Mathematical modeling of energy consumption in the acute inflammatory response during sepsis

by

Ivan Ramirez Zuniga

B.S., Mathematics, Universidad de Costa Rica, 2010

M.S., Mathematics, East Tennessee State University, 2014

Submitted to the Graduate Faculty of

the Dietrich School of Arts and Sciences in partial fulfillment

of the requirements for the degree of

Doctor of Philosophy

University of Pittsburgh

2020

UNIVERSITY OF PITTSBURGH

DIETRICH SCHOOL OF ARTS AND SCIENCES

This dissertation was presented

by

Ivan Ramirez Zuniga

It was defended on

July 9th 2020

and approved by

Dr. Jonathan E. Rubin, Professor, Department of Mathematics

Dr. David Swigon, Associate Professor, Department of Mathematics

Dr. Gilles Clermont, MD, Department of Critical Care Medicine UPMC

Dr. G. Bard Ermentrout, Distinguish University Professor, Department of Mathematics

Mathematical modeling of energy consumption in the acute inflammatory response during sepsis

Ivan Ramirez Zuniga, PhD

University of Pittsburgh, 2020

When a pathogen invades the body, an acute inflammatory response is activated to eliminate the intruder. In some patients, runaway activation of the immune system may lead to collateral tissue damage and, in the extreme, organ failure and death. Experimental studies have found an association between severe infections and depletion in levels of adenosine triphosphate (ATP), increase in nitric oxide production, and accumulation of lactate, suggesting that tissue energetics is compromised.

We present a computational model consisting of ordinary differential equations to explore the dynamics of the acute inflammatory response against infections caused when a pathogen makes its way into a host. This model incorporates energy production along with the energy requirements that arise when fighting such an infection. In particular, we investigate the role of energetics during infection and explore the relation between overproduction of nitric oxide (NO), lactate, altered adenosine triphosphate (ATP) levels, and sepsis.

Finally, a data-driven approach is used to extend our model as an effort to better understand the role of energy in sepsis. This extended model is calibrated by fitting animal data from a study done in thirty-two baboons that were induced into sepsis after infusing E. coli intravenously. Using Bayesian analysis, we quantify uncertainty in model parameters and with them we investigate differences across different populations, including survivors and non-survivors.

Table of contents

Preface . . . xii

1.0 Introduction . . . 1

2.0 Mathematical modeling of energy consumption in the acute inflammatory response . . . 5

2.1 Introduction . . . 5

2.2 Mathematical model . . . 6

2.3 Fundamental asymptotic states and multi-stability . . . 15

2.4 Model application to altered metabolic states . . . 21

2.4.1 Hypoglycemia . . . 22

2.4.2 Hyperglycemia . . . 24

2.4.3 Hypoxia . . . 25

2.4.4 Survival analysis . . . 27

2.5 Discussion . . . 36

3.0 A data-driven model of the role of energy in sepsis . . . 38

3.1 Introduction . . . 38

3.2 Experimental data . . . 38

3.3 Mathematical model . . . 45

3.4 Results . . . 51

3.5 Discussion . . . 52

4.0 Parameter estimation on data-driven model . . . 59

4.1 Introduction . . . 59

4.2 Ordinary least squares (OLS) . . . 59

4.3 Bayesian inference for parameter estimation . . . 69

4.3.1 Random walk Metropolis algorithm with non-informative prior . . . 71

4.3.2 Delayed rejection adaptive Metropolis algorithm (DRAM) . . . 72

4.3.3 Space distribution of virtual subjects . . . 74

4.3.4 Validation of the total distribution . . . 85
4.4 Discussion . . . 93
5.0 Applications of data-driven model . . . 96
5.1 Introduction . . . 96
5.2 Inducing hypoglycemia and hyperglycemia . . . 97
5.3 Introducing therapy . . . 102
5.3.1 Modeling therapy . . . 102
5.3.2 Metropolis algorithm with informative prior on treated subjects . . . 103
5.3.3 Alternative scenarios of treatment induction . . . 110
5.4 Logistic regression: identifying outcome from patient characteristics . . . 112
5.4.1 Preliminaries . . . 112
5.4.2 Logistic regression on survivors and non-survivors non-treated . . . 115
5.4.2.1 Envelopes for non-survivors and survivors . . . 120
5.4.3 Logistic regression on non-survivors non-treated: septic and aseptic . . . 124
5.4.3.1 Envelopes for septic and aseptic . . . 127
5.4.4 Logistic regression on non-survivors with therapy . . . 130
5.4.4.1 Envelopes for non-survivors treated: survivors and non-survivors 138
5.4.4.2 Envelopes for non-survivors treated: septic and aseptic . . . 138
5.5 The role of anti-inflammatory mediators and glucose . . . 141
5.6 Discussion . . . 145
6.0 Conclusions . . . 149
Appendix. Individual fits with DRAM . . . 153
Bibliography . . . 156

List of tables

1 Parameter values 13
2 Parameter values continued 14
3 Biologically significant equilibrium points 18
4 Healthy equilibrium state values for equations (12)-(25) 50
5 Parameter values for the health sample trajectory 57
6 Parameter values for the health sample trajectory continued 58
7 Best fit parameter values and initial conditions for average of the survivors . . . 64
8 Metropolis with informative prior: individual fits for non-treated subjects . . . 85
9 Metropolis with informative prior: individual fits on non-survivors non-treated with 5 and 6 data points 88
10 Metropolis with informative prior: individual fits on survivors non-treated with 5 and 6 data points 89
11 Inducing metabolic conditions in total population X_{tot} 98
12 Metropolis with informative prior: individual fits of treated subjects 103
13 Metropolis with informative prior: individual fits of treated subjects with 5 and 6 time points 105
14 Alternative therapy protocols 110
15 Logistic regression summary for non-treated subjects when classifying subjects between survivors and non-survivors 116
16 Standard deviation of significant parameters when classifying non-treated subjects between survivors and non-survivors 117
17 Standard deviation of parameters in septic versus aseptic within non-treated non-survivors 126
18 Logistic regression summary for non-survivors after treatment that are classified between septic and aseptic. 127

19 Logistic regression summary for non-survivors after treatment that are classified between survivors and non-survivors 133
20 Standard deviation for parameters in non-survivors treated 134
21 Exploring role of glucose and anti-inflammatory mediators 142

List of figures

1 Wiring diagram for reduced model 7
2 Cell respiration process 10
3 Sample trajectories 17
4 Bifurcation diagrams 20
5 Basin of attraction baseline 22
6 Basin of attraction for hypoglycemic versus baseline 24
7 Basin of attraction for hyperglycemic versus baseline 26
8 Basin of attraction for hypoxia versus baseline. 28
9 Representation of outcomes for a population of 300 virtual patients on the k_{pg} versus P_0 plane 32
10 Representation of outcomes for a population of 300 virtual patients on the k_{pg} versus max D plane. 33
11 Survival curves 34
12 Survival curves for metabolic conditions 35
13 Data survivors non-treated 41
14 Data non-survivors non-treated 42
15 Data survivors treated 43
16 Data non-survivors treated 44
17 Wiring diagram for the extended model 48
18 Sample model trajectories for the healthy state 54
19 Sample model trajectories for the aseptic state 55
20 Sample model trajectories for the septic state 56
21 Best fit for the observable trajectories in average of the survivors with logarithmic time scale 65
22 Best fit for the observable trajectories in average of the survivors in linear scale 66

23 Model trajectories obtained with best fit for average of the survivors with logarithmic time scale . . . 67
24 Model trajectories obtained with best fit for average of the survivors in linear scale 68
25 Parameter chain paths obtained with DRAM when fitting S89 . . . 78
26 Marginal parameter densities obtained with DRAM when fitting S89 . . . 79
27 Envelopes of observed trajectories for S89, S90, S100, and S101 . . . 80
28 Envelopes of observed trajectories for NS73, NS74, NS88, and NS98 . . . 81
29 Envelopes of model trajectories for S89 . . . 82
30 Envelopes of model trajectories for NS73 . . . 83
31 Marginal parameter densities of total distribution . . . 84
32 Test results for NS67, NS74, NS88, NS98 . . . 87
33 Test results for NS88 with 5, 6, and 9 time points . . . 89
34 Test results for S89 with 5 and 6, and 11 time points . . . 90
35 Envelopes for S89 with 5, 6, and 11 time points . . . 91
36 Envelopes for NS88 with 5, 6, and 9 time points . . . 92
37 Envelopes for hypoglycemia versus baseline . . . 100
38 Envelopes for hyperglycemia versus baseline . . . 101
39 Envelopes of model trajectories corresponding to posterior density for NS68, NS71, NS78, and NS94 . . . 106
40 Envelopes of model trajectories corresponding to posterior density for S91, S102, S103, and S10 . . . 107
41 Envelopes of model trajectories for individual fit of NS68 . . . 108
42 Envelopes of model trajectories for individual fit of S102 . . . 109
43 Diagram of three different scenarios studied with logistic regression . . . 114
44 Confusion matrix and ROC curve when classifying non-treated subjects between non-survivors and survivors. . . . 118
45 Quartiles of most contributing parameters when non-treated subjects are classified between non-survivors and survivors. . . . 120
46 Densities of most contributing parameters when non-treated subjects are classified between non-survivors and survivors . . . 121

47 Pair correlations of some parameters in the survivors and non-survivors cohorts 122
48 Envelopes of non-treated non-survivors and survivors 123
49 Confusion matrix and ROC curve for septic and aseptic. 125
50 Pair correlations of some parameters in septic versus aseptic 126
51 Quartiles of most contributing parameters for non-survivors non-treated when classified between septic and aseptic. 127
52 Densities of most contributing parameters for non-survivors non-treated when classified between septic and aseptic. 128
53 Envelopes of non-survivors that are septic or aseptic 129
54 Pair correlations of some parameters for non-survivors treated that survive or do not survive. 132
55 Densities of most contributing parameters for non-survivors after treatment. . 135
56 Parameter quartiles of most contributing parameters for non-survivors after treatment. 136
57 Confusion matrix and ROC curve for non-survivors after treatment. 137
58 Envelopes of non-survivors who were treated that survive or die 139
59 Envelopes for non-survivors treated that died of sepsis or asepsis 140
60 Envelopes comparing increasing source of C_A and baseline 142
61 Envelopes comparing increasing glucose source s_g and baseline 143
62 Envelopes comparing lowering glucose source s_g and baseline 144
63 Envelopes of observed trajectories for NS66, NS67, NS69, and NS76 154
64 Envelopes of observed trajectories for NS80, NS92, NS97, and NS104 155

Preface

This thesis is dedicated to my wife, Pamela Delgado. Pame you have been my partner during this entire journey, we have cried from happiness and frustration, but we have always been together. I am sure I would have not done this without your love, patience and support.

There are many people who I would like to express my gratitude. My advisors Jon Rubin and David Swigon, I thank you for your continuous support and dedication. You both are extraordinary scientists and I am grateful for having you as my mentors. Dr. Swigon, thank you for taking the time to help me prepare for my preliminary exams and comps. Thank you for your patience and support during many unofficial meetings when I needed additional help with understanding concepts or debugging code. Dr. Rubin, thank you for always making me go the extra mile and improve myself. Thank you for your constant help, patience, and guidance during all these years. Thank you for always finding time to meet unofficially and always being there whenever I needed advise. Dr. Clermont, you were basically my third advisor. Thank you for your support, encouragement, patience, and advise. I consider myself lucky to have had you guys as my mentors. And I hope I can one day be as inspiring and successful as you all are. Dr. Ermentrout, thank you for feedback and discussions after my Mathbio seminars and in the manuscript. You were definitely a great complement to my committee. Dr. Lennard, thank you so much for your help and support, specially during complicated times. Thank you and Cathy for your kindness, your friendship, and love. You guys are like family to Pam and me.

I am grateful for the support I received during my first and last years as graduate student at Pitt through the Arts and Sciences Graduate Fellowship in 2014-2015, and the Andrew Mellon Predoctoral Fellowship in 2019-2020. These fellowships helped me focus on my personal academic and professional goals.

I would like to thank in general all the Math department, but specially Dr. Pan for his help, Dr. Vainchtein, Dr. Trenchea, Dr. Yotov, Dr. Nielan, Dr. DeBlois, and Dr. Jiang. Also, I would like to thank the entire Mathbio group for so many interesting talks and discussions on Thursdays. I would also like to thank the department staff for their job

in trying to make things easier for us graduate students.

I would like to thank my family and friends who were always there to support me, not only during my time at Pitt but throughout my entire academic journey. Last but not least, I would like to thank God, for so many blessings and letting me live my dreams and fight for them.

1.0 Introduction

When pathogens enter the body, a complex chain of reactions occurs in which the immune system activates and attempts to eliminate the intruders and prevent persistent infection. For a short period of time, invading pathogens can reproduce rapidly. However, encounters with pathogens activate immune cells, such as macrophages and neutrophils, which release signaling molecules such as cytokines and eliminate pathogens through means such as phagocytosis and recruitment of additional immune cells. Under normal circumstances, as long as the initial insult is sufficiently limited, the immune response will satisfactorily eliminate the pathogen and the host will become healthy again. In some cases, however, the initial response may escalate into an overwhelming systemic inflammation. Such overreaction of the immune system can lead to tissue damage, organ failure, and possibly death. This state of uncontrolled inflammation is known as sepsis. Every year severe sepsis affects more than 1.7 million people in the U.S. alone and over 30 million people worldwide [1].

Several studies have found associations between overproduction of nitric oxide (NO), mitochondrial dysfunction, and sepsis [12], [13], [14]; moreover, it has been proposed that septic organ failure is caused by depression of mitochondrial function, [18]. Because mitochondria are organelles responsible for the generation of most of the energy in a cell, mitochondrial dysfunction directly affects the production of ATP, which could contribute to this association. For instance, in a study performed on skeletal muscle of 28 patients with sepsis, [12] observed a relation between overproduction of NO, mitochondrial dysfunction and lowered adenosine triphosphate (ATP) levels. They reported a decrease in mitochondrial complex I activity, the magnitude of which was associated with the degree of NO production in skeletal muscles of patients admitted to intensive care with septic shock. In a subsequent study, similar results were found in muscle and liver in a long-term rodent model of fecal peritonitis [13]. Furthermore, [14] found that adding NO to isolated rat brain mitochondria inhibits ATP synthesis. Since ATP provides energy for physiological processes including activation of immune cells, production and release of signaling molecules, protein synthesis, and tissue repair [17], [16], lowered ATP levels are likely to compromise aspects of the inflammatory

response; yet, since this response involves a complex balance of pro- and anti-inflammatory effects, the impact of these ATP-related alterations is not straightforward to predict.

Computational modeling provides an approach to deriving predictions about complex biological systems that can effectively complement experimental work and allow the exploration of manipulations that may not be experimentally feasible. In particular, a variety of previous works have drawn insights from reduced computational models of the inflammatory response. Often such models lump cytokine actions into a small number of classes exhibiting coarsely similar properties or simply combine together all pro-inflammatory components of the response, but they nonetheless can provide useful information. For instance, [47] proposed a simplified model for acute inflammation that includes pathogens, early pro-inflammatory effectors such as macrophages and neutrophils, and late pro-inflammatory feedback; despite its simplicity, the model yielded predictions about how changes in biologically interpretable parameters influenced inflammatory outcomes and was used to suggest therapeutic strategies. Soon afterwards, another reduced model was developed to describe the dynamics of the acute inflammatory response including pathogens, tissue damage and activated neutrophils along with an anti-inflammatory mediator, which was used to study how the dynamics of anti-inflammatory feedback contribute to patient outcomes, [61]. A related model was also used to suggest possible explanations for tolerance effects arising with repeated endotoxin exposure, [26]. A somewhat more detailed model for the acute inflammatory response was shown to fit data from mice exposed to various inflammation-inducing insults and was used to predict mortality outcomes following endotoxin injection [19], while another work used parameter optimization based on fits to data to demonstrate both that different balances of inflammatory processes could yield similar cytokine dynamics yet with different mortality expectancies, [24]. Such models have also been used to study control strategies for inflammation, [25], as well as to explore the impact of blood filtration on inflammation, [57].

Unlike these earlier models, [23] derived several compartmental models describing the interaction between energy resources, a general pool of immune cells, and pathogens. These models were employed to study the scenario when the immune agents and pathogens have separate resources and the case when both depend on the same source. However, these models

do not incorporate signaling components of the immune response, such as pro- and anti-inflammatory cytokines, and their level of abstraction poses an obstacle for model comparison with human and animal data.

In contrast to these works, other modeling frameworks offer alternatives that take into account spatiotemporal dynamics. For example, partial differential equations have been used to study the immune response to antigen including spatial effects such as immune cell recruitment and granuloma formation, [73]. Similarly, agent-based models that treat pathogens as well as immune-related molecules and cells as discrete agents that move around in a spatial domain have been used in a variety of works (e.g., [27] and the references therein). In these models, biological mechanisms can be encoded in rules used to perform discrete temporal updates of system states. We instead work with continuous ordinary differential equation models because we wish to apply dynamical systems methods such as bifurcation analysis and because our study is motivated by data sets that lack spatial information.

This thesis can be subdivided in two large stages: a forward problem and an inverse or backward problem. The forward problem is presented in Chapter 2, which is the foundation of our work, as we present an initial mathematical model that encloses the dynamics of the acute inflammatory response including the energy requirements to fight an infection. Numerical analysis of the model help to understand important model features. We use this model as a tool to study the effect of metabolic conditions such as hypoglycemia, hyperglycemia, and hypoxia.

We continue in Chapter 3, where we extend our initial model presented in Chapter 2 to include new state variables that were observed in an experimental study performed in baboons who were induced into sepsis by bacterial infusion. Chapter 4 builds in the model developed in Chapter 3 and it consists of solving the backward problem of parameter estimation given the observed data. We follow a Bayesian approach to construct a distribution of virtual patients and determine model parameter densities to quantify uncertainty in model parameters. Next, in Chapter 5 we use our model to revisit the effect of hypoglycemia and hyperglycemia in a virtual population. We also adapt our model to study the role of an NOS inhibitor, a drug treatment used in the same baboon study. Further, we use logistic regression to identify key parameters that can be used to predict patient outcome. Lastly,

Chapter 6 concludes with final remarks and conclusions.

Some of the main goals that will be addressed in the second stage of this thesis are to understand what biological factors determine whether a patient will end up being a survivor or a not survivor. And within the non-survivors, the same question between septic and aseptic patients. Similarly, we are interested in finding what biological factors determine whether a patient will survive or not after treatment. We also want to predict from patient data whether a patient will be a survivor or non-survivor. And to understand effects of energy-related conditions on patient outcomes.

By the time of thesis submission only the work presented in Chapter 2 has been published, [59].

2.0 Mathematical modeling of energy consumption in the acute inflammatory response

2.1 Introduction

This chapter is based on our published work [59]. Here, we develop a computational model to study the dynamics of acute inflammation that incorporates a reduced representation of relevant metabolic pathways and energy resources and demands. We use our model to investigate the role of energetics during infection and to explore the relation between overproduction of NO, altered ATP levels, and sepsis. Moreover, disorders in energy metabolism or other alterations in metabolic states, such as hypoglycemia, hyperglycemia and hypoxia, can trigger organ dysfunction as is characteristic in patients with sepsis [28]. These conditions can be associated with low levels of ATP and with lactate accumulation, and thus we apply our model to predict their impact on the acute inflammatory response as well.

This chapter is organized as follows. In Section 2.2, we provide a complete and detailed description of the mathematical model that we have developed. In Section 2.3, we present an analysis of the model starting with numerical simulations, bifurcation analysis and computation of basins of attraction of stable states across varying levels of pathogen growth rate. These results are followed in Section 2.4 by the application of the model to study the altered metabolic conditions of hypoglycemia, hyperglycemia, and hypoxia in comparison with baseline states. Finally, in Section 2.4.4 we perform a survival analysis for 300 virtual patients and compare their outcomes under each of the conditions mentioned above. In Section 2.5, we conclude with a discussion.

2.2 Mathematical model

Here we present a reduced model of immune response to pathogen infection that includes several pro-inflammatory and anti-inflammatory drivers and that accounts for the energy consumption associated with the immune response and the effect of energy imbalance on the system. This model builds on the work of [61] and consists of eight nonlinear ordinary differential equations that describe the interactions between the immune response to a pathogen and the associated energy production and demand. As in the Reynolds model, the state variable P denotes the number of pathogens present, N is the level of active phagocytes and also represents their pro-inflammatory effects, D is a marker of tissue damage, and C_A denotes the level of anti-inflammatory mediators. In addition, we introduce new state variables A_n, A_b, X, and L as follows: A_n measures the levels of ATP produced by phagocytes such as neutrophils and macrophages, A_b corresponds to the levels of ATP generated by all other cells in the body, and X and L are the levels of NO and lactate in the host, respectively. With this choice of new variables we seek to study the role of ATP in acute inflammation including the contributions of NO and the implications for lactate production. The inclusion of lactate is motivated by the fact that it is commonly measured as a risk factor for sepsis in the ICU; similarly, levels of ATP and of by-products of NO such as nitrate are available in animal data. Several terms in the model feature an ATP-dependent factor that scales the vigor of the process based on the availability of the relevant energy supply, while a collection of energy flux terms in the ATP equations effect energy consumption.

Our model is based on the interactions shown in Fig. 1. When pathogens enter the body, a complex chain of reactions occurs, starting with tissue damage and activation of phagocytes N. These activated effectors induce inflammation followed by a surge of anti-inflammatory cytokines that balance the recruitment of more phagocytes and down-regulate the production of harmful substances such as NO (X). Unlike previous work [61], we do not include a direct reciprocal interaction between N and D; that is, in our model N does not directly promote D. Instead, both N and D produce X, which in turn promotes D. These interactions clearly represent a positive feedback loop: NO causes tissue damage while tissue damage induces more inflammation that enhances NO release. Since every metabolic

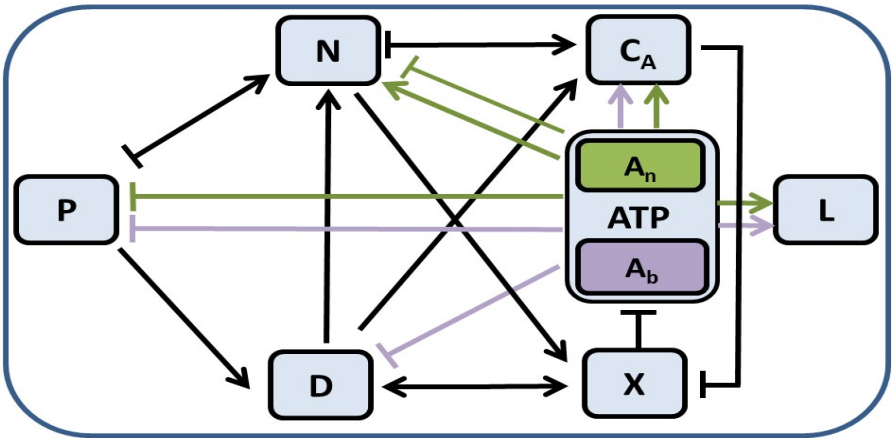

Figure 1: Interactions between the eight variables appearing in the system of equations (1)-(8). The system includes pathogens (P), a marker of tissue damage (D), active phagocytes (N), anti-inflammatory mediators (C_A), nitric oxide (X), and lactate (L), while A_n and A_b correspond to the levels of ATP produced by phagocytes and all other cells in the body, respectively. Arrows and bars indicate up and down regulation, respectively. The effects on model components influenced by levels of A_n are indicated by green arrows and bars while the effects dependent on A_b are denoted in purple.

process requires energy in the form of ATP, the intensities of phagocyte activation, pathogen elimination, healing of tissue and production of anti-inflammatory mediators in the model are all modulated by ATP levels. Finally, as a byproduct of anaerobic ATP production, lactate L is produced.

The ATP energy source for the inflammatory response is produced in the cytosol and mitochondria through the sequential processes of glycolysis and oxidative phosphorylation, the latter of which requires oxygen (Fig. 2). Although in anaerobic respiration fewer molecules of ATP are produced, this process is about 100-times faster than oxidative phosphorylation and therefore is preferred for some immune cells as a quick source of energy, even if oxygen

is abundant. Moreover, sites of inflammation are often hypoxic environments and although some oxydative phosphorylation takes place, neutrophils and macrophages depend mostly on glycolysis for energy production, [9, 58]. Thus, we will introduce separate equations for a phagocyte ATP level, A_n, and an ATP level available to other cells in the body, A_b. Indeed, ATP is produced locally and has a very short half-life, justifying the use of two physically separated pools of ATP. Within each pool, both glycolysis and oxidative phosphorylation contribute to ATP production, although to different extents. Oxidative phosphorylation in both pools is compromised by X due to the known competitive inhibitory effect of NO on this pathway.

The following system of differential equations incorporates these many biological considerations. Values and meanings for all parameters are given in Table 2; note that the saturating function g modulates energy-intensive terms based on availability of relevant ATP supplies, while the Hill function f represents inhibitory effects:

$$\frac{dP}{dt} = k_{pg}P\left(1-\frac{P}{P_\infty}\right) - (1+k_{ns}g(A_b))\frac{k_{pm}P}{\mu_m + k_{mp}P} - \frac{k_{pn}g(A_n)f\left(\frac{C_A}{C^*}\right)NP}{1+k_{ps}P} \tag{1}$$

$$\frac{dN}{dt} = \frac{s_{nr}g(A_n)f\left(\frac{C_A}{C^*}\right)(k_{nn}N + k_{np}P + k_{nd}D)}{\mu_{nr} + f\left(\frac{C_A}{C^*}\right)(k_{nn}N + k_{np}P + k_{nd}D)} - \mu_n\left(1 + \frac{k_{de}g(A_n)f\left(\frac{C_A}{C^*}\right)P}{1+k_{ps}P}\right)N \tag{2}$$

$$\frac{dD}{dt} = k_{dn}h(X+P) - g(A_b)\mu_d D \tag{3}$$

$$\frac{dC_A}{dt} = s_c + k_{cn}\left(\frac{g(A_n)f\left(\frac{C_A}{C^*}\right)N}{\mu_{cq} + f\left(\frac{C_A}{C^*}\right)N} + \frac{g(A_b)f\left(\frac{C_A}{C^*}\right)k_{cnd}D}{\mu_{cq} + f\left(\frac{C_A}{C^*}\right)k_{cnd}D}\right) - \mu_c C_A \tag{4}$$

$$\frac{dA_b}{dt} = c(A_b)\left(f\left(\frac{X}{X^*}\right)(1-\lambda_{gb}) + \lambda_{gb}\right) - g(A_b)\sum_{i\in\{1,4,6\}}\Phi_i - \mu_A A_b \tag{5}$$

$$\frac{dA_n}{dt} = c(A_n)\left(f\left(\frac{X}{X^*}\right)(1-\lambda_{gn}) + \lambda_{gn}\right) - g(A_n)\sum_{i\in\{2,3,5\}}\Phi_i - \mu_A A_n \tag{6}$$

$$\frac{dX}{dt} = f\left(\frac{C_A}{C^*}\right)(k_{non}N + k_{nod}D) - \mu_{no}X \tag{7}$$

$$\frac{dL}{dt} = \lambda_L\left(1 - f\left(\frac{X}{X^*}\right)\right)\left((1-\lambda_{gb})\,c(A_b) + (1-\lambda_{gn})\,c(A_n)\right) - \mu_L L \tag{8}$$

where

$$f(V) = \frac{1}{1+V^2}\ ; \quad h(V) = \frac{V^6}{x_{dn}^6 + V^6}\ ; \quad c(A_x) = \frac{\mu_A(1+k_2)}{k_2 + e^{k_1(A_x-1)}}\ ; \quad g(A_x) = \frac{A_x^2}{c_g + A_x^2}\ ;$$

$$\Phi_1 = c_1 \frac{k_{pm} s_m k_{ns} P}{\mu_m + k_{mp} P} \; ; \quad \Phi_2 = c_2 \frac{k_{pn} f\left(\frac{C_A}{C^*}\right) NP}{1 + k_{ps} P} \; ; \quad \Phi_3 = c_3 \frac{s_{nr} f\left(\frac{C_A}{C^*}\right) (k_{nn} N + k_{np} P + k_{nd} D)}{\mu_{nr} + f\left(\frac{C_A}{C^*}\right) (k_{nn} N + k_{np} P + k_{nd} D)};$$

$$\Phi_4 = c_4 \mu_d D; \quad \Phi_5 = c_5 \frac{k_{cn} f\left(\frac{C_A}{C^*}\right) N}{\mu_{cq} + f\left(\frac{C_A}{C^*}\right) N} \; ; \quad \Phi_6 = c_6 \frac{k_{cn} f\left(\frac{C_A}{C^*}\right) k_{cnd} D}{\mu_{cq} + f\left(\frac{C_A}{C^*}\right) k_{cnd} D}$$

The first four equations in system (1)-(8) are based on the model given in [61], where the reader can find a more detailed explanation of the derivation of these equations as well as a detailed description of the parameters used there. For consistency, we kept the same variable and parameter nomenclature. In equation (1), the dynamics of P is driven by a logistic growth term where k_{pg} and P_∞ are the growth rate and carrying capacity of P, respectively. The second term of this equation describes the elimination of P by nonspecific immune responses, such as defensins and nonspecific antibodies [61]. We assume that this process includes two mechanisms: one that is local with negligible energy requirements and a second where the phagocytes spend energy either traveling to the infected area or activating. The third and last term of the P equation describes the removal of pathogens by activated neutrophils N through phagocytosis, the efficacy of which depends on A_n and is down-regulated by the anti-inflammatory mediators C_A.

In a positive feedback cycle, pro-inflammatory cytokines activate phagocytes, while activated phagocytes in turn release these cytokines. As in [61], since our model includes a single combined pro-inflammatory variable N, we collapse this cycle into a positive feedback of N on itself, which appears in the first term of equation (2). This term also includes the recruitment of pro-inflammatory effects by tissue damage and by processes triggered by the presence of pathogen, all modulated by A_n and C_A. Equation (2) also includes a depletion term that encompasses an intrinsic decay rate μ_n as well as an energy-dependent collateral damage effect from phagocytosis.

The production of tissue damage D is controlled in equation (3) by the Hill function $h(X + P)$, based on the assumption that both NO and pathogens promote D; indeed, NO is also associated with microvascular damage, organ dysfunction and induction of programmed cell death, or apoptosis. This term includes the same exponent used previously [61], which

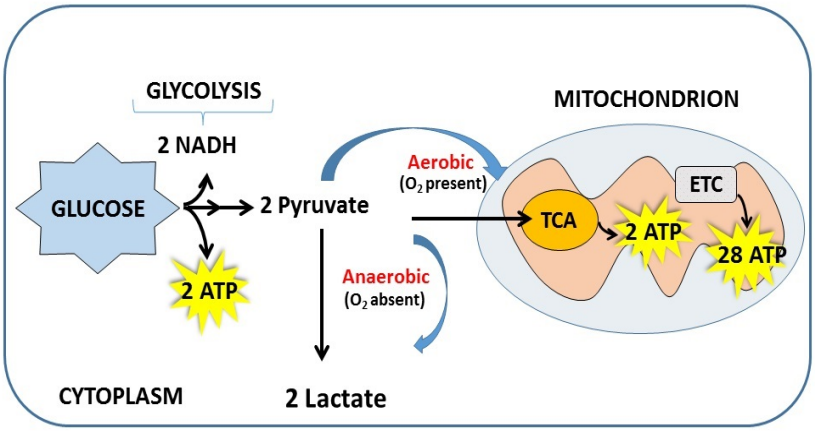

Figure 2: Schematic diagram of cellular respiration. One molecule of glucose is metabolized into two molecules of pyruvate. In the presence of oxygen, pyruvate enters mitochondria to be oxidized into acetyl-CoA by a process called pyruvate decarboxylation. Acetyl-CoA is then metabolized in the tricarboxylic acid cycle (TCA) or Krebs cycle. Here, acetyl-CoA undergoes a cycle of reactions where some ATP, as well as ETC substrates (such as NADH) are produced. These substrates, by virtue of electron exchange in the ETC, generate an electrochemical gradient at the internal mitochondrial inner membrane that is associated to the production of more ATP as protons move along this gradient. About 30 molecules of ATP are produced in this process. In contrast, in the absence of oxygen (anaerobic respiration or glycolysis respiration), the molecules of pyruvate are synthesized into two molecules of lactate in a process called fermentation. In this metabolic pathway only two molecules of ATP are produced. Anaerobic respiration, also called anaerobic glycolysis, is about 100-times faster than oxidative phosphorylation and therefore is preferred for some immune cells as a quick source of energy, even if oxygen is abundant.

provides a reasonable gradation of D levels across healthy, aseptic, and septic outcomes. Damage production increases in a saturating way with half-activation x_{dn}. We assume that healing occurs at a rate of μ_d and also requires energy. For simplicity we neglect any contributions of phagocytes to clearing damaged tissue and assume that only A_b fuels healing.

Equation (4) describes the dynamics of the anti-inflammatory mediators C_A as in [61], with terms for a baseline anti-inflammatory level s_c, the promotion of anti-inflammatory release by N and D, and an intrinsic decay term. We make the modification, however, that C_A release related to activated phagocytes and tissue damage depend on A_n and A_b, respectively.

We define a rate function for production of A_x, where x stands for each of the subindices b and n, as a decreasing sigmoidal function $c(A_x)$. This phenomenological term represents a ramping up of energy production when supplies diminish, [6]. It multiplies a sum of an aerobic respiration (pyruvic pathway) component $f\,(X/X^*)\,(1-\lambda_{gx})$, downregulated by NO, [15, 55], and an anaerobic respiration (glycolysis) term λ_{gx}. Because about 30 molecules of ATP are produced per molecule of glucose in the aerobic pathway, while only 2 molecules of ATP are produced in glycolysis, we estimated λ_{gb} in such a way that $(1-\lambda_{gb})/\lambda_{gb} = 15$. On the other hand, unlike the majority of cells in the body, phagocytes rely on ATP production from mostly the anaerobic pathway. For this reason, we estimated $\lambda_{gn} = 0.9$.

The A_x equations include sums of energy flux terms Φ_i that represent all of the processes in the model that consume energy and hence deplete the level of A_x. Specifically, phagocyte production/activation and migration of phagocytes to the infected area are all processes that require A_n and are represented in Φ_3. Note that even though energy dependence arises in the final terms of both equations (1) and (2), these terms derive from the effects of the same process, phagocytosis. For this reason, the single flux term Φ_2 accounts for both of these terms. A_n is also consumed in the production of anti-inflammatory mediators by phagocytes in equation (4), represented by Φ_5. Similarly, A_b is consumed by non-specific pathogen elimination and production of anti-inflammatory mediators as well as in healing and cellular regeneration. Corresponding terms appear in equations (1), (3), and (4) and these effects are captured in the flux terms Φ_1, Φ_4, Φ_6. We assume that both ATP supplies are naturally depleted at a constant rate of μ_A and in the absence of infection both reach an equilibrium level at 1.

The production of NO, denoted by X, is driven by tissue damage and by activated phagocytes via induction of iNOS through pro-inflammatory cytokines, such as IL-1β, IL-2, IL-6, TNF and IF$-\gamma$, [46]. The former process is included in the $k_{nod}D$ term while the latter

process motivates the $k_{non}N$ term in the production of NO in equation (7). This production is modulated by anti-inflammatory mediators, such as IL-10 and IL-8, represented in equation (7) with the factor $f(C_A/C^*)$. Nitric oxide is assumed to be naturally depleted at a rate of μ_{no} .

Lactate, denoted by L, is generated in anaerobic glycolysis. In the absence of oxygen, glucose is metabolized into pyruvate generating lactate as a byproduct. Equation (8) was constructed such that the greater the inhibition of cellular respiration through NO, the more lactate is produced. Finally, lactate is assumed to be naturally depleted at a rate of μ_L. Lactate will play an important role in our model as there is available data of lactate for septic patients.

Some of the parameters in our model were extracted from existing literature as shown in Table 2. However, the remaining parameters were tuned to achieve biologically reasonable behavior. For instance, all the state variables must remain positive. Also, some processes are known to require more energy than others, and the parameters involved in the energy fluxes were estimated accordingly. Moreover, nitric oxide is known to have rapid dynamics [76] and ATP production depends on two different pathways with different production rates. All of these considerations were taken into account when tuning the model parameters. Most of these parameters are dimensionless since the variables represented by the model are assumed dimensionless as we are concerned here with qualitative behavior of the system rather than fitting specific data sets. The system of equations (1)-(8) was solved numerically using ode23s in Matlab R2018a. We choose this solver to avoid issues with stiffness and accuracy; results with ode45 were similar (data not shown).

Table 1: Parameter values

Parameter	Range	Value	Description	Sources
k_{pg}	0.021-2.44/h	Varies	Pathogen growth rate	[69], [77]
P_∞	Estimated	20×10^6/cc	Carrying capacity for pathogen	Vodovotz, Y. pers. comm.
k_{pm}	Estimated	0.002	Rate parameter for the elimination of pathogens by the non-specific local response	
k_{ns}	Estimated	0.25	Weighting of the energy-dependent component of non-specific pathogen elimination	
μ_m	0.0013–0.0048/h	0.002/h	Half-activation parameter for the non-specific local response	[44]
k_{mp}	Estimated	0.1	Saturation rate parameter for the non-specific local response	
k_{pn}	Maximum 2.5/N-units/h	0.75	Phagocytosis rate	[10]
C^*	Estimated	0.17	Saturation parameter for effects of anti-inflammatory mediators	[42]
k_{ps}	Estimated	0.3	Phagocytosis saturation constant	
s_{nr}	Estimated	0.16	Production rate for activated phagocytes (based on resting phagocyte level [61])	
k_{nn}	Estimated	0.007	Weighting of contribution to activation of resting phagocytes by previously activated phagocytes and their cytokines	
k_{np}	Estimated	0.5	Weight of contribution to activation of resting phagocytes by pathogen	
k_{nd}	Less than k_{np}	0.03/h	Weight of contribution to activation of resting phagocytes by tissue damage	[2]
μ_{nr}	0.069-0.12/h	0.1/h	Decay rate of resting phagocytes [61]	[22]
μ_n	Less or equal than μ_{nr}	0.1/h	Decay rate of activated phagocytes	[22]
k_{de}	Estimated	0.75	Pathogen degradation enhancement constant	
k_{dn}	Estimated	0.0037	Maximum rate of damage produced by activated phagocytes	
x_{dn}	Estimated	0.14	Determines levels of pathogens and nitric oxide needed to bring damage production up to half its maximum	
μ_d	Estimated	0.01/h	Decay rate of damage	
s_c	Estimated	0.0625	Source of anti-inflammatory mediators	[80]

Table 2: Parameter values continued

Parameter	Range	Value	Description	Sources
k_{cn}	Estimated	0.02	Maximum production rate of anti-inflammatory mediators	
k_{cnd}	Estimated	48	Effectiveness of damaged tissue relative to activated phagocytes in inducing production of anti-inflammatory mediators	
μ_{cq}	Estimated	1	Determines the levels of activated phagocytes and damage that are needed to bring rate of anti-inflammatory mediator production to half its maximum	
μ_c	0.15-2.19/h	1/h	Decay rate of anti-inflammatory mediators	[3], [8] [34], [41]
μ_A	Estimated	0.1	Baseline depletion rate of both ATP supplies	
c_g	Estimated	1	Half-saturation energy level for the driving of various processes	
k_1	Estimated	3	Phenomenological energy production parameter	
k_2	Estimated	0.01	Phenomenological energy production parameter	
c_1	Estimated	0.03	Energy consumption rate of Φ_1	
c_2	Estimated	0.015	Energy consumption rate of Φ_2	
c_3	Estimated	2.25	Energy consumption rate of Φ_3	
c_4	Estimated	4	Energy consumption rate of Φ_4	
c_5	Estimated	0.05	Energy consumption rate of Φ_5	
c_6	Estimated	0.05	Energy consumption rate of Φ_6	
k_{non}	Estimated	3	Rate of NO release due to presence of pro-inflammatory cytokines	
k_{nod}	Estimated	0.1	Rate of NO release due to tissue damage	
μ_{no}	Estimated	1	Natural depletion rate of NO	
X^*	Estimated	0.5	Half saturation level of NO	
λ_L	Estimated	0.5	Production rate of lactate	
μ_L	Estimated	0.05	Decay rate of lactate	
λ_{gb}	Estimated	0.0625	Fraction of A_b produced via the anaerobic pathway in the absence of NO	
λ_{gn}	Estimated	0.9	Fraction of A_n produced via the anaerobic pathway in the absence of NO	

2.3 Fundamental asymptotic states and multi-stability

The system of equations (1)-(8) exhibits three biologically significant long term outcomes. The outcome that allows host survival, the healthy state, occurs when the immune system is able to completely eliminate the pathogen and there is resolution of inflammation. When the immune system satisfactorily eliminates the insult but in the process, a sustained immune activation occurs, leading to persistent inflammation and tissue damage, the patient is said to be in aseptic state. In this case, multiple organ dysfunction syndrome (MODS) may occur, followed eventually by death. The third and possible outcome, the septic state, occurs when a massive influx of pathogens attacks the host or when the pathogen growth rate is overwhelming. The immune response of the infected individual cannot wipe out the pathogen, leading to sustained presence of pathogen along with persistent inflammation, tissue damage, lactate accumulation, organ dysfunction and eventually death.

Representative time courses of these outcomes appear in Fig. 3, the pathogen growth rate k_{pg} was chosen to achieve the various states, while the initial conditions were identical and all other parameters are kept at the values reported in Table 2. In the *healthy case* (Fig. 3a), as a response to the initial insult, there is a surge in N as phagocytes become activated and travel to the infected area to eliminate pathogens. This process induces tissue damage, represented by a rise in D, and a release of anti-inflammatory mediators, given by an increase in C_A. Both NO and lactate levels also increase, while energy supplies drop below baseline due to enhanced energy consumption associated with all of these processes. The model suggests that the patient would eliminate the pathogen and that subsequently, the levels of ATP and all other inflammatory indicators would return to baseline.

In the *aseptic case* (Fig. 3b), a similar set of processes begins in response to the elevated pathogen level. In the example shown, despite the initial inflammatory response, the pathogen population size grows before subsequently decaying. The elimination of pathogen requires a greater surge in the components of the inflammatory response and a correspondingly more substantial reduction in energy levels. Interestingly, although phagocyte activity causes a decrease in A_n, the drop in A_b, associated with the baseline immune response and various tissue damage and healing effects including C_A production, is even more pronounced.

Although the immune response eventually eliminates the infection and energy levels rise again, the associated elevation of phagocyte activation and pro-inflammatory effects cannot be fully countered by the anti-inflammatory mediators. In the long term, N tends to a non-zero value, D continues to grow, levels of both ATP pools remain below baseline, and sustained accumulation of both NO and lactate occurs. This sustained damage and other effects would be expected to cause organ dysfunction and death in patients.

The *septic case* also starts with a rise in levels of pathogen and immune agents (Fig. 3 c). As anti-inflammatory mediators accumulate, they cause mild reductions in N, X, and L, but P and D continue to rise. Energy levels fall and exhibit little (A_b) or no (A_n) recovery. Without elimination of pathogen, all immune components tend in the long term to elevated levels, with sustained energy depletion, which in patients would together result, as in the aseptic case, in severe tissue damage, organ dysfunction and death.

The example trajectories shown demonstrate clear relations between N, X, L, and both A_b and A_n. The presence of pathogens activates neutrophils, which leads to NO and lactate production. These three responses are clearly inversely proportional to ATP levels relative to baseline, or directly proportional to ATP consumption. High demand for neutrophil activation and other pro-inflammatory effects consumes large amounts of energy. In general we observe a strong relation between ATP levels and long term outcomes.

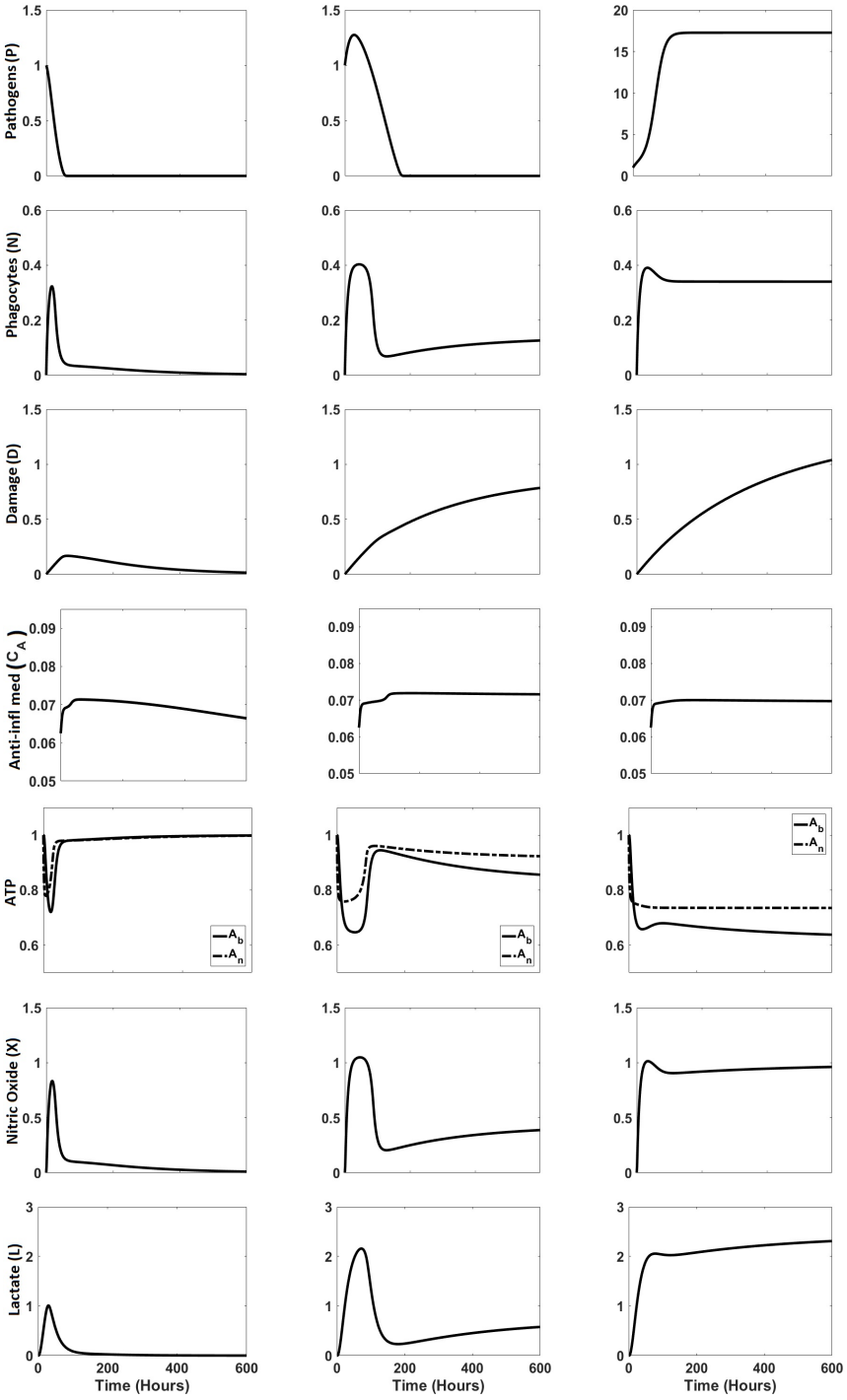

Figure 3: Transient behavior of model (1)-(8). Three outcomes are illustrated: (a) health, obtained by taking $k_{pg} = 0.01$, (b) aseptic, with $k_{pg} = 0.08$, and (c) septic, with $k_{pg} = 0.1$. The initial conditions in all three cases were identical: $P(0) = 1, N(0) = 0, D(0) = 0, C_A(0) = 0.0625, A_b(0) = 1, A_n(0) = 1, X(0) = 0, L(0) = 0$. Values for parameters other than k_{pg} are given in Table 2.

Each of the outcomes illustrated in Fig. 3 corresponds to an equilibrium point of system (1)-(8), as characterized in Table 3.

Table 3: Biologically significant equilibrium points

Name	Equilibrium Point
Health	$(P = 0, N = 0, D = 0, C_A > 0, A_b = 1, A_n = 1, X = 0, L = 0)$
Aseptic	$(P = 0, N > 0, D > 0, C_A > 0, 0 < A_b < 1, 0 < A_n < 1, X > 0, L > 0)$
Septic	$(P > 0, N > 0, D > 0, C_A > 0, 0 < A_b < 1, 0 < A_n < 1, X > 0, L > 0)$

We performed a bifurcation analysis of the model using XPPAUT ([31]) to explore more thoroughly the relations among these equilibrium points with respect to variations in the pathogen growth rate k_{pg}. Results are shown, projected onto the variables P , N , A_b, and A_n, in Fig 4, where stable equilibrium curves are presented as solid, unstable as dashed, and additional non-physiological bifurcation curves (e.g., with values for one or more variables negative) are not shown.

The healthy and aseptic equilibria, characterized by $P = 0$, both exist for $k_{pg} = 0$ and persist, with no change in equilibrium values of P, N, A_b, and A_n as k_{pg} increases. For sufficiently large k_{pg}, each of these equilibria loses stability by meeting an unstable equilibrium state in a transcritical bifurcation. These occur at $k_{pg} = 1.125$ and $k_{pg} = 1.143$, respectively; besides the destabilization of the healthy and aseptic states, these result in the previously unstable equilibria becoming stable but non-physiological (not shown). Well before these destabilizations, at $k_{pg} = 0.048$, the stable septic equilibrium point arises, along with an unstable equilibrium state, through a fold bifurcation. In fact, this unstable equilibrium is the same one that eventually participates in the transcritical bifurcation that destabilizes the aseptic state. Unlike the other two equilibria, the coordinates of the septic equilibrium do depend on k_{pg}, although they do already approach asymptotic values at relatively low k_{pg}.

Putting these results together, we observe that while the healthy and aseptic are bistable for $0 < k_{pg} < 0.048$, the model exhibits tri-stability for $0.048 < k_{pg} < 1.125$. Once the healthy

state loses stability, bi-stability between the septic and aseptic equilibria persists over the small range $1.125 < k_{pg} < 1.143$. Our model shows similar structure to the model presented in [61] in the sense that they both have the same three biologically relevant equilibrium points. Although the bifurcations of health and asepsis for our model occur for slightly lower values of k_{pg} than in the earlier work, the values are fairly close. On the other hand, the fold bifurcation introducing the septic state in our model occurs at a much smaller k_{pg} value than in [61].

This bifurcation analysis confirms that our model consistently exhibits a strong relation between low levels of ATP and sepsis. Similar results have been observed in human data, [12]. In particular, in Fig. 4c and Fig. 4d, we note that during sepsis, A_b attains an equilibrium at 0.62 while A_n drops to a new equilibrium at 0.73. The model analysis also verifies that accumulation of lactate and NO occurs during sepsis in general, although the projections of the bifurcation diagrams to these variables are not shown.

The bifurcation analysis shows that for our baseline parameter set, it is possible to choose the pathogen growth rate, k_{pg}, at a value for which either two or three physiologically relevant equilibrium points exist and are stable. For such a parameter set, different model trajectories will converge to different equilibria, selected by the choice of initial conditions for the model variables. In particular, by simulating model behavior over a long time period for each of a grid of values of k_{pg} and $P(0)$ (denoted by P_0), with all other parameters and initial conditions fixed, we can numerically explore how predicted outcome depends on the intensity of the pathogenic invasion. This simulation defines a basin of attractions for each type of equilibrium, defined as the set of (k_{pg}, P_0) for which the resulting trajectory converges to that equilibrium state. Fig. 5 displays the partitioning of the (k_{pg}, P_0) plane into basins of attraction resulting from this experiment. Note that the tristability observed in the bifurcation analysis here corresponds to the existence of a range of k_{pg} values at which a vertical line through the plot would intersect all three basins.

In the bifurcation diagram, asepsis looses stability at $k_{pg} = 1.143$, while in the basin of attraction, asepsis seems to disappear at about $k_{pg} = 0.2$. This apparent contradiction occurs because the basin of attraction and the bifurcation diagrams are obtained through different approaches. On the one hand, the basin of attraction is computed by solving the

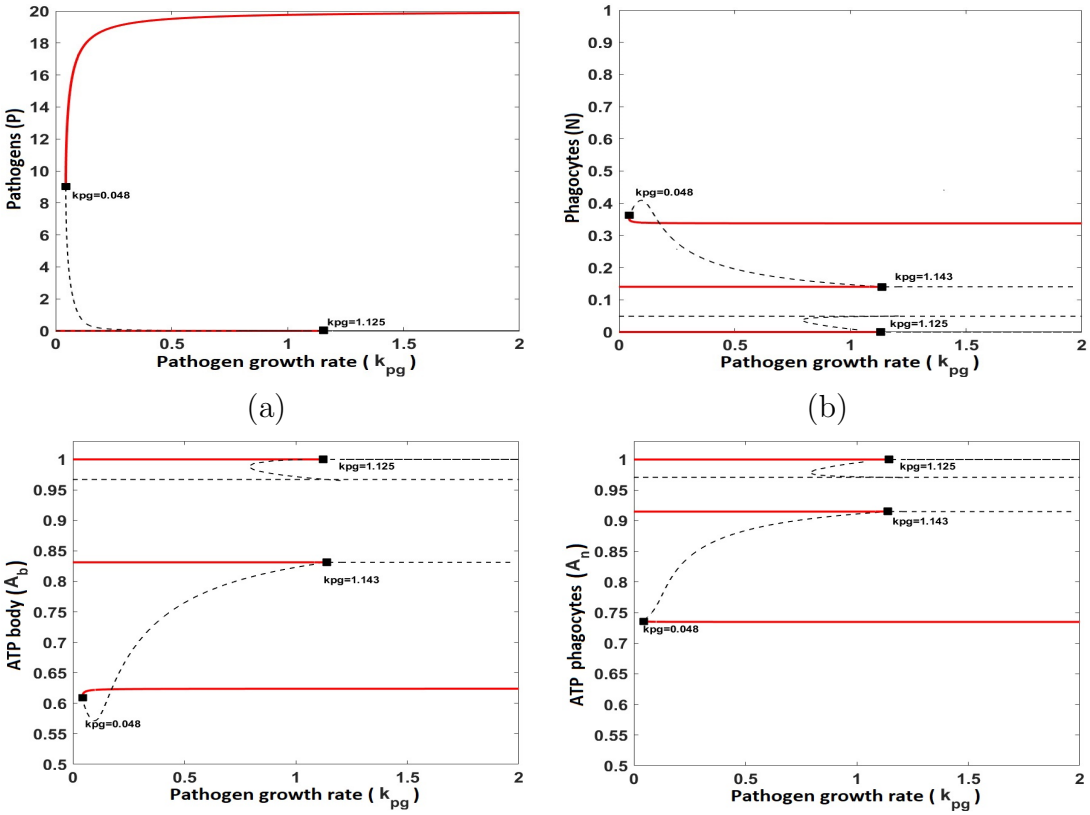

Figure 4: Bifurcation diagrams for the system of equations (1)-(8). Equilibrium states are illustrated with solid red curves (stable), shown with dashed curves (unstable), or not shown at all if non-physiological. The three stable equilibrium points correspond to healthy, aseptic, and septic states. Health loses stability at a transcritical bifurcation at $k_{pg} = 1.125$. The aseptic state loses its stability at a transcritical bifurcation at $k_{pg} = 1.143$. At $k_{pg} = 0.048$, a fold bifurcation gives rise to the septic equilibrium point. (a) Bifurcation diagram for P versus k_{pg} . Here both healthy and aseptic equilibrium points coincide at $P = 0$. (b) Bifurcation diagram for N versus k_{pg}. (c) Bifurcation diagram for A_b versus k_{pg}. (d) Bifurcation diagram for A_n versus k_{pg}. All parameters other than k_{pg} are as in Table 2.

model on a grid of values of k_{pg} and P_0 and with the remaining initial conditions fixed at baseline levels. On the other hand, the bifurcation diagrams are found by studying the

eigenvalues of the jacobian of the system (1)-(8). More precisely, the initial conditions do not play a role in the classification of equilibrium points, but they do in the computation of the basins of attraction. What the bifurcation diagram suggests is that there must be some initial conditions where asepsis exists and is stable for $k_{pg} \in (0, 1.143)$.

The basin of attraction results are not as exact as the bifurcation analysis because they are based on simulations with finite time horizons, which may yield faulty conclusions in borderline cases in which pathogen are eliminated only after extremely long time periods, and because they are limited to a finite range of P_0 values. Nonetheless, they represent a valuable complement to the bifurcation analysis. They show, for example, that values of P_0 needed to produce septic outcomes for low k_{pg} (e.g., < 0.06) are relatively quite high (e.g., > 2), well above the level where healthy outcomes are no longer possible. This diagram is also useful in that it represents a prediction of the outcome of a standardized patient, characterized by our baseline parameter set and baseline initial conditions for all variables other than P, when exposed to a pathogen for which the growth rate and initial load are known.

2.4 Model application to altered metabolic states

Some altered metabolic states such as hypoglycemia, hyperglycemia, and hypoxia have been found to compromise the performance of the immune response against infection. With small variations our model can be used to study these three energetically dependent conditions. We compare the performance of our model with existent literature about the relation between these three conditions and sepsis.

Hypoglycemia is defined as low blood glucose or low blood sugar. Insufficient glucose in the blood will compromise the production of ATP and as a consequence it will reduce the effectiveness of the immune system in fighting the infection. Hyperglycemia, also known as high blood glucose, activates protein kinase C, which inhibits neutrophil activities such as migration, phagocytosis, apoptosis, and killing of microbes. Finally, hypoxia is characterized by the lack of the necessary oxygen to accomplish metabolic requirements. When an inad-

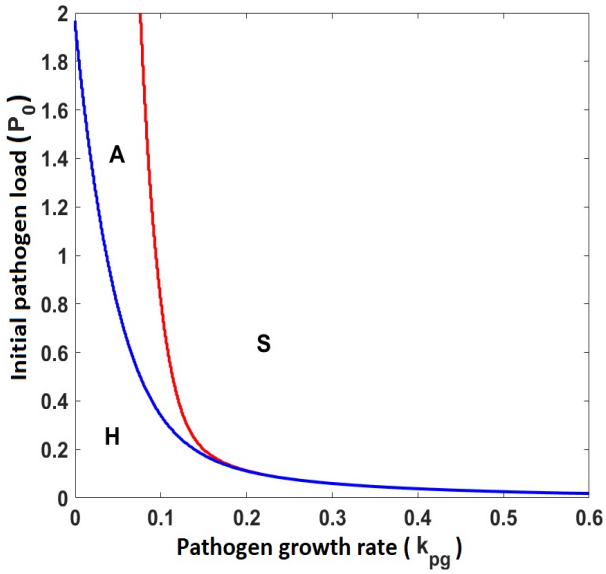

Figure 5: Basins of attraction of healthy (H), aseptic (A), and septic (S) equilibria for equations (1)-(8). The healthy region is bounded by the coordinate axes and the solid blue curve, the aseptic region lies between the solid blue and red curves, and the septic region is above the red solid curve. All the parameters and initial conditions except k_{pg} and P_0 were taken as in Table 2 and Fig. 3.

equate amount of oxygen reaches the tissues, cellular respiration (production of ATP) must rely more heavily on anaerobic glycolysis. Also, pro-inflammatory cytokine levels increase, causing inflammation and tissue damage during hypoxia.

2.4.1 Hypoglycemia

It seems natural to suggest that hypoglycemia in vivo involves a decrease in glucose production, an increase in glucose demand, or both. Possible factors contributing to hypoglycemia include depletion of glycogen stores, impaired gluconeogenesis and increased peripheral glucose utilization, [54]. In a study performed in rats by [48], it was found that during sepsis there is an increase in glucose utilization by macrophage-rich-tissues that could lead to hy-

poglycemia.

Several studies have been conducted to understand the relation between hypoglycemia and sepsis. In a study performed on nine human patients, [54] observed that hypoglycemia was associated with overwhelming sepsis. In fact, in four of these patients, sepsis was the only cause of hypoglycemia. In five patients, another possible cause for hypoglycemia was present (alcoholism and chronic renal insufficiency). All patients exhibited metabolic and/or respiratory acidosis. Although serum lactate was not measured, their metabolic acidosis was presumably secondary to lactate accumulation.

Because our model does not contain an equation for glucose, but glucose is the fuel for ATP production, we indirectly represented the effects of hypoglycemia by a reduction in the rate of ATP production in equations (5)-(6). As we observed in our bifurcation analysis, the state variables A_n and A_b are always between 0.6 and 1. One can easily check that the behavior of the function $c(A_x)$ is mostly governed by the parameter k_1 in this range of A_x. Therefore, to lower the ATP production rate, we decreased the control parameter k_1, which resulted in reduced A_n and A_b levels. Lowering A_b availability affects the healing process as well as the production of anti-inflammatory cytokines and the response of nonspecific immune cells. On the other hand, reducing A_n impacts the production and activation of neutrophils, undermines pro-inflammatory cytokine production, and slows phagocytosis.

Several studies have also found that hypoglycemia increases leukocytes and circulating pro-inflammatory cytokines, [56, 60]. To include this effect, we also increased the parameter s_{nr}, which controls the rate of phagocyte production, by 25%. Combining this change with the alteration in k_1, we found the same three physiological equilibria as in our baseline case and we recomputed the basins of attraction for these states.

As a result of the pro-inflammatory and energy effects of hypoglycemia, the lower boundaries of the basins for both the septic and aseptic equilibria shifted to smaller P_0 values, at the expense of healthy and aseptic territories, respectively (Fig. 6). The shift from health to an aseptic state was particularly pronounced for small k_{pg}. The shift from aseptic to septic, on the other hand, took the form of a translation of the boundary between the two outcomes to a lower k_{pg} level, fairly uniformly in P_0. In general, our results agree with the findings of [54] that hypoglycemia promotes sepsis, while providing a more detailed specification of

how outcomes of pathogen invasion under hypoglycemia are predicted to depend on invasion characteristics.

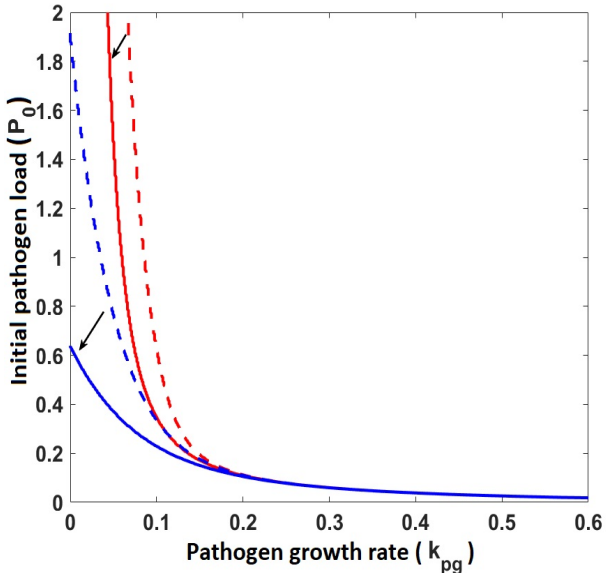

Figure 6: Basins of attraction for hypoglycemic versus normal states. The dashed blue and red lines correspond to the baseline boundaries distinguishing aseptic from healthy and septic outcomes, respectively, as shown in Fig. 5. The blue and red solid lines indicate the new boundaries in the presence of hypoglycemia. The arrows highlight the direction of the shift that occurs with hypoglycemia induction. To represent hypoglycemia, we took $k_1 = 1$, $s_{nr} = 0.2$, and all remaining parameter values are as in Table 2.

2.4.2 Hyperglycemia

Septic patients may become hyperglycemic due to a combination of various factors. For instance, they may experience increases in insulin clearance, causing a reduction in insulin-mediated glucose uptake. Septic patients may also develop hyperglycemia due to adverse effects of certain therapies such as glucocorticoids or sympathicomimetic drugs. Additionally, insulin resistance, which is proportional to the severity of the stress response, also promotes hyperglycemia, [52].

Although hyperglycemia might naively be expected to benefit the inflammatory response by providing extra fuel to support pathogen elimination, it has in fact been found to have negative impacts on acute immune-related outcomes. In particular, in a study conducted on 62 patients with severe sepsis, [49] found that stress hyperglycemia is related to high elevated cytokine levels (IL-6 and TNF-α) and the severity of the disease. Moreover, it is known that hyperglycemia increases vascular permeability as well as inflammatory cytokine levels, altering the balance between anti-inflammatory and inflammatory cytokines in a way that might promote run-away inflammation. It also increases neutrophil adherence, which inhibits cellular migration at sites of inflammation. Finally, hyperglycemia can actually suppress neutrophil activity including metabolism, phagocytosis and microbial killing. These effects could lead to an increase in infection intensity and cause tissue damage, [43].

To simulate a hyperglycemic state in a simple way with our model, we decreased the rate of phagocytosis and microbial killing by 25%, setting $k_{pn} = 0.5625$. Similarly, we reduced parameters associated with phagocyte recruitment and metabolism, decreasing their production and depletion rates by 15%, setting $s_{nr} = 0.136$ and $\mu_n = 0.085$; the choice of 15% rather than 25% here was made to represent compensation due to increased vascular permeability. Together, these changes not only slow down the immune system response but they also more generally affect the subsequent time course of inflammation. Interestingly, these changes lead to somewhat similar shifts in basins of attraction as occur with hypoglycemia, namely shrinking of the healthy region and a shift in the aseptic region to lower k_{pg} levels; see Fig 7. Our model predicts milder effects of hyperglycemia than hypoglycemia, however; specifically, the extent of the septic region does not change as significantly in hyperglycemia and the change in the aseptic basin at small k_{pg} is milder. Nonetheless, our model agrees with the literature suggesting that hyperglycemia promotes sepsis, again with detail about possible dependence on pathogen properties.

2.4.3 Hypoxia

Hypoxia-induced inflammation and inflammation during hypoxic conditions in the context of several human diseases have been studied in a variety of recent publications, [29]. For

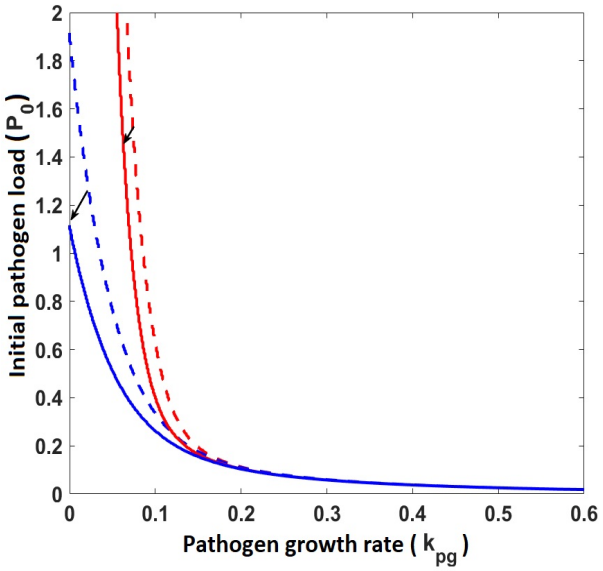

Figure 7: Basin of attraction for hyperglycemic versus normal states. The dashed red and blue lines indicate the septic and healthy boundaries in the baseline scenario shown also in Fig 5. The solid red and blue lines indicate the boundaries with the introduction of hyperglycemia. The arrows indicate the direction of the transition. To represent hyperglycemia, we set $s_{nr} = 0.136$, $\mu_n = 0.085$, and $k_{pn} = 0.5625$. All the other parameters were taken as in Table 2.

instance, people with mountain sickness have exhibited increasing levels of pro-inflammatory cytokines as well as pulmonary or cerebral edema, [64, 38, 35]. In another study, healthy volunteers experienced higher levels of IL-6 and other pro-inflammatory cytokines after spending 3 nights at an elevation above 3400 m, [39]. Also, studies in mice have found that after short-term exposure to low oxygen concentrations, vascular leakage, accumulation of inflammatory cells and high levels of cytokines occur [29]. Further, ischemia and reperfusion injury have been associated with inflammatory responses that lead to subsequent organ dysfunction [30, 5].

We represented the pro-inflammatory effects of hypoxia in our model by increasing the

parameter s_{nr} by 12.5%. Moreover, the reduced oxygen availability was addressed by introducing a new parameter $0 < \epsilon_H < 1$ and replacing $f(X/X^*)$ by $\epsilon_H f(X/X^*)$ in equations (5), (6) and $(1 - f(X/X^*))$ by $(1 - f(X/X^*))\epsilon_H$ in equation (8). Recall that equation (8) represents enhanced lactate production due to diminished function of the aerobic pathway with rising X. The latter adjustment therefore implements a decrease in this additional lactate production, since for each X, the aerobic pathway is less active under hypoxic than control conditions.

As a result of these modifications, as seen in Fig. 8, the basin of attraction of the healthy state shrinks, making the aseptic outcome more likely. On the other hand, the septic region hardly changes in the presence of hypoxia, suggesting that hypoxia does not promote sepsis. This outcome is natural because the lack of oxygen does not affect A_n, which is the energy needed to produce inflammation. It does cause a reduction in the supply of A_b, however, which is the energy needed for healing and anti-inflammatory cytokine production, such that an over-exuberant pro-inflammatory response can result. These results are also consistent with the observations in a previous computational model that for low values of k_{pg}, such reduction in anti-inflammatory cytokines promotes aseptic outcomes [61].

In general, our results suggest that maintaining patients blood sugar within an euglycemic range might be beneficial for recovery from sepsis as long as the pathogen load and pathogen growth rate are under moderate levels as well. Also, regulating oxygen delivery improves the chances of recovery as long as the patient is in aseptic state.

2.4.4 Survival analysis

So far, we have discussed results of a variety of simulations using our baseline parameter values given in Table 2 with variations in k_{pg} and P_0, as well as some outcomes from modifications of a few specific parameters designed to represent effects of certain altered metabolic states. A more realistic situation would be to consider a heterogeneous collection of parameter sets, representing the variability inherent in actual patient populations.

We adopted this heterogeneity to generate predictions about survival rates among a population of 300 virtual patients. We introduced variability in those parameters on which

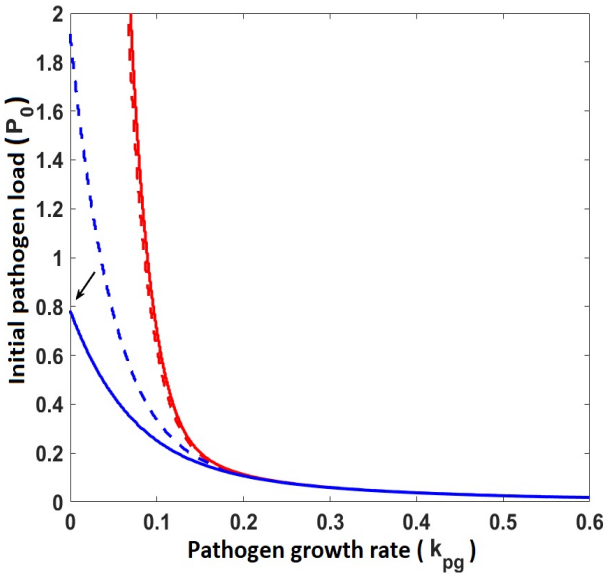

Figure 8: Basin of attraction for hypoxic versus normal states. The dashed blue and red curves indicate the healthy and septic boundaries for the baseline case as shown in Fig. 5. The solid blue and red curves indicate these boundaries in the presence of hypoxia. The arrow indicates the direction of the transition. To obtain hypoxia we take $s_{nr} = 0.18$ and set the new parameter $\epsilon_H = 0.5$ (see text), which diminishes the output of the aerobic pathway for energy production. All other parameter values were taken as in Table 2.

we found that the model outcomes depended most sensitively. Specifically, we determined the set of most sensitive parameters in the model by computing the relative sensitivities $(\partial x(t)/\partial\theta)(\theta/x(t))$, where $x(t)$ corresponds to the vector of state variables and θ is the vector of parameters. The healthy state was taken as a baseline for generating $x(t)$, which included the variables P, N, and D. Choosing a sensitivity threshold of 0.09, we obtained the following subset of sensitive parameters:

$$k_{pg}, k_{pm}, k_{mp}, k_{pn}, s_{nr}, k_{np}, k_{nd}, \mu_n, k_{dn}, \mu_d, s_c, \mu_c, c_3, \mu_A, C^*, k_1 \tag{9}$$

In addition to these, we also included variability in the initial levels of anti-inflammatory mediators, C_{A_0}, and the pathogen load, P_0. Therefore, to generate each virtual patient, a

total of 16 parameters and two initial conditions were perturbed randomly from their baseline value given in Table 2. We let k_{pg} and P_0 be uniformly distributed on the intervals $[0, 0.2]$ and $[0, 0.45]$, respectively, so that the outcomes of simulations of virtual patients were not driven primarily by pathogen-dependent parameters but by the parameter set as a whole. On the other hand, the remaining parameters, including the initial condition C_{A_0}, were taken to be normally distributed around their baseline values with a standard deviation of $\sigma = 0.2$ relative to the size of each parameter with the exception of k_1, for which we used a smaller standard deviation of $\sigma = 0.03$ so that every patient would have relatively similar energy availability as the baseline level defined by the parameters in Table 2.

After producing our population of 300 virtual patients, we simulated the time courses of their inflammatory responses until they clearly approached one of the model equilibrium states, healthy, aseptic, or septic. Each virtual patient was assigned an outcome based on its asymptotic behavior. Fig. 9 depicts the outcomes, projected to the plane of the patients' P_0 and k_{pg} values. Note that, while lower (higher) k_{pg} and P_0 are naturally associated with more healthy (septic) outcomes, outcomes were certainly not dictated by this parameter pair but rather were intermingled in many regions of the plane. Of the model patients, 60.7% were classified as healthy, 19% as aseptic, and 20.3% as septic.

For those patients with aseptic and septic outcomes, we used our model to assign each a time of death. To do so, we considered levels of lactate and damage, which are associated with appraisals of patient status in clinical settings. Based on comparisons across long-time simulations, we determined that the maximum observed damage provided the most reliable separator between patients with healthy outcomes, or survivors ($n = 182$), and other patients, or non-survivors ($n = 118$). Specifically, we found that for all 300 virtual patients, $D(t) < 0.30635$ for the full simulation time if and only if the patient was in the survivor group. Thus, we defined the time of death of each non-survivor patient be the moment when the damage trajectory hits 0.30635 units. As one can notice from Fig. 10, the same separation would have also resulted from using any other value between 0.30635 and 0.5 as the designated damage threshold. Based on the damage threshold, we plotted the fraction of patients classified into each outcome group and of the total population that were still alive, with damage not yet exceeding threshold, as a function of time (Fig. 11a). The

surviving fraction among septic patients dropped faster than among aseptic patients, with full loss of survival before 350 hours.

Finally, we explored how the conditions of altered metabolism discussed in subsection 2.4 affected survival trajectories among virtual patients. For each condition, we created a new group of virtual patients. To do so, we started from the baseline population we had already generated and we modified parameters in a way that was consistent with the desired condition. Specifically, to represent hypoglycemia in the population, we decreased k_1 by 66.67% for each patient and we increased each patient's s_{nr} value by 25%. As a result, the percentage of healthy patients dropped to 50.3%, the aseptic population size decreased to 23%, and the septic population fraction increased to 26.7%. As shown in Fig. 11b, the aseptic hypoglycemic patients die at similar rate than in the normal (euglycemic) case, except that a tail of longest surviving patients is lost. Due to the enhanced pro-inflammatory effects and the lack of energy associated with hypoglycemia, the hypoglycemic septic patients die at a faster rate than the euglycemic ones. The overall acceleration of death by hypoglycemia can also be observed in Fig. 11b, where combined survival curves are displayed.

Next, we induced hyperglycemia in the virtual patients by reducing their k_{pn} values by 25% and both s_{nr} and μ_n by 15%, just as we did to represent hyperglycemia from our baseline parameter set. As a result, the percentage of healthy patients was reduced to 56.3%, the aseptic population decreased slightly to 17%, and the septic population increased to 26.7%. The survival curves of the virtual hyperglycemia population are shown in Fig 11c. When looking individually at the septic population, it is difficult to distinguish a significant difference between hyperglycemic and euglycemic death rates. The hyperglycemic aseptic population however dies at a faster rate compared to the euglycemic population and consequently the tail of longer survival patients dies out sooner again. The overall death rate in the population of hyperglycemic patients is indeed faster than in the euglycemic population, however (Fig 11c).

In general, our model suggests that hypoglycemic septic patients die at a faster rate than the hyperglycemic and euglycemic patients. In particular, in Fig. 12a we show the overall survival curves for the 4 populations (euglycemic or healthy, hypoglycemic, hyperglycemic, and hypoxic) for a period of 15 days. Here, we have shifted the x-axis so that day 0 starts at

the 55 hour time point from the other panels, which is about the time the virtual patients start to die. For model validation, we compared the qualitatively behavior obtained in our simulations with a study performed in 418 Ugandan patients with severe sepsis, where 16.3% of the patients were diagnosed as hypoglycemic and 50.2% as hyperglycemic. Among these patients, the hypoglycemic cohort died at a faster rate than the hyperglycemic patients and both died faster than the euglycemic patients, [70]. The survival curves of the euglycemic, hyperglycemic, and hypoglycemic patients in this study are reproduced in Fig. 12b and their results are consistent with our simulations shown in Fig. 12a.

To finish, we represented hypoxia among the virtual patients by increasing the inflammatory parameter s_{nr} by 12.5% and set $\epsilon_H = 0.5$ to represent a 50% reduction of oxygenation. As a result, the percentage of healthy individuals dropped to 53%, the aseptic population size increased to 28%, and the septic component decreased slightly to 19% of the population. These results are consistent with what we observed in the basins of attraction in Fig. 8: hypoxia promotes the aseptic state and diminishes health, with relatively little impact on the likelihood of septic outcomes. The survival curves for the hypoxic population are depicted in Fig. 11d. Here we observe that hypoxic patients with sepsis die at a faster rate than non-hypoxic septic patients and overall, hypoxic non-survivors die faster than non-survivors in the non-hypoxic group.

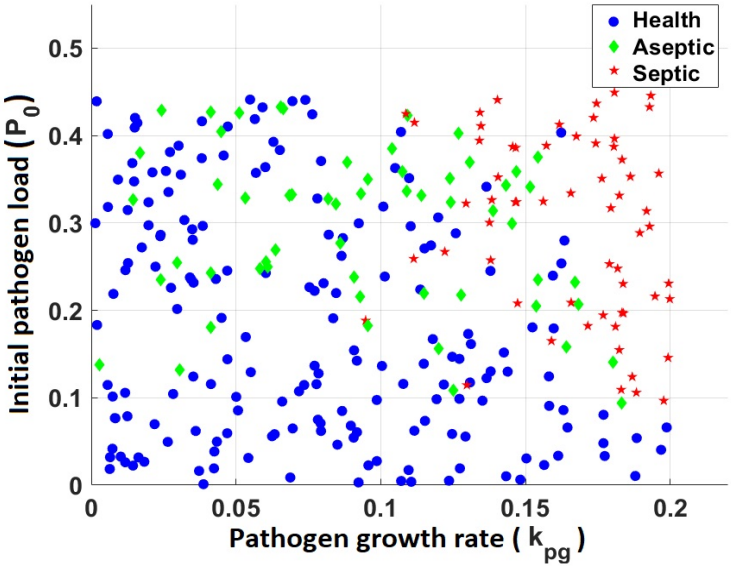

Figure 9: Representation of outcomes for a population of 300 virtual patients on k_{pg} versus P_0 plane.

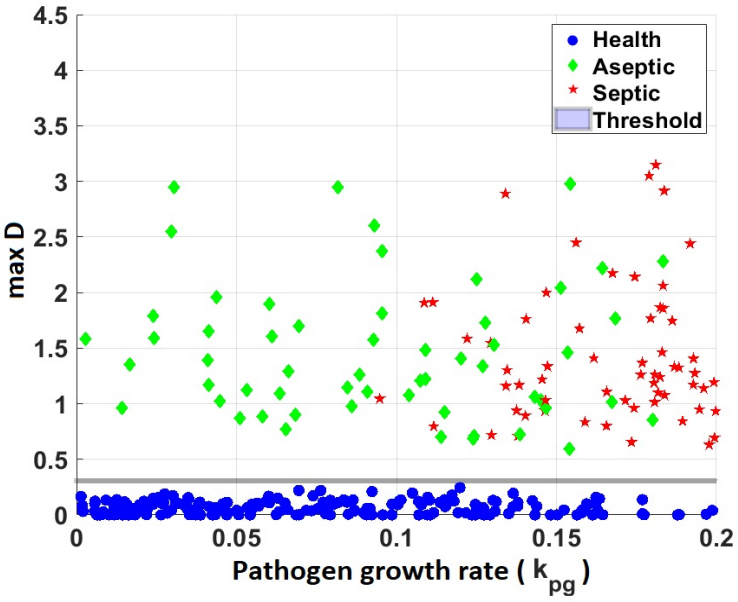

Figure 10: Representation of outcomes for a population of 300 virtual patients on the k_{pg} versus max D plane. Projection with respect to P_0 and the maximum damage value attained over the course of patient simulation. The solid gray line indicates the threshold of 0.30635 units of damage used to separate survivors and non-survivors.

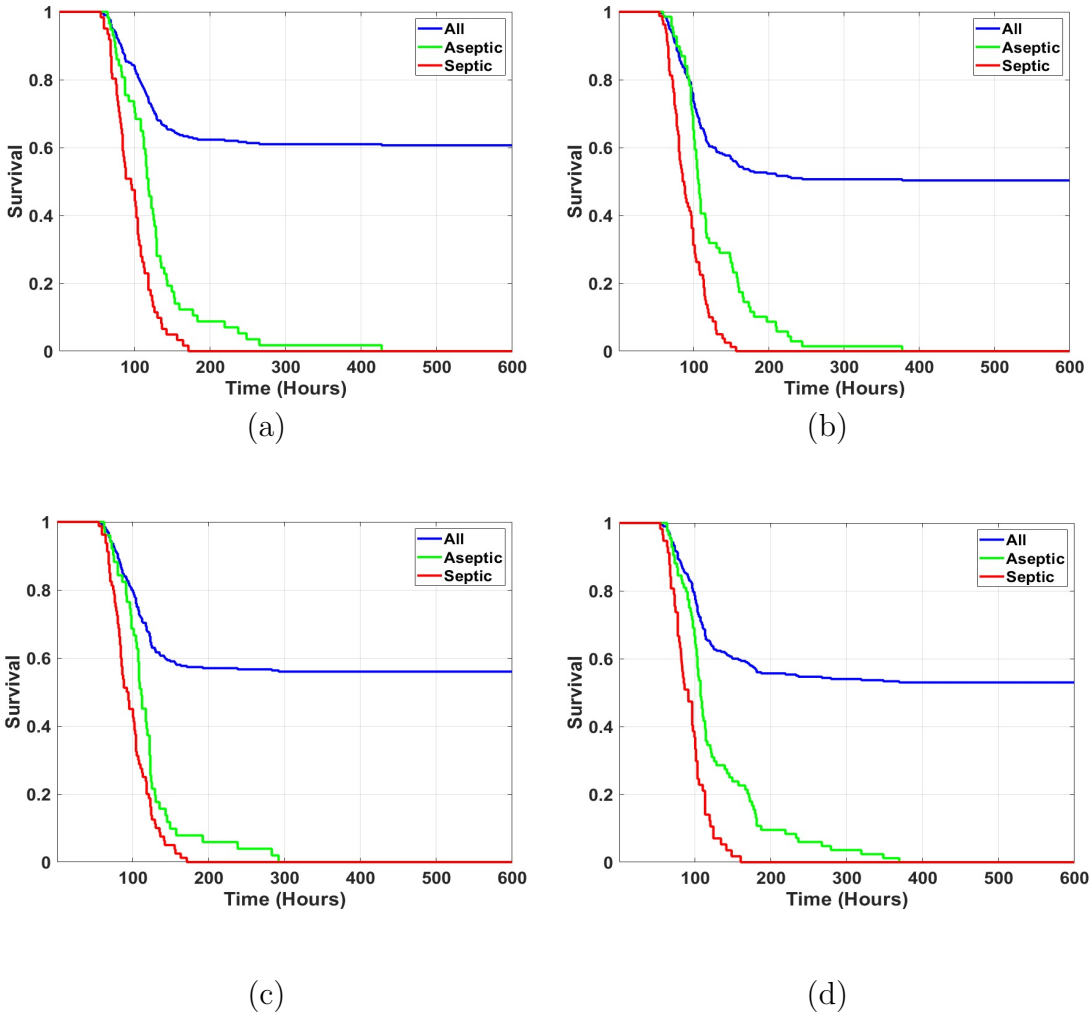

Figure 11: Survival curves of the 300 virtual patients across metabolic conditions. (a) Baseline euglycemic or normal population. (b) Hypoglycemic population. (c) Hyperglycemic population. (d) Hypoxic population. The red solid lines show fraction surviving from the septic group, the green correspond to the aseptic group, and the blue combines healthy, septic, and aseptic subjects.

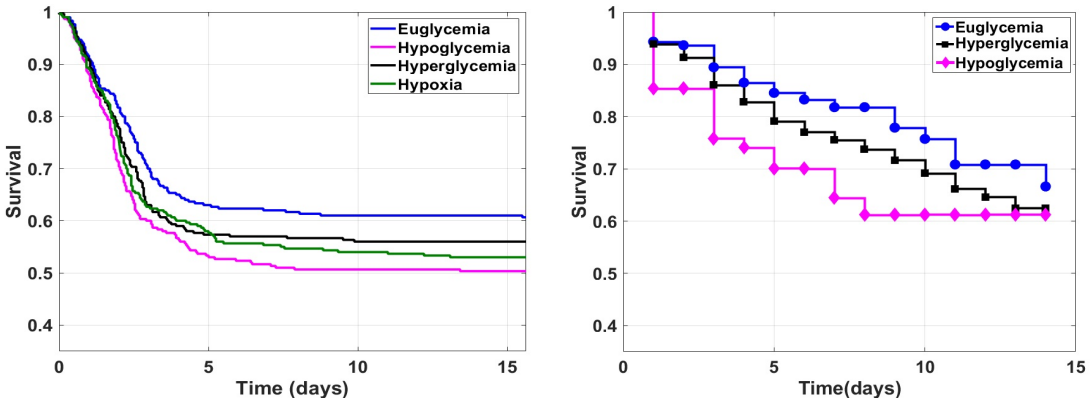

(a) (b)

Figure 12: (a) Survival curves of the total euglycemic, hypoglcemic, and hyperglycemic virtual patient populations. The 15 day time courses shown correspond to the range from 55-415 hours of the virtual population simulation shown on Figures 11(a)-(d). (b) Data from three Ugandan hospitals in 2011; figure adapted from [70].

.

2.5 Discussion

In this chapter, we present a reduced model system that describes the dynamics of the immune system in the presence of pathogens and incorporates energy production along with the energy requirements that arise in fighting such an infection. To the best of our knowledge, this is the first model that incorporates these features. This model builds on several previous models representing various aspects of the acute inflammatory response [61], [47], [19], [26], [24], [57]. In addition to two ATP components, our model includes an equation for lactate, which can be measured experimentally in patients and thus will allow us to fit the model to data in future work.

From the point of view of dynamical systems, the model presents an interesting bifurcation structure with respect to variations in k_{pg}. In particular, tri-stability among healthy, aseptic, and septic states can be achieved for fixed values of k_{pg}, as in previous models [61], which reflects a realistic tuning in that the same patient could end up in any one of these three states, depending on infection severity. While bifurcation analysis indicated which equilibrium states are present and over what ranges of k_{pg} they are stable, we also considered the basins of attraction of these states, which indicated the practical relevance of the available stable equilibria in terms of the levels of P_0 needed for them to emerge.

Our results show that both the energy supply to phagocytes and that to other cells in the body play fundamental roles in sepsis. As an infection progresses, the high level of ATP usage associated with the inflammatory response drives augmented energy production as well as a large accumulation of lactate, overproduction of NO, further inflammation, and tissue damage, which in patients could lead to organ dysfunction and death. In general, all of these findings are consistent with experimental data [12], [13], [14]. The inclusion of energy dynamics in the model induced a reduction in the healing capacity of the inflammatory process due to limitations on pro-inflammation, pathogen elimination, and healing of damage imposed by energy consumption. Moreover, it allows us to simulate hyperglycemia, hypoglycemia, and hypoxia and to explore their effects on the inflammatory response. In particular, the immune consequences of hyperglycemia and hypoglycemia promote sepsis and make health and recovery less likely. We also observed that hypoxia favors an aseptic outcome and does

not have a crucial effect on sepsis. This result arises because the non-phagocyte related energy demands in the model rely more on the aerobic ATP production pathway, whereas the energy supply associated with phagocytes and pro-inflammation is more biased towards the anaerobic route.

We created 300 virtual patients by introducing variability in a sensitive subset of model parameters. We included heterogeneity in k_{pg} among this virtual population to reflect the reality that in any infected patient population, infections of disparate severities would be represented. Based on outcomes arising in simulated infections, we subdivided our virtual patient population into survivors and non-survivors. We predicted the times of death for the non-survivors via a threshold that we defined based on the damage level in each simulated patient.

The biological conclusions that can be drawn from our model are, however, limited by the fact that the model is simplified and does not consider many other interactions that occur in the immune system during infection. One of the weaknesses of the model is that it assumes that values of all parameter are kept fixed through the entire time course of infection, which is not entirely realistic. For example, with parameter variation over time, the model could account for metabolic re-programming or the ability of tissue to survive by shutting down non-essential function and thus decreasing damage, [66]. Another aspect of the model that could merit refinement in future work is the definition of death. We defined time of death as the moment when the D trajectory exceeded a certain threshold. However, the level of an appropriate "death threshold" could not be derived directly from biological principles and depends on the extent of variability that we included in the virtual population.

3.0 A data-driven model of the role of energy in sepsis

3.1 Introduction

The work presented in Chapter 2 was purely theoretical and did not involve any data calibration. In this chapter we present a data-oriented model that builds up in the model presented in chapter 2. The goal here is to extend our initial model to one that can be fitted with available animal data and that can eventually be used to better understand the role of energy in sepsis and that can help physicians to make more informed decisions when dealing with septic patients.

This chapter is organized as follows. We start in Section 3.2 by describing the origin and details about the available animal data. We continue in Section 3.3 with a complete description of the extended model. Lastly, in Section 3.5, we present sample health, aseptic, and septic trajectories, including parameter values and initial conditions.

3.2 Experimental data

In this section we present the experimental data that is used to develop our extended model. This data was originally collected and studied by Schlag et. al in [62]. In this study, thirty-three baboons of the species Papio ursinus were sedated and intravenously infused with 2×10^9 colony forming units per kilogram of Escherichia coli (E. coli) at the beginning of the experiment over a period 2 hours. Subjects received fluid resuscitation (Ringer's solution 10 ml/kg/h) and antibiotic therapy throughout the experiment (gentamycin 4mg/kg every 12 h).

Several measurements were taking for a lapse of 28 days. However, we are just interested in 5 of the observed variables: elastase (ng/mL), glucose (mg/dL), lactate ($mmol/L$), lipopolysaccharides (pg/mL) (LPS), and nitrate ($\mu mol/L$).

Elastase is an enzyme secreted by neutrophils during inflammation. It can therefore

be directly compared to the number of activated neutrophils. Glucose is the main source of fuel to sustain any biological process. Lactate is a byproduct of anaerobic respiration and it is produced by a process called fermentation. LPS are molecules found in the outer membrane of bacteria. Therefore, LPS release occurs whenever bacteria membrane is broken during pathogen elimination. Nitrate is a byproduct of nitric oxide. Units will be consistent throughout this thesis and we will not explicitly indicate them on figures. All measurements were taking in hours at times $t_1 = 0, t_2 = 2, t_3 = 4, t_4 = 6, t_5 = 11, t_6 = 23, t_7 = 35, t_8 = 47, t_9 = 72, t_{10} = 144, t_{11} = 672$.

Originally the experiment was designed to investigate the therapeutic effects of a nitric oxide synthase (NOS) inhibitor, NG-monomethyl-Larginine (L-NMMA), on septic shock by comparing two groups: the *placebo or non-treated* group which corresponds to those animals that where not given any therapy during the experiment and the *treated* group which was administered with the NOS inhibitor. The NOS inhibitor treatment L-NMMA began after hour 12 on 16 subjects and was continuously administered during 36 hours, i.e. until hour 48 of the experiment. Animals were treated in accordance with National Institutes of Health guidelines. The experimental protocol was reviewed and approved by the Institutional Animal Care and Use Committee of Biocon Research Laboratories, Pretoria, South Africa [62].

We further classified the 33 subjects into two more groups: the *survivors* are the group of subjects that lived until at least the first 144 hours from the beginning of the experiment and the *non-survivors* which were subjects who died before 144 hours. These two groups will be labeled by their subject number assigned in the original experiment and preceded by a capital S to indicate survivors or by NS to indicate they are non-survivors.

To account for different scales and high variability across the observable variables, we take the natural logarithm of the measurements. In Fig. 13 we show the observable variables of the 4 placebo survivor subjects S89, S90, S100, and S101, where we are plotting the time in logarithmic scale for better visualization. Similarly, Fig. 14 depicts the data of the placebo non-survivors, NS66, NS67, NS69, NS73, NS74, NS76, NS80, NS88, NS92, NS97, NS98, and NS104. We considered subject S75 (not shown) to be an outlier as its measurements were considerably different from the other subjects, in at least one of the observable variables

that we are taking under consideration. Fig. 15 shows the data for the survivors that were treated with the NOS inhibitor, S91, S93, S95, S99, S102, S103, S106, S70, S72, S77, S79, and S83, whereas Fig. 16, shows the time series for the non-survivors that were treated, NS68, NS71, NS78, NS94.

There is no apparent reason for the glucose rise in mostly every subject at times $t = 35$ hours, $t = 47$ hours, and $t = 72$ hours. Although it is not mentioned in the experimental study, we conclude the subjects must had been fed at day 2. As the purpose of our study is to understand how energy is consumed by the immune response, we are going to disregard these three time points in glucose for every subject.

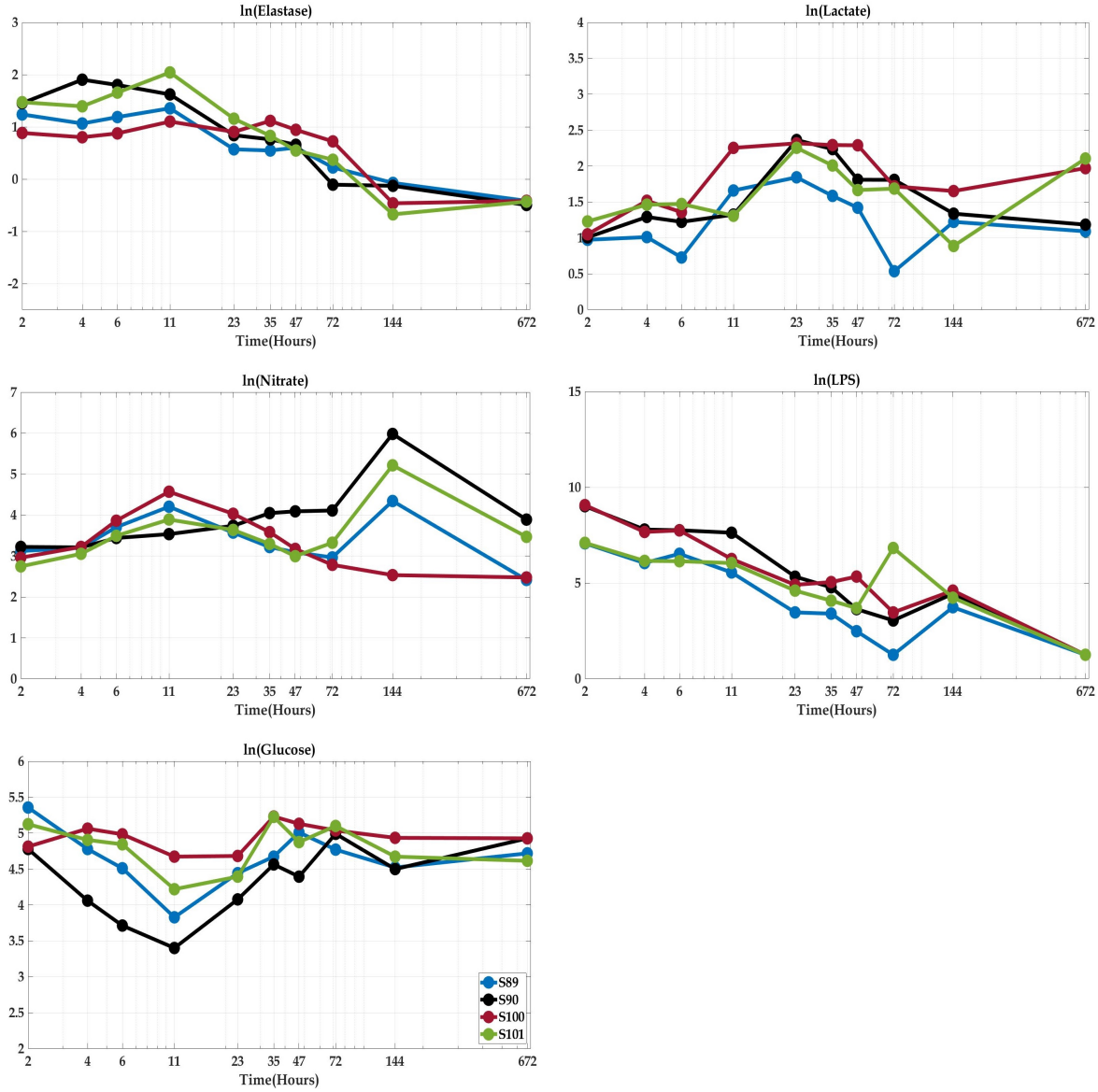

Figure 13: Time series trajectories of the observable variables for the survivors non-treated subjects. The x-axis is in logarithmic scale for better visualization. For this reason the time at $t = 0$ is not shown. The y-axis contains the logarithm of the observable variables.

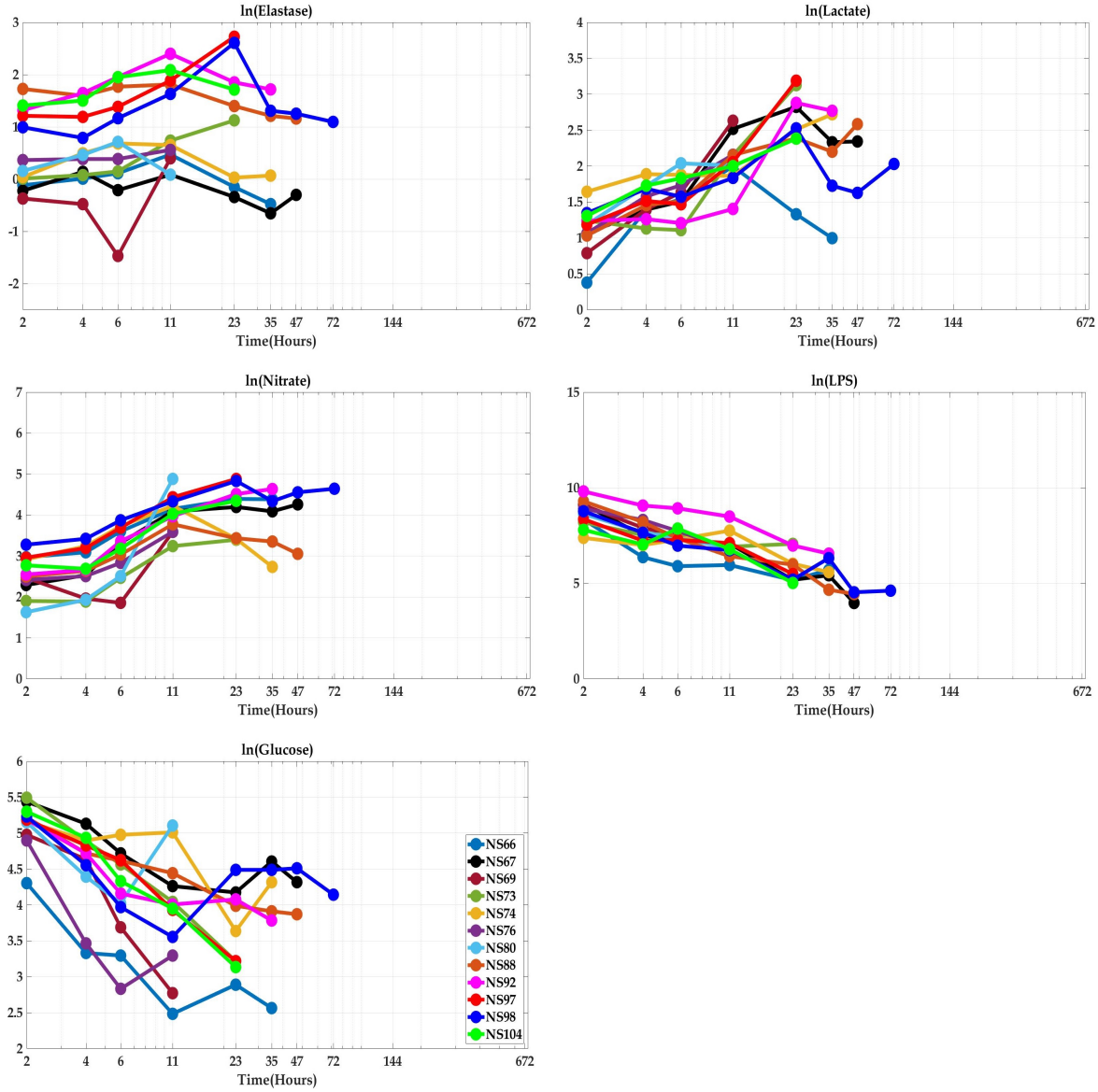

Figure 14: Time series trajectories of the observable variables for the non-survivors non-treated subjects. The x-axis is in logarithmic scale for better visualization. For this reason the time at $t = 0$ is not shown. The y-axis contains the logarithm of the observable variables.

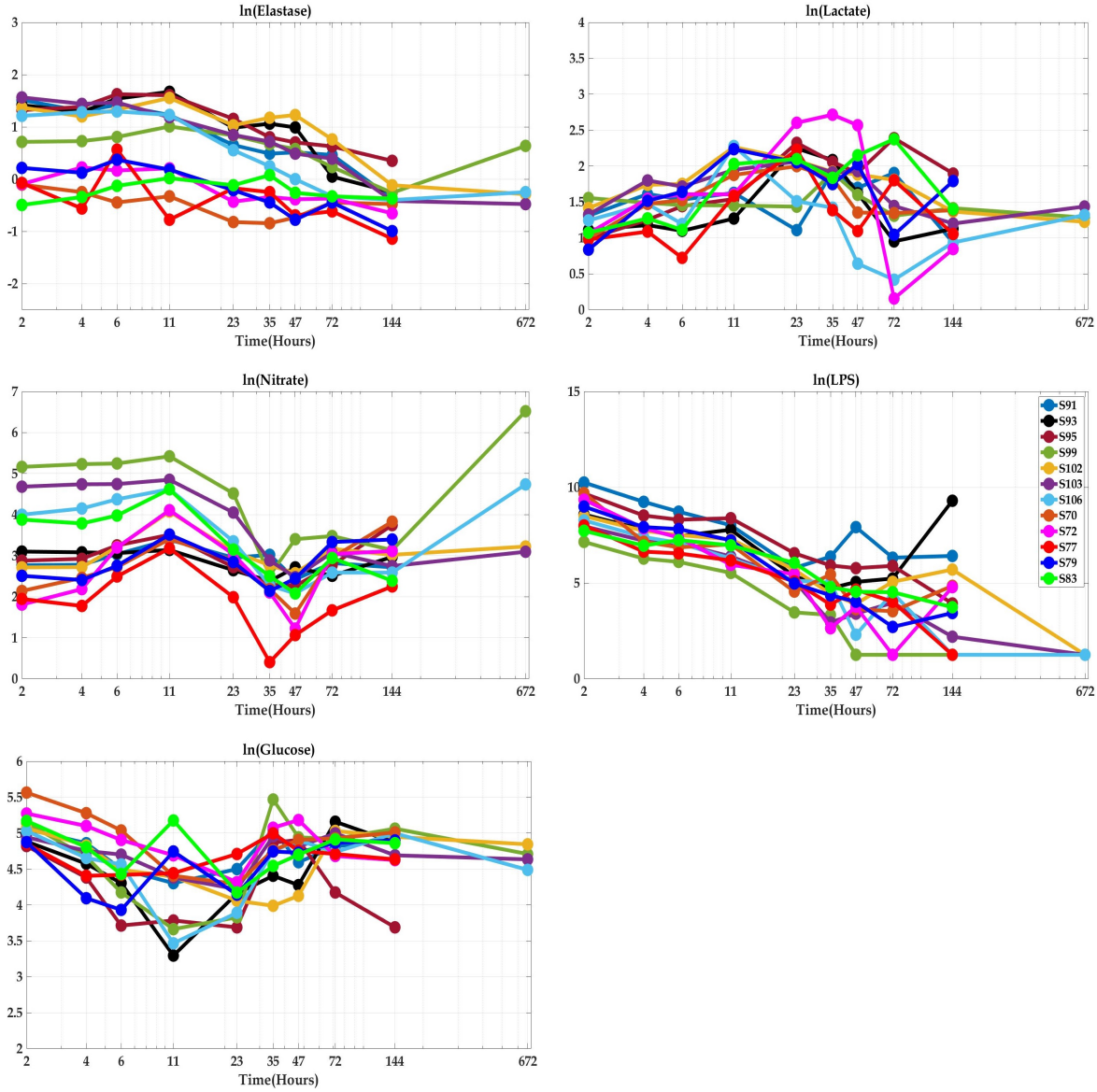

Figure 15: Time series trajectories of the observable variables for the survivors treated subjects. The x-axis is in logarithmic scale for better visualization. For this reason the time at $t = 0$ is not shown. The y-axis contains the logarithm of the observable variables.

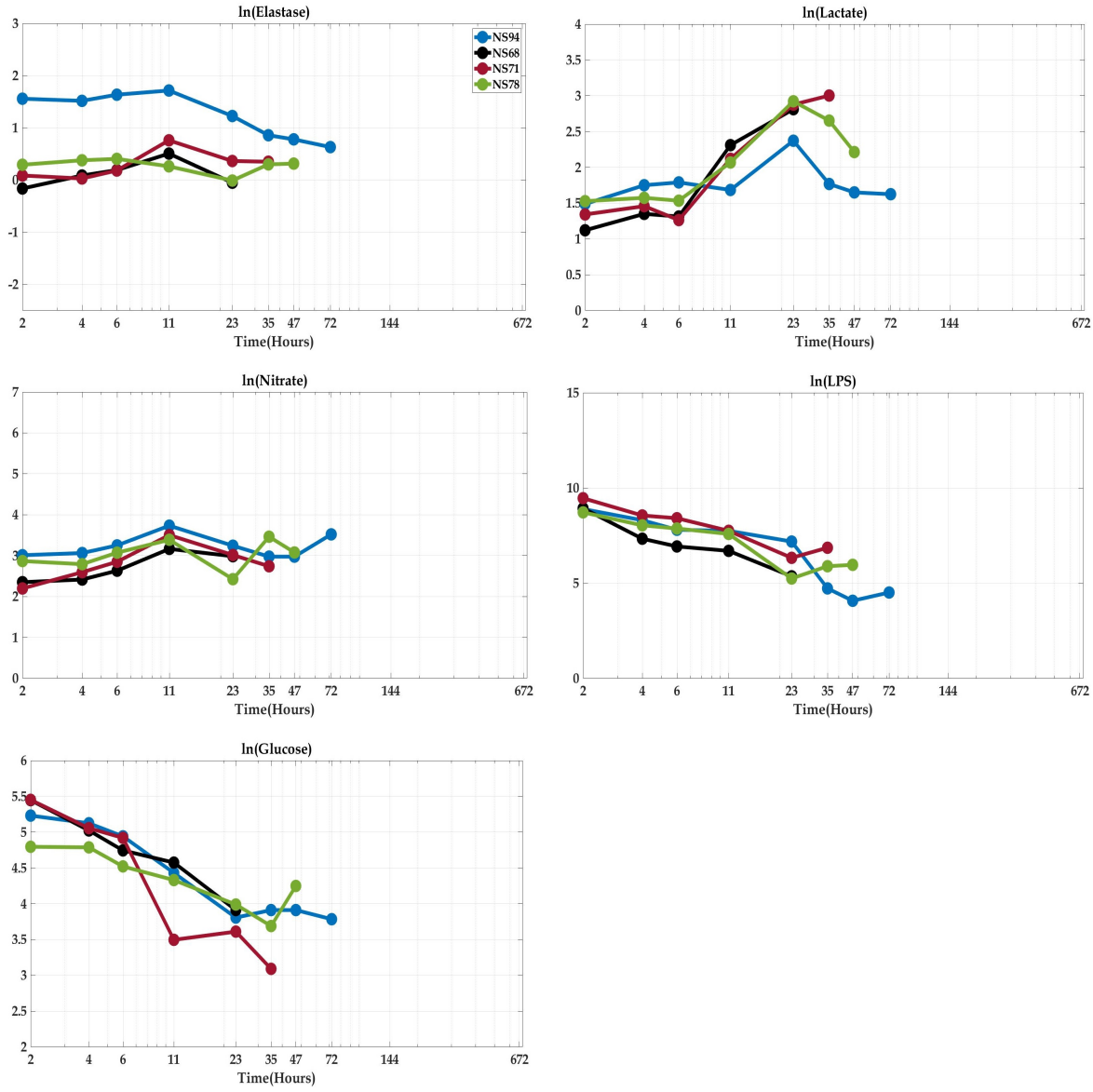

Figure 16: Time series trajectories of the observable variables for the non-survivors treated subjects. The x-axis is in logarithmic scale for better visualization. For this reason the time at $t = 0$ is not shown. The y-axis contains the logarithm of the observable variables.

3.3 Mathematical model

We present a data-driven model of the acute inflammatory response that also keeps track of the energy demand and production that is needed during activation of the acute immune response to fight an infection. This model extends our previous work [59] which is presented in this thesis in Section 2.2. This extended model consists of 14 ordinary differential equations which includes the interactions shown in Fig. 17. It includes variables that are normally measured in the ICU in septic patients, such as elastase, lactate, nitrate, lipopolysaccharides (LPS), and glucose. This model also includes pyruvate which brings more detail to the modeling of the cellular metabolism process and finally, this model also takes into account glycogen which corresponds to a storage form of glucose.

We recall, as mentioned in Section 2.2, that phagocytes including neutrophils, rely their production of ATP mostly on the anaerobic pathway, whereas the majority of other cells in the body produce their ATP with no special preference between aerobic or anaerobic metabolism. For this reason we split ATP into two pools, one that corresponds to the ATP produced by the phagocytes A_n, and other to the ATP produced by all the other cells in the body, A_b. Similarly, pyruvate was also separated into two distinct pools, Y_b and Y_n, corresponding to the pyruvate generated during the production of A_b and A_n, respectively. We once again use the notation A_x and Y_x, where x stands for the sub indices b and n.

Overall, the first eight equations (12)-(19), have the same structure than our previous model. However, some modifications were made in equations (13), (14), (16), (17), and (19), which we discuss next. The first change appears in equation (13) on which the production of activated phagocytes depends on LPS rather than on P. This change improves our first model in that the actual reason phagocytes become activated by the presence of pathogens is due to the release of LPS when their membrane is broken after elimination by immune cells. Another minor change occurs in equation (14), where we introduce the parameter α_x which works as a conversion unit between P and X.

More elaborated improvements appear in the description of the energy metabolism. Although the ATP equations keep the same structure as before, consisting of three parts: production, consumption, and natural depletion, a relevant change is observed in the pro-

duction of A_x. This production term consist itself of two parts. The first part contains the term $\beta(Y_{max}Y_x)/(Y_{max}+Y_x)$ with $\beta < 1$, which indicates the fraction of pyruvate that enters the mitocondria during the aerobic pathway, and it is down-regulated by nitric oxide through the term $f(X/X^*)$. The second term given by $\lambda_{an}c(A_x)G$, corresponds to the ATP produced via anaerobic respiration. The function $c(A_x)$ is a sigmoide which ramps up as A_x is consumed, leading to the need of metabolizing more glucose to fuel the energy demand.

Although phagocytes rely mostly their ATP production on anaerobic respiration, aerobic respiration still occurs but at lower levels. This is indicated by the ε_n parameter in front of the aerobic production term of A_n. The parameter λ_{an} is fixed equal to 100, and denotes the fact that anaerobic respiration is 100 times faster than aerobic respiration. From our previous discussion in Section 2.2, we know that about 30 molecules of ATP are produced per molecule of glucose during the aerobic pathway, whereas only 2 molecules of ATP are produced in the anaerobic pathway. More specifically, 1 molecule of glucose is transformed into 2 molecules of pyruvate which yields 30 molecules of ATP, which justifies the use of the constants 15 and 2 in front of each term of the production of A_x. The consumption of both ATPs is determined by the energy fluxes Φ_1, Φ_2, Φ_3, Φ_4, Φ_5, and Φ_6 which preserve the same structure and meaning as in the original model. Similarly, the ATP intrinsic decay did not change from the previous model and is equal to μ_A for both ATP's. It is important to mention that just as in the model presented in Chapter 2, $A_b = 1$ and $A_n = 1$ are baseline values by design.

The production of A_b and A_n depends on the parameters k_b and k_n whose role is to balance the units between molecules of glucose and molecules of pyruvate. These parameters are fixed but dependent on other parameters and initial conditions. We can find explicit expressions for k_b and k_n by solving equations (16), (17), (24), (25), (23), (22) around the healthy equilibrium. That is, when $\overline{P} = 0$, $\overline{N} = 0$, $\overline{D} = 0$, $\overline{A_b} = 1$, $\overline{A_n} = 1$, $\overline{X} = 0$, we find the values of $\overline{Y_b}, \overline{Y_n}, \overline{Gly}$, and $\overline{G}$ and substitute them in equations (16) and (17) to obtain equations (10) and (11). The bars over the variables indicate they are at the steady state value and the values for all the variables around the healthy steady state are given in Table 4.

$$k_b = \frac{\mu_A(Y_{max} + \overline{Y_b})}{s_g(Y_{max} + \overline{Y_b}) + 15\beta Y_{max}\overline{\overline{Y_b}}} \tag{10}$$

$$k_n = \frac{\mu_A(Y_{max} + \overline{Y_n})}{s_g(Y_{max} + \overline{Y_n}) + 15\beta\varepsilon_n Y_{max}\overline{Y_n}} \tag{11}$$

The first term of the Y_x equations describe the fact that 1 molecule of glucose yields 2 molecules of pyruvate, both being controlled by the corresponding decreasing sigmoidal function $c(A_x)$. The second and third terms on the Y_x equations, correspond to the amount of pyruvate that is converted during the aerobic pathway into A_x and to the intrinsic natural decay of Y_x, respectively. We assume both pyruvates decay at a rate of μ_Y.

The new variables Nit and LPS act as read outs of nitric oxide (X) and P, respectively. Nitrate is produced at a constant source rate s_{nit}. It is also produced as a byproduct of nitric oxide at a rate k_{no} and naturally depleted at a rate μ_{nit}. As a result of damaged tissue, bacteria make their way into the gut causing LPS leakage, which we assume happens at a rate s_{lps}. Moreover, LPS is found in the outer membrane of bacteria and it is released whenever pathogens are eliminated by phagocytes and nonspecific immune cells. This occurs at a rate k_{lps} and is included in the second term of equation (21). Finally, LPS is naturally depleted at a rate μ_{lps}.

Lactate is produced as a byproduct of anaerobic respiration and its production depends on how strong the X inhibition is on the aerobic pathway, causing pyruvate to enter into the fermentation process. The lactate equation is written in such a way that the higher the inhibition of nitric oxide on aerobic respiration, the more lactate is produced.

Finally, glycogen is a form of energy storage and when needed is converted back into glucose and vice versa. We include an additional equation describing this glucose-glycogen dynamics. We assume glucose is converted into glycogen at a rate k_{gly}, that glycogen is transformed into glucose again at a rate μ_{gly}, and we assume this transformation increases when inflammation occurs. Glucose is assumed to be constantly produced at a rate of s_g and when glucose is not converted into glycogen it is used as fuel to produced ATP.

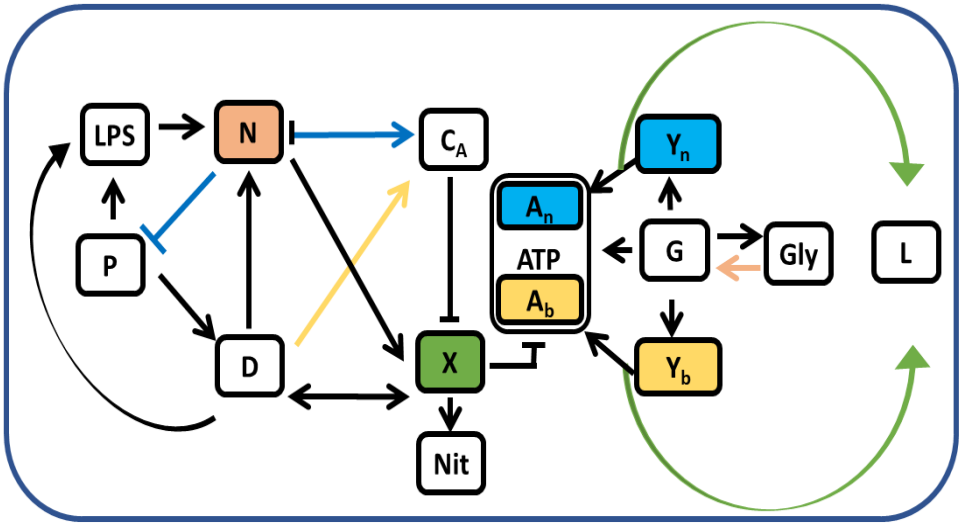

Figure 17: Interactions between the variables appearing in the system of equations (12)-(25). P denotes the level of pathogens, D corresponds to a marker of tissue damage, N represents the level of active phagocytes, C_A is anti-inflammatory mediators, X is nitric oxide, L lactate, and A_n and A_b correspond to the levels of ATP produced by phagocytes and all other cells in the body, respectively. Similarly, Y_n and Y_b, are the pyruvate levels for phagocytes and other cells in the body, respectively. LPS measures the amount of lipopolysaccharides , Nit is nitrogen, G glucose, and Gly corresponds to glycogen. Arrows and bars indicate up and down regulation, respectively. The effects on model components influenced by levels of A_n are indicated by blue arrows and bars while the effects dependent on A_b are denoted in yellow. Similarly, the nitric oxide effect on lactate production is colored in green. And the implicit action of phagocyte inflammation over the transformation of glycogen into glucose is colored in pink.

$$\frac{dP}{dt} = k_{pg}P\left(1-\frac{P}{P_\infty}\right) - (1+k_{ns}g(A_b))\frac{k_{pm}P}{\mu_m + k_{mp}P} - \frac{k_{pn}g(A_n)f\left(\frac{C_A}{C^*}\right)NP}{1+k_{ps}P} \tag{12}$$

$$\frac{dN}{dt} = \frac{s_{nr}g(A_n)f\left(\frac{C_A}{C^*}\right)(k_{nn}N + k_{np}LPS + k_{nd}D)}{\mu_{nr} + f\left(\frac{C_A}{C^*}\right)(k_{nn}N + k_{np}LPS + k_{nd}D)} - \mu_n\left(1 + \frac{k_{de}g(A_n)f\left(\frac{C_A}{C^*}\right)P}{1+k_{ps}P}\right)N \tag{13}$$

$$\frac{dD}{dt} = k_{dn}h(\alpha_x X + P) - g(A_b)\mu_d D \tag{14}$$

$$\frac{dC_A}{dt} = s_c + k_{cn}\left(\frac{g(A_n)f\left(\frac{C_A}{C^*}\right)N}{\mu_{cq} + f\left(\frac{C_A}{C^*}\right)N} + \frac{g(A_b)f\left(\frac{C_A}{C^*}\right)k_{cnd}D}{\mu_{cq} + f\left(\frac{C_A}{C^*}\right)k_{cnd}D}\right) - \mu_c C_A \tag{15}$$

$$\frac{dA_b}{dt} = k_b\left(15\beta f\left(\frac{X}{X^*}\right)\frac{Y_{max}Y_b}{Y_{max}+Y_b} + 2\lambda_{an}c(A_b)G\right) - g(A_b)\sum_{i\in\{1,4,6\}}\Phi_i - \mu_A A_b \tag{16}$$

$$\frac{dA_n}{dt} = k_n\left(\varepsilon_n 15\beta f\left(\frac{X}{X^*}\right)\frac{Y_{max}Y_n}{Y_{max}+Y_n} + 2\lambda_{an}c(A_n)G\right) - g(A_n)\sum_{i\in\{2,3,5\}}\Phi_i - \mu_A A_n \tag{17}$$

$$\frac{dX}{dt} = f\left(\frac{C_A}{C^*}\right)(k_{non}N + k_{nod}D) - \mu_{no}X \tag{18}$$

$$\frac{dL}{dt} = \lambda_L\left(1 - \beta f\left(\frac{X}{X^*}\right)\right)(Y_n + Y_b) - \mu_L L \tag{19}$$

$$\frac{dNit}{dt} = s_{nit} + k_{no}X - \mu_{nit}Nit \tag{20}$$

$$\frac{dLPS}{dt} = s_{lps}D + k_{lps}\left((1+k_{ns}g(A_b))\frac{k_{pm}P}{\mu_m + k_{mp}P} - \frac{k_{pn}g(A_n)f\left(\frac{C_A}{C^*}\right)NP}{1+k_{ps}P}\right) - \mu_{lps}LPS \tag{21}$$

$$\frac{dG}{dt} = s_g + \mu_{gly}(1+N)Gly - \lambda_{an}\left(c(A_b) + c(A_n)\right)G - k_{gly}G \tag{22}$$

$$\frac{dGly}{dt} = k_{gly}G - \mu_{gly}(1+N)Gly \tag{23}$$

$$\frac{dY_b}{dt} = 2\lambda_{an}c(A_b)G - f\left(\frac{X}{X^*}\right)\frac{Y_{max}Y_b}{Y_{max}+Y_b} - \mu_Y Y_b \tag{24}$$

$$\frac{dY_n}{dt} = 2\lambda_{an}c(A_n)G - \varepsilon_n f\left(\frac{X}{X^*}\right)\frac{Y_{max}Y_n}{Y_{max}+Y_n} - \mu_Y Y_n \tag{25}$$

where

$$f(V) = \frac{1}{1+V^2}\ ; \quad h(V) = \frac{V^6}{x_{dn}^6 + V^6}\ ; \quad c(A_x) = \frac{k_A(1+k_2)}{k_2 + e^{k_1(A_x-1)}}\ ; \quad g(A_x) = \frac{A_x^2}{c_g + A_x^2}\ ;$$

and

$$\Phi_1 = c_1 \frac{k_{pm} s_m k_{ns} P}{\mu_m + k_{mp} P} \; ; \quad \Phi_2 = c_2 \frac{k_{pn} f\left(\frac{C_A}{C^*}\right) NP}{1 + k_{ps} P} \; ;$$

$$\Phi_3 = c_3 \frac{s_{nr} f\left(\frac{C_A}{C^*}\right) (k_{nn} N + k_{np} LPS + k_{nd} D)}{\mu_{nr} + f\left(\frac{C_A}{C^*}\right) (k_{nn} N + k_{np} LPS + k_{nd} D)};$$

$$\Phi_4 = c_4 \mu_d D; \quad \Phi_5 = c_5 \frac{k_{cn} f\left(\frac{C_A}{C^*}\right) N}{\mu_{cq} + f\left(\frac{C_A}{C^*}\right) N} \; ; \quad \Phi_6 = c_6 \frac{k_{cn} f\left(\frac{C_A}{C^*}\right) k_{cnd} D}{\mu_{cq} + f\left(\frac{C_A}{C^*}\right) k_{cnd} D};$$

Table 4: Healthy equilibrium state values for equations (12)-(25)

Variable	Equilibrium Value	Variable	Equilibrium Value
$\overline{P}$	0	$\overline{L}$	$\frac{(1-\beta)(\overline{Y_b}+\overline{Y_n})\lambda_L}{\mu_L}$
$\overline{N}$	0	$\overline{Nit}$	$\frac{s_{nit}}{\mu_{nit}}$
$\overline{D}$	0	$\overline{LPS}$	0
$\overline{C_A}$	$\frac{s_c}{\mu_c}$	$\overline{G}$	$\frac{s_g}{2\lambda_{an} k_A}$
$\overline{A_b}$	1	$\overline{Gly}$	$\frac{k_{gly}}{\mu_{gly}} \overline{G}$
$\overline{A_n}$	1	$\overline{Y_b}$	positive solution to $Ax^2 + Bx + C = 0$ where $A = -\mu_y$ $B = 2\lambda_{an} k_A \overline{G} - Y_{max} - \mu_Y Y_{max}$ $C = 2\lambda_{an} k_A \overline{G} Y_{max}$
$\overline{X}$	0	$\overline{Y_n}$	positive solution to $Dx^2 + Ex + F = 0$ where $D = -\mu_y$ $E = 2\lambda_{an} k_A \overline{G} - \varepsilon_n Y_{max} - \mu_Y Y_{max}$ $F = 2\lambda_{an} k_A \overline{G} Y_{max}$

3.4 Results

Similar to the original model, the extended model also presents three biologically relevant equilibrium points, healthy, aseptic, and septic. Sample trajectories of these states are shown in Figures 18, 19, and 20. We present these trajectories in logarithmic time scale for better visualization. These three trajectories were obtained with the same set of parameters and initial conditions shown in Table 5, and only varying the pathogen growth rate k_{pg}.

In the healthy state trajectory (Fig. 18), pathogens P enter the host and trigger an immune response led by activated phagocytes. This response quickly resolves the infection within the first 10 to 15 hours. During this time, anti-inflammatory mediators play a fundamental role in down-regulating inflammation at expenses of energy. There is a rise in tissue damage that leads to accumulation of nitric oxide, lactate, nitrate, and LPS. However, a proper balance of glucose provides enough ATP to sustain C_A production as well as to maintain an adequate tissue healing. Just before pathogens are eliminated, phagocytes take a second rebound. However, a proper down-regulation from the anti-inflammatory mediators, controls such rebound and allows the trajectories to land back in the healthy state.

The aseptic trajectory (Fig. 19) shows a similar behavior for the beginning of the simulation. However, this time pathogens replicate at a higher rate, and therefore need a much faster immune response that quickly is out of control and the C_A can not sustain for too long. This uncontrolled inflammation leads to a rapid increase in nitric oxide, tissue damage, nitrate and lactate. Finally, energy is consumed in an attempt to fight the over inflammatory response, leading to a drop in the glucose and glycogen levels.

In the septic trajectory (Fig. 20), the pathogen rate is so fast that the immune response is unable to mitigate their reproduction. At about 20 hours the immune system cannot hold the infection anymore and pathogens start to take over the host. As an attempt to fight this rapid infection, energy reserves are consumed and are not enough to neither fuel anti-inflammatory mediators nor provide an adequate tissue healing response. This leads to elevated values of nitric oxide, which trigger higher tissue damage and LPS.

Unlike the previous model presented in Chapter 2, ATP can now attain values higher than 1. This happens when there is a glucose uptake or high energy response. However, the

ATP healthy steady state value is still 1.

3.5 Discussion

We developed and extended model that includes the dynamics of the acute immune response along with the energy requirements that are needed when fighting an infection. This model builds on the previous work done in [59] and presented in Chapter 2 of this thesis. A data-oriented approach was followed in the development of the model, on which we included and modified new equations to describe the observed animal data. We provide a thorough description of the model equations and parameters and illustrate the transient dynamics of three biologically significant equilibrium points: healthy, aseptic, and septic.

In equations (10) and (11), we showed that the parameters k_b and k_n are fixed but dependent on other model parameters. In particular, these two parameters are μ_A-dependent. Therefore, using the notation $k_b = \hat{k}_b \mu_A$ and $k_n = \mu_A \hat{k}_n$, where

$$\hat{k}_b = \frac{(Y_{max} + \overline{Y_b})}{s_g(Y_{max} + \overline{Y_b}) + 15\beta Y_{max}\overline{Y_b}} \tag{26}$$

$$\hat{k}_n = \frac{(Y_{max} + \overline{Y_n})}{s_g(Y_{max} + \overline{Y_n}) + 15\beta\varepsilon_n Y_{max}\overline{Y_n}} \tag{27}$$

equations (16) and (17) can be rewritten as:

$$\frac{dA_b}{dt} = \mu_A \left[\hat{k}_b \left(15\beta f \left(\tfrac{X}{X^*}\right) \tfrac{Y_{max}Y_b}{Y_{max}+Y_b} + 2\lambda_{an} c(A_b) G\right) - A_b\right] - g(A_b) \sum_{i\in\{1,4,6\}} \Phi_i \tag{28}$$

$$\frac{dA_n}{dt} = \mu_A \left[\hat{k}_n \left(\varepsilon_n 15\beta f \left(\tfrac{X}{X^*}\right) \tfrac{Y_{max}Y_n}{Y_{max}+Y_n} + 2\lambda_{an} c(A_n) G\right) - A_n\right] - g(A_n) \sum_{i\in\{2,3,5\}} \Phi_i \tag{29}$$

Unlike in the reduced model presented in Chapter 2, μ_A is involved not only in the depletion rate of ATP but also in its own production rate. This suggests that parameter μ_A can be understood as the energy rate constant. This equivalent way of writing the ATP equations will be convenient later on in Chapter 5 when we discuss the role of important parameters to predict patient outcome.

The new extended model improves our previous model in that it includes the dynamics of commonly measured variables in the ICU and therefore can eventually be calibrated with human data. However, with a more realistic model comes the downside of having more unknown parameters and complicated non-linearities that can potentially make parameter estimation challenging. When fitting a complex non-linear dynamical system with human data, issues like unidentifiable parameters and computational limitations can present barriers to extract useful information from this models.

Nitric oxide has also been found to have protective roles in response to inflammatory estimuli, including preservation of blood flow and prevention of platelet adhesion [53]. Future extensions of this model include incorporating such protective roles of nitric oxide. This model can also be used to form compartmental models for the study of multiple organ dysfunction syndrome (MODS) by including the dynamics of certain organs like the liver and lungs. Model and parameter dimensionality reduction are also part of possible future directions.

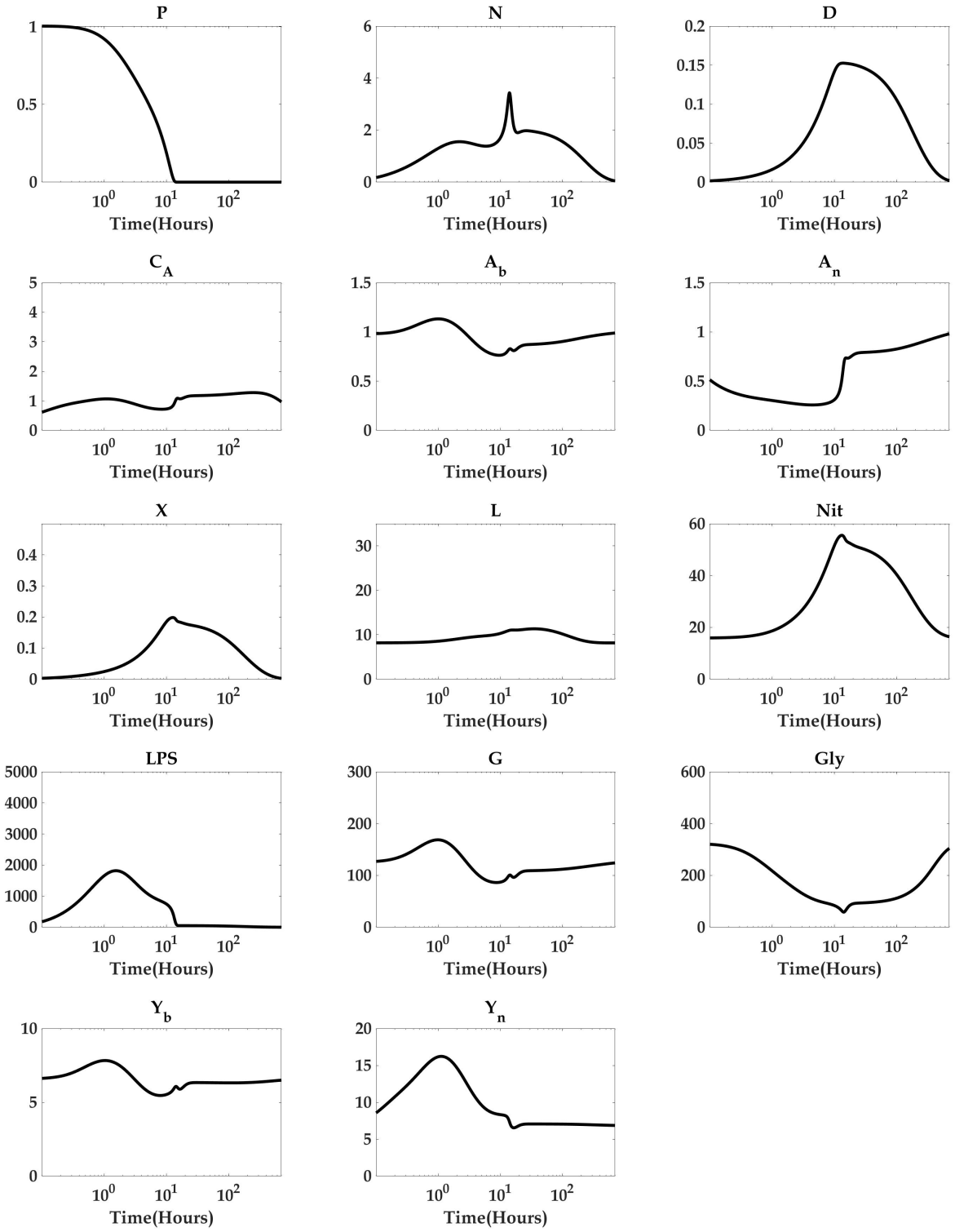

Figure 18: Sample model trajectories for the healthy state. Parameter values are given in Table 5. Initial conditions are computed as in Table 4, with the exception of initial pathogen load which is $P(0) = 1$.

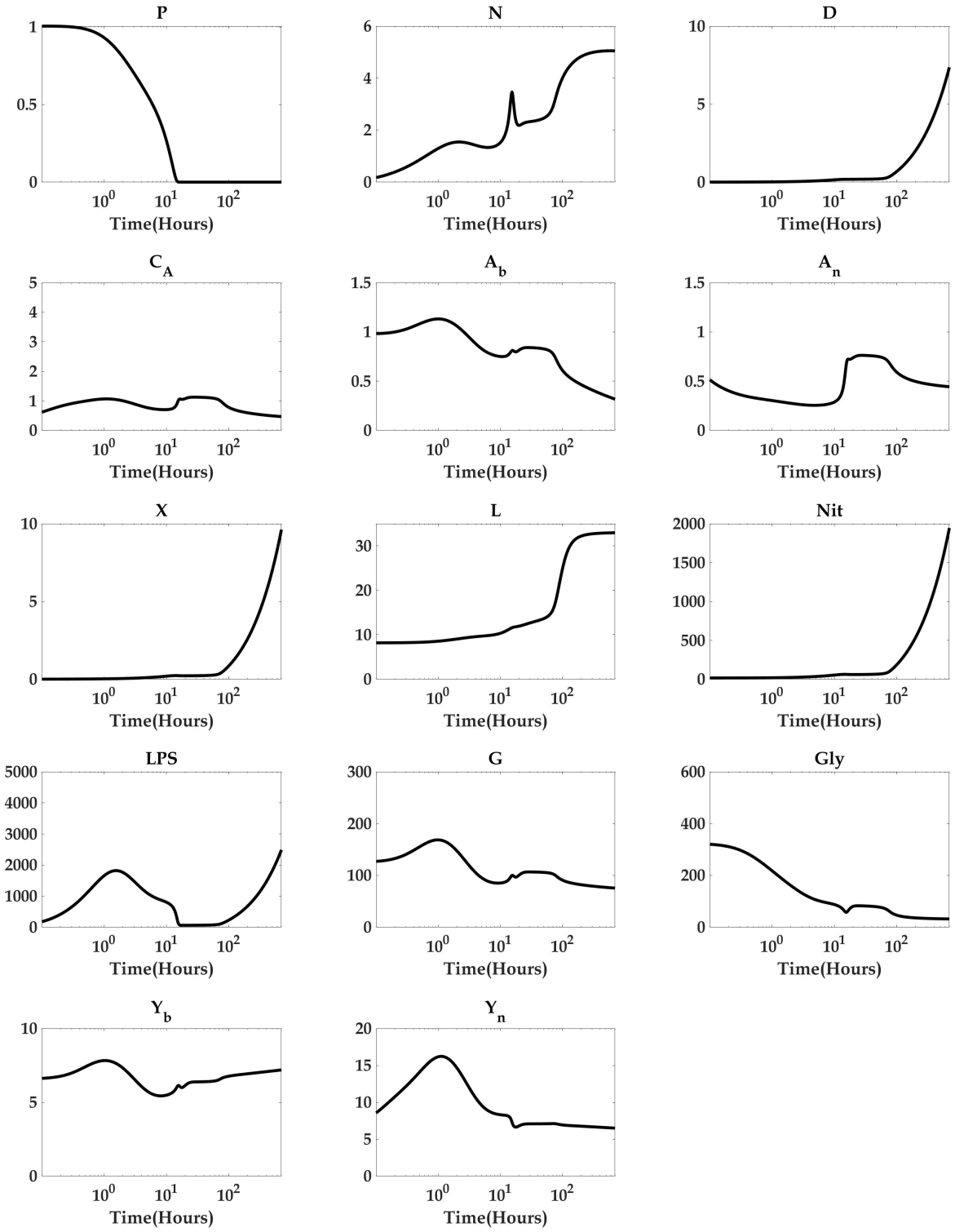

Figure 19: Sample model trajectories for the aseptic state. All parameter values are given in Table 5 with the exception of $k_{pg} = 0.13907$. Initial conditions are computed as in Table 4, with the exception of initial pathogen load which is $P(0) = 1$.

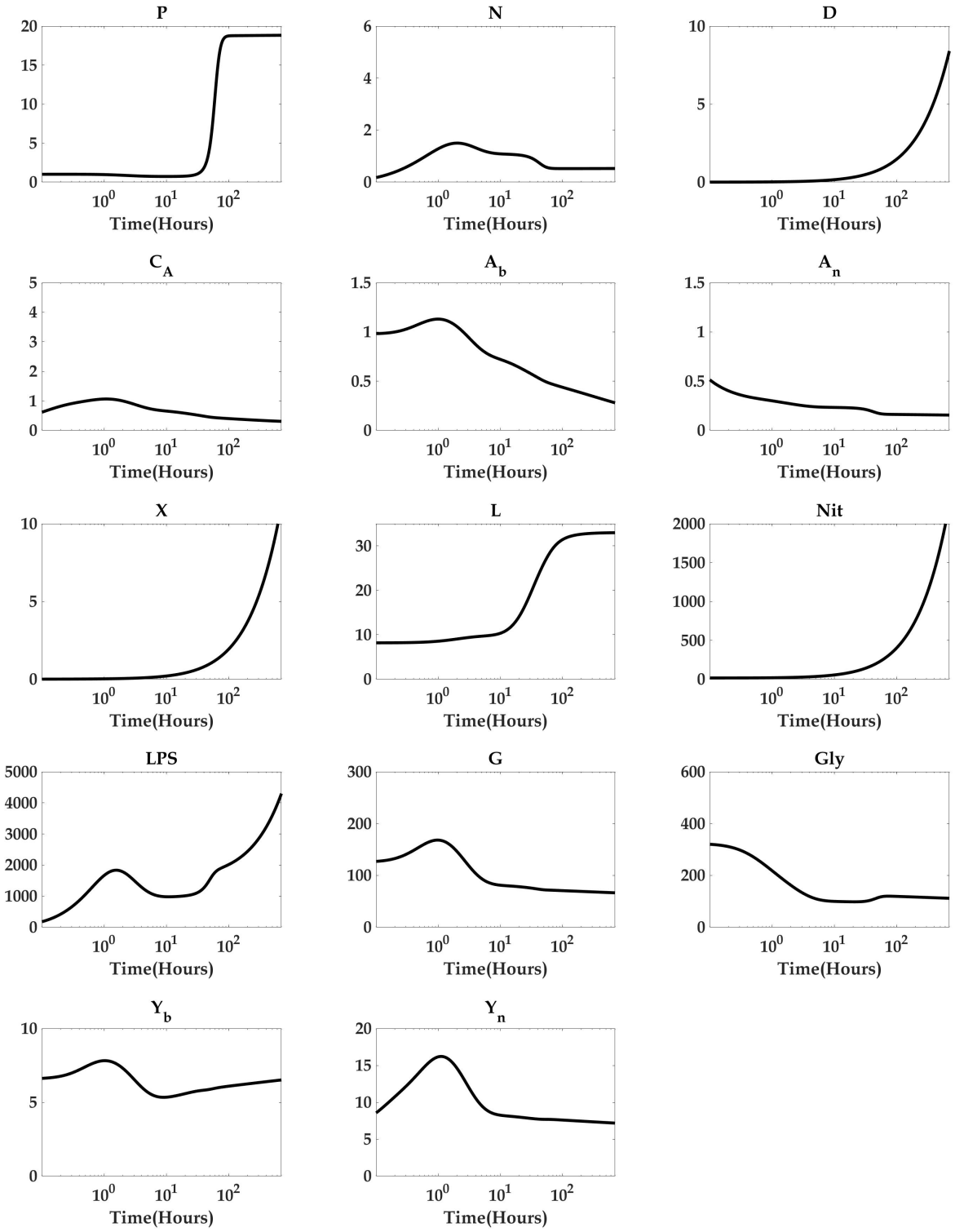

Figure 20: Sample model trajectories for the septic state. All parameter values are given in Table 5 with the exception of $k_{pg} = 0.17615$. Initial conditions are computed as in Table 4, with the exception of initial pathogen load which is $P(0) = 1$.

Table 5: Parameter values for the health sample trajectory

Parameter	Value	Description
k_{pg}	0.1298	Pathogen growth rate
P_∞	20×10^6/cc	Carrying capacity for pathogen
k_{pm}	0.000148	Rate parameter for the elimination of pathogens by the non-specific local response
k_{ns}	0.59934	Weighting of the energy-dependent component of non-specific pathogen elimination
μ_m	0.0044093/h	Half-activation parameter for the non-specific local response
k_{mp}	0.0001478	Saturation rate parameter for the non-specific local response
k_{pn}	9.1058	Phagocytosis rate
C^*	2.5114	Saturation parameter for effects of anti-inflammatory mediators
k_{ps}	0.34996	Phagocytosis saturation constant
s_{nr}	82.137	Production rate for activated phagocytes
k_{nn}	0.00088	Weight of contribution to activation of resting phagocytes by previously activated phagocytes and their cytokines
k_{np}	0.014887	Weight of contribution to activation of resting phagocytes by LPS
k_{nd}	0.00068064	Weight of contribution to activation of resting phagocytes by tissue damage
μ_{nr}	4.2731/h	Decay rate of resting phagocytes
μ_n	0.94573/h	Decay rate of activated phagocytes
k_{de}	15.119	Pathogen degradation enhancement constant
k_{dn}	0.016343	Maximum rate of damage produced by activated phagocytes
α_x	1.2639	Weight of contribution of creation of tissue damage by nitric oxide
x_{dn}	0.41101	Determines levels of pathogens and nitric oxide needed to bring damage production up to half its maximum
μ_d	0.026832/h	Rate of tissue healing
s_c	2.1859	Source of anti-inflammatory mediators
k_{cn}	24.893	Maximum production rate of anti-inflammatory mediators
k_{cnd}	907.29	Effectiveness of damaged tissue relative to activated phagocytes in inducing production of anti-inflammatory mediators
μ_{cq}	0.13048	Determines the levels of activated phagocytes and damage that are needed to bring rate of anti-inflammatory mediator production to half its maximum
μ_c	9.9179/h	Decay rate of anti-inflammatory mediators
μ_A	24.743	Energy rate constant
c_g	2.8237	Half-saturation energy level for the driving of various processes
k_b	0.14951	Scaling parameter to balance units of glucose and pyruvate in the A_b production process

Table 6: Parameter values for the health sample trajectory continued

Parameter	Value	Description
β	0.74611	Fraction of pyruvate that is converted into ATP during aerobic respiration
X^*	0.43276	Half saturation level of NO
Y_{max}	22.326	Maximum saturation value for pyruvate
λ_{an}	fixed at 100	ATP production during anaerobic glycolysis is about 100 times faster than during phosphorylation
k_A	0.0043282	Homeostatic value of modulator function $c(A_x)$, i.e when $A_x = 1$
k_1	0.91496	Phenomenological energy production parameter
k_2	0.083895	Phenomenological energy production parameter
c_1	169.98	Energy consumption rate of Φ_1
c_2	206.03	Energy consumption rate of Φ_2
c_3	2.5215	Energy consumption rate of Φ_3
c_4	1366.2	Energy consumption rate of Φ_4
c_5	0.29397	Energy consumption rate of Φ_5
c_6	0.023474	Energy consumption rate of Φ_6
k_n	0.22686	Scaling parameter to balance units of glucose and pyruvate in the A_n production process
ε_n	0.0018957	Denotes lower production of A_n through the anaerobic pathway
k_{non}	99.788	Rate of NO release due to presence of pro-inflammatory cytokines
k_{nod}	24504	Rate of NO release due to tissue damage
μ_{no}	18174	Natural depletion rate of NO
λ_L	0.2081	Production rate of lactate
μ_L	0.086296	Decay rate of lactate
s_{nit}	28.159	Source of nitrate
k_{no}	355.66	Rate at which NO is converted into nitrate
μ_{nit}	1.7728	Decay rate of nitrate
s_{lps}	1046.1	Source of LPS
k_{lps}	23206	Rate at which LPS is released after pathogen membrane breaking by immune cells
μ_{lps}	3.0929	Decay rate of LPS
s_g	108.96	Source of glucose
μ_{gly}	1.2347	Rate at which glycogen is converted into glucose
k_{gly}	3.1658	Rate at which glucose is converted into glycogen
μ_Y	15.915	Decay rate of pyruvate

4.0 Parameter estimation on data-driven model

4.1 Introduction

Once a mathematical model provides qualitative features that are consistent to the known biology of the problem of interest, we proceed to a second stage known as parameter estimation. There are some standard techniques that are commonly used when modeling complex biological processes. In this chapter we begin by utilizing the so called ordinary least squares method to obtain a nominal set of parameters that better explains our data. We present a brief introduction to the method and then present the results and conclusions. We then present an introduction to Bayesian parameter estimation and use it to quantify uncertainty on the model parameters. More specifically, we use an delayed rejection adaptive metropolis algorithm and available data to construct a distribution of parameters that resembles patient heterogeneity. The main goal in this chapter is to find distributions for model parameters that can be used to predict patient outcome with certain probability.

4.2 Ordinary least squares (OLS)

The standard ordinary least squares (OLS) formulation involves a mathematical model and a statistical model [4] [11]. The mathematical model can be written as:

$$\frac{dx}{dt} = g(t, x(t, \theta), \theta) \tag{30}$$

where $x(t, \theta) \in \mathbb{R}^m$ corresponds to the parameter state variable vector at time t and $\theta \in \mathbb{R}^p$ denotes the parameter vector and p the number of parameters.

We denote the model output by $f(t_i, \theta_0)$ which is a functional of the state variable $x(t, \theta)$. That is $f(t_i, \theta_0) \in \mathscr{F}(x(t, \theta))$ and θ_0 is the true parameter vector. In our case, the statistical model for the observation process will be given by

$$\ln(Y_i) = \ln\left(f(t_i, \theta_0)\right) + \mathscr{E}_i \tag{31}$$

where Y_i is a vector of random variables with realizations y_i. We assume the errors $\mathscr{E}_i$ are independent and identically log-normally distributed random variables, that is $\text{cov}\,(\mathscr{E}_i, \mathscr{E}_j) = 0$ whenever $i \neq j$. We assume different observation coordinates f_i may have different variances σ_i^2 associated with different coordinates of the errors $\mathscr{E}_i$. Then $\mathscr{E}_i$ is an m-dimensional random vector, [4]. We also assume $E[\mathscr{E}_i] = 0$, and that $\text{var}(\mathscr{E}_i) = V_0 = \text{diag}(\sigma_{0,1}^2, \cdots, \sigma_{0,m}^2)$.

Typically the method of ordinary least squares consists in minimizing the objective function consisting on the sum of square differences between data and the model. The objective function can however be modified to normalize residuals and also include heuristic terms to constraint the parameter domain. We will use a weighted ordinary least squares with heuristics $\mathcal{H}$:

$$\sum_{i=1}^{n} w_i \left[\ln(Y_i) - \ln\left(f(t_i, \theta)\right)\right]^2 + \mathcal{H} \tag{32}$$

where the minimum is taken over the set of parameter vectors θ constrained by a pre-specified feasible region denoted Θ. The minimizer is a random variable, called the estimator θ_{OLS} and is given by

$$\theta_{OLS} = \text{argmin}_{\theta \in \Theta} \sum_{i=1}^{n} w_i \left[\ln(Y_i) - \ln\left(f(t_i, \theta)\right)\right]^2 + \mathcal{H} \tag{33}$$

The theoretical quantity θ_0 is in general unknown. In practice, one has only the data associated with a single realization y_i of the observation process Y_i for $i = 1, 2, \cdots, n$ and has no option but to compute an estimate for θ_{OLS} denoted $\hat{\theta}_{OLS}$ and given by

$$\hat{\theta}_{OLS} = \text{argmin}_{\theta \in \Theta} \sum_{i=1}^{n} w_i \left[\ln(y_i) - \ln\left(f(t_i, \theta)\right)\right]^2 + \mathcal{H} \tag{34}$$

In our case, in order to use fit the model with the data, we first define

$$Elas(t_i, \theta) = N(t_i, \theta) + elas_b \tag{35}$$

where $elas_b$ is a shifting parameter that scales the N trajectory to fit the elastase data. Parameter $elas_b$ will from now on be part of the unknown parameter set. Therefore, from now on and for the rest of this chapter, for fitting purposes we will use equation (35) instead of equation (13). Further, we define

$$f(t_i, \theta) = \left[Elas(t_i, \theta), L(t_i, \theta), Nit(t_i, \theta), LPS(t_i, \theta), G(t_i, \theta)\right]^T \tag{36}$$

and then $\ln(f(t_i,\theta))$ in equation (34) indicates taking the logarithm entrywise.

As all subjects in the experiment were given the same amount of initial bacterial load, we assume all survivors will have similar response against the infection. Therefore, we use the OLS method described here to estimate a nominal set of parameters for the average data trajectory obtained with the non-treated survivors S89, S90, S100, and S101.

In order to use the formulation of the OLS described above, we define an appropriate objective function that includes the fact that measurements are in logarithmic scale, that it normalizes the distance between data and the model, and that ensures we obtain a set of parameters whose outcome is a survivor trajectory, by including heuristic terms. Therefore, we are interested in finding

$$\hat{\theta}_{OLS} = \text{argmin}_{\theta\in\Theta} G(t,\theta) \tag{37}$$

where $G(t,\theta)$ is defined as follows:

$$\begin{aligned} G(t,\theta) = &\sum_{i=1}^{10}\left[\frac{\ln(LPS_{data}(t_i)) - \ln(LPS_{model}(t_i,\theta))}{\ln(LPS_{SD}(t_i))}\right]^2 + \omega_1 H(LPS_{model}(t_0) - 3.5) + \\ &\omega_2 H(LPS_{model}(t_{11}) - 3.5) + \sum_{i=1}^{10}\left[\frac{\ln(Elas_{data}(t_i)) - \ln(Elas_{model}(t_i,\theta))}{\ln(Elas_{SD}(t_i))}\right]^2 + \\ &\omega_3 H(Elas_{model}(t_{11}) - 0.11) + \sum_{i=1}^{11}\left[\frac{\ln(L_{data}(t_i)) - \ln(L_{model}(t_i,\theta))}{\ln(L_{SD}(t_i))}\right]^2 + \\ &\sum_{i=1}^{11}\left[\frac{\ln(Nit_{data}(t_i)) - \ln(Nit_{model}(t_i,\theta))}{\ln(Nit_{SD}(t_i))}\right]^2 + \omega_4 H(D_{model}(t_{11}) - 0.0001) + \\ &\sum_{\substack{i=1\\ i\neq 7,8,9}}^{11}\left[\frac{\ln(G_{data}(t_i)) - \ln(G_{model}(t_i,\theta))}{\ln(G_{SD}(t_i))}\right]^2 + \omega_5 H(P_{model}(t_{11}) - 0.0001) + \\ &\omega_6 H(max(C_A) - 2C^*) \end{aligned} \tag{38}$$

Here, $\theta = (\theta_1, \cdots, \theta_M)$ is the vector of unknown model parameters to be determined and the data points are collected at times $t = t_1, \cdots, t_{11}$, as described in Section 3.2. This function consists of the normalized difference squared between the natural logarithm of the observed data and the natural logarithm of the model. In particular, we use weighted Heaviside functions as heuristics to impose certain conditions we want our output trajectory

to satisfy. We note that in the data, at the first and last time points, t_0 and t_{11}, LPS was recorded to be exactly 3.5 across all individuals in the placebo group. This suggests that 3.5 corresponds to the lowest level of detection observed in LPS instead of being the actual recorded value. We introduce the terms $\omega_1 H(LPS_{model}(t_0) - 3.5)$ and $\omega_2 H(LPS_{model}(t_{11}) - 3.5)$. In these terms, $H(x-a)$ is the Heaviside function that equals 0 when $x < a$ and equals 1 when $x - a > 0$. Overall, the idea is to force the algorithm to search for parameter values that satisfy that $LPS_{model}(t_j) < 3.5$ for $j = 0, 11$.

Similarly, in order to obtain an elastase trajectory that also goes below the level of detection of 0.11 at time t_{11}, we impose the condition $\omega_3 H(Elas_{model}(t_{11}) - 0.11)$. Moreover, the terms $\omega_4 H(D_{model}(t_{11}) - 0.0001)$ and $\omega_5 H(P_{model}(t_{11}) - 0.0001)$ force the algorithm to search in the parameter space for values for which $D_{model}(t_{11})$ and $P_{model}(t_{11})$ lie below 0.0001, which we use as threshold to define a healthy trajectory. The term $\omega_6 H(max(C_A) - 2C^*)$, guarantees the maximum value achieved by the model variable C_A does not passes 2 times its half saturation given by C^*. The parameters ω_i are penalty weights, and depending on how much weight one wants to put on each penalty condition, ω_i can be modified. However, we used $\omega_i = 100$ for all $i = 1, \cdots, 6$, as we wanted to have equal weight.

It is important to note that every term in the sum of squares is weighted by a term of the form $\log(V_{SD}(t_i))$ where $V_{SD}(t_i)$ corresponds to the standard deviation of the measurement V at time t_i. Also, because subjects were fed during times t_7, t_8, and t_9, we observed a glucose increment that is not part of the inflammatory response we are interested on. Therefore, we will not be considering these time points in glucose trajectory for data fitting.

We used the patternsearch algorithm from Matlab R2018b to minimize the objective function $G(t, \theta)$ and to speed up the process of solving the system of differential equations and calculate Y_{model}, we used CVODE as provided in SUNDIALS, [40]. The values of the parameters obtained in the OLS are given in Table 7. All but six parameters were left free. We assume pathogen load has a maximum carrying capacity of $P_\infty = 20 \times 10^6/cc$, $\lambda_{an} = 100$ corresponds to the speed at which anaerobic respiration occurs (100 times faster than aerobic respiration). We estimated $C^* = 2$, and the maximum production rate of anti-inflammatory mediators at $k_{cn} = 49.483$. Lastly, k_b and k_n are fixed but depend on other parameters. They can be computed as shown in equations (10) and (11).

The resulting best fit trajectory is depicted in Fig. 21 in logarithmic scale whereas Fig. 22 shows the same plot in linear scale up to 150 hours. Similarly, the corresponding model trajectories in logarithmic scale are shown in Fig. 23 and in linear scale for the first 50 hours in Fig. 24. We observe that within the first hour, the presence of pathogens activate an inflammatory response which is responsible for the rise in nitric oxide and consequently in tissue damage and lactate. As pathogens are eliminated by neutrophils and other immune cells, LPS builds up contributing also to the increase in tissue damage. In an attempt to control the inflammatory response, anti-inflammatory mediators C_A also kick in during the first hour after infection. In the urge of a quick response for the ATP demand to fuel both the inflammatory and anti-inflammatory cascade, glycogen is quickly transformed into glucose. During the next few hours pathogens are gradually eliminated until at about $t = 10$ hours they are no longer in the system. Because no more pathogens are around and an adequate amount of anti-inflammatory mediators, N starts decreasing and inflammation seems to be under control. However, because at 10 hours C_A is lowering down and tissue damage is still building up, due to the still high values of nitric oxide and LPS, neutrophils have a rebound. Such rebound activates again the C_A production fueled by ATP in an effort to control inflammation and tissue healing. After the first 10 hours, tissue starts to recover from damage, LPS continues decreasing and C_A finally down-regulates inflammation until N decays to rest on the healthy equilibrium at the end of the simulation.

Table 7: Best fit parameter values and initial conditions for average of the survivors

Parameter	Value	Parameter	Value	Parameter	Value
k_{pg}	0.12388	s_c	1.4416	c_6	0.01396
P_∞	fixed at 20	k_{cn}	fixed at 49.483	k_n	fixed at 0.173
k_{pm}	0.0002	k_{cnd}	767.46	ε_n	0.00183
k_{ns}	0.37134	μ_{cq}	0.071231	k_{non}	91.07
μ_m	0.00298	μ_c	5.8034	k_{nod}	14162
k_{mp}	0.00075	μ_A	14.638	μ_{no}	10739
k_{pn}	7.1696	c_g	1.8958	λ_L	0.16851
C^*	fixed at 2	k_b	fixed at 0.1025	μ_L	0.0711
k_{ps}	0.29301	β	0.91389	s_{nit}	26.363
s_{nr}	53.567	X^*	0.24701	k_{no}	317.8
k_{nn}	0.00058	Y_{max}	12.016	μ_{nit}	1.6219
k_{np}	0.00818	λ_{an}	fixed at 100	s_{lps}	1158.7
k_{nd}	0.00039	k_A	0.0038	k_{lps}	27240
μ_{nr}	3.0008	k_1	0.8257	μ_{lps}	2.6421
μ_n	0.59336	k_2	0.05597	s_g	84.131
k_{de}	11.762	c_1	103.48	μ_{gly}	0.80734
k_{dn}	0.02982	c_2	106.95	k_{gly}	1.7424
α_x	1.2697	c_3	2.0714	μ_Y	12.039
x_{dn}	0.2617	c_4	2055.7	$elas_b$	0.51786
μ_d	0.04848	c_5	0.15979	$P(0)$	1
$N(0)$	0	$D(0)$	0	$C_A(0)$	0.24841
$A_b(0)$	1	$A_n(0)$	1	$X(0)$	0
$L(0)$	2.7794	$Nit(0)$	16.254	$LPS(0)$	0
$G(0)$	110.66	$Gly(0)$	238.83	$Y_b(0)$	6.6332
$Y_n(0)$	6.9875				

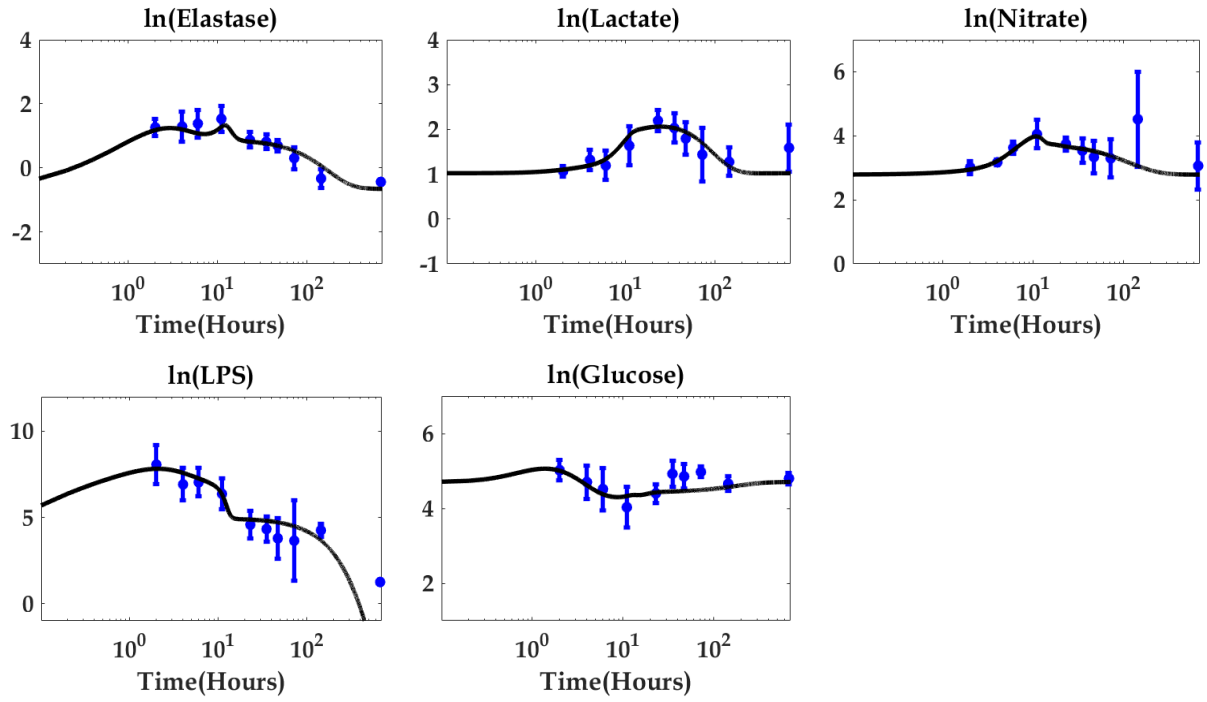

Figure 21: Best fit for the observable trajectories in average of the survivors obtained with OLS with logarithmic time scale. Parameter values and initial conditions are given in Table 7.

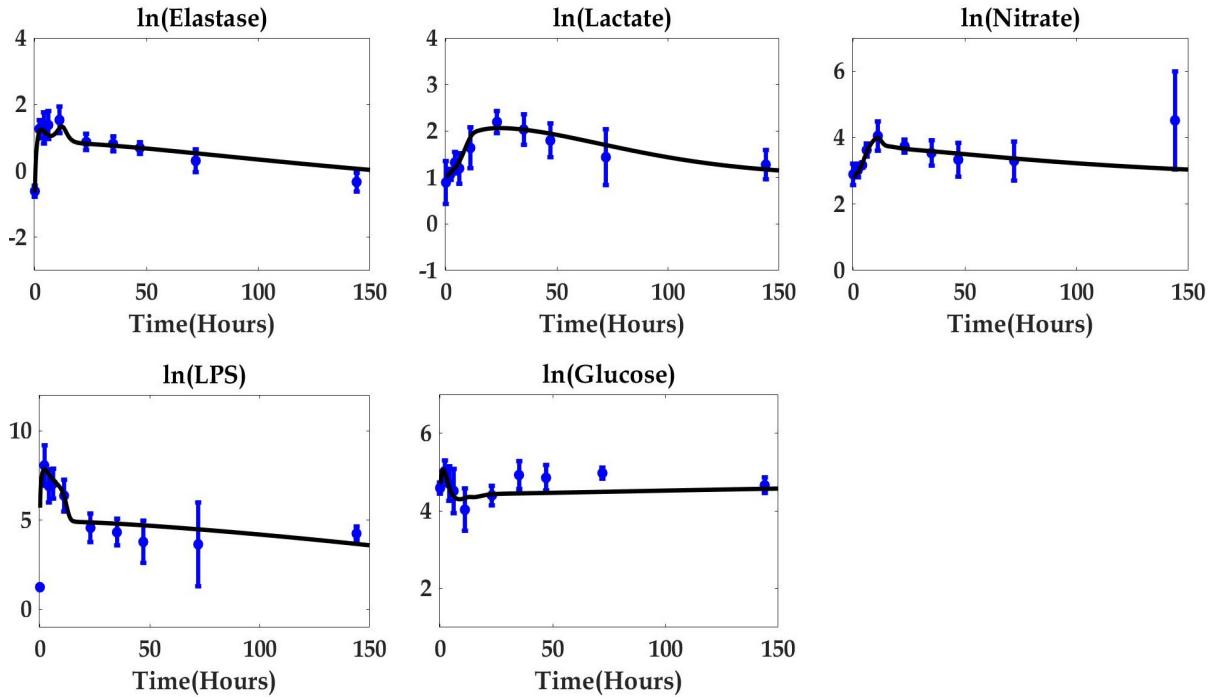

Figure 22: Best fit for the observable trajectories in average of the survivors obtained with OLS in linear scale. Parameter values and initial conditions are given in Table 7.

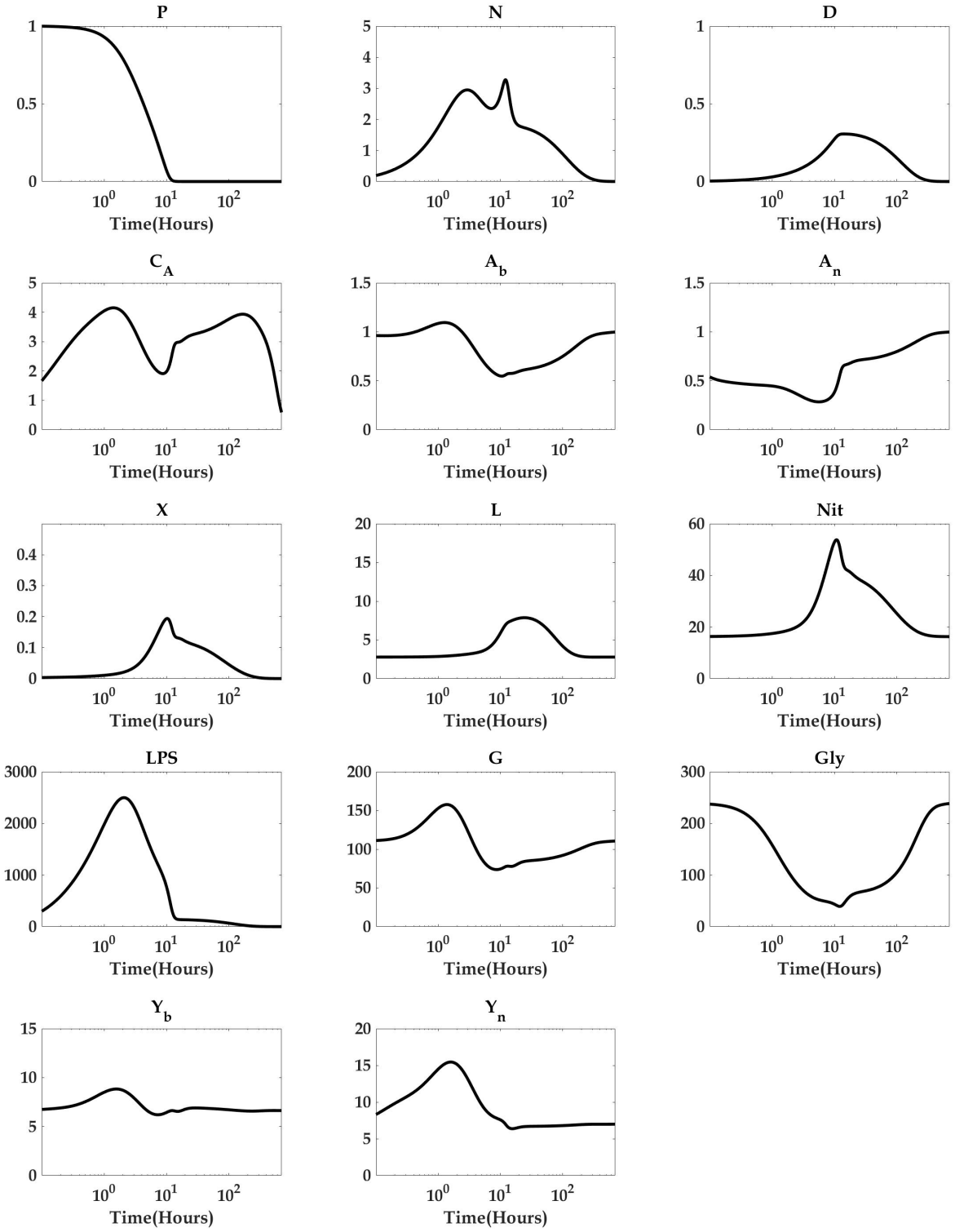

Figure 23: Model trajectories obtained with best fit for the average of the survivors with logarithmic time scale. Values for parameters and initial conditions are given in Table 7.

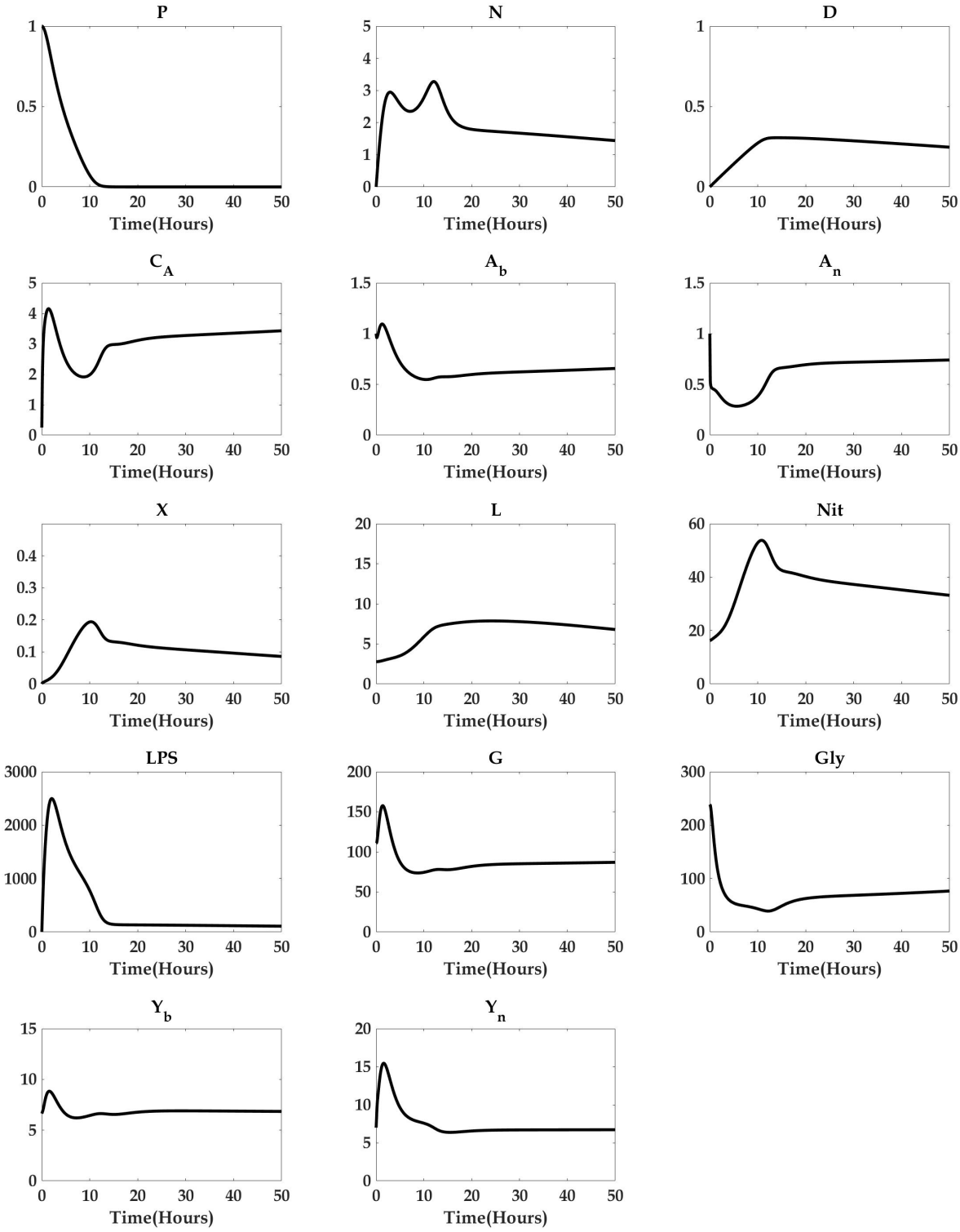

Figure 24: Model trajectories obtained with best fit for the average of the survivors in linear scale. Values for parameters and initial conditions are given in Table 7.

4.3 Bayesian inference for parameter estimation

In the Bayesian inference setting it is standard to work with the statistical model

$$Y_i = f(t_i, \Theta) + \mathcal{E}_i\,; \qquad i = 1, \cdots, n \tag{39}$$

Here $f(t_i, \Theta)$ represents the parameter dependent model response, and $Y_i, \mathcal{E}_i$, and Θ are assumed to be random variables representing measurements, measurement errors, and parameters, respectively [68].

We assume the random variable of unknown vectors Θ has realizations θ with corresponding distribution $\pi(\theta)$, also known as the prior distribution. The prior distribution contains any prior information we may know about the parameter vector θ. If information of the parameter of interest can be found in the literature or can be estimated experimentally, we may assume its prior distribution is given by a Gaussian distribution with certain mean and standard deviation. However, if no previous information is known about this parameter, it is preferred to use a non-informative prior. In biological models for instance, it is common to work with positive parameters and usually no other information is known. If this is the case, one can use a non-informative prior defined as an improper uniform density given by $\pi(\theta) = \chi_{(0,\infty)}(\theta)$, [68].

The posterior distribution $P(\theta|y)$, which is our quantity of interest, corresponds to the probability distribution of the parameter θ given the observed data y. Determining the posterior distribution using prior information given by the observed data can be done by making use of the so called Bayes formula:

$$P(\theta|y) = \frac{P(y|\theta)\,\pi(\theta)}{P(\theta)} \tag{40}$$

Bayes formula provides a relation between the posterior distribution, the prior distribution and the likelihood function. The likelihood function $P(y|\theta)$, corresponds to the probability of obtaining the data y given the parameter value θ. The term $P(\theta)$ is the probability distribution of the observed data. This last term is a normalization factor to ensure the posterior is a number between 0 and 1. This normalization factor can be computed by

$$P(\theta) = \int_{\mathbb{R}^N} P(y|\theta)\,\pi(\theta) d\theta \tag{41}$$

where N is the number of unknown parameter values.

As shown in [68], if we assume that the measurement errors $\mathcal{E}_i$ are independent and identically distributed (iid) and that they are given by a normal distribution centered at 0 and with fixed standard deviation σ^2, the likelihood function is

$$P\left(y|\theta\right) = L(\theta, \sigma^2|y) = \frac{1}{\left(2\pi\sigma^2\right)^{n/2}} e^{-SS_\theta/2\sigma^2} \tag{42}$$

where $SS_\theta = \sum_{i=1}^{n} \left[y_i - f_i(\theta)\right]^2$ is the sum of squares error.

Evaluating the posterior relation given in (40) is usually complicated or even impossible, especially for high dimensional parameter spaces as it involves the evaluation of (41). As an alternative approach, we can construct Markov chains, using Markov Chain Monte Carlo (MCMC) techniques, whose stationary distributions is the desired posterior distribution $P\left(\theta|y\right)$. Evaluating realizations of the chain allow us to sample the posterior to obtain a density for the parameter values based on the observed measurements, [68].

In simple words, the MCMC sampling algorithms generate a chain of random variables that satisfy the Markov property that X_k depends only on X_{k-1}, where the state space X is the space of all possible parameter values. If we suppose a current parameter vector θ^{k-1} is obtained from the chain realization $X_{k-1} = \theta^{k-1}$, a new candidate θ^* is proposed, where θ^* is determined by a proposal or jumping distribution $J\left(\theta^*|\theta^{k-1}\right)$. We then accept θ^* with probability $\alpha\left(\theta^*|\theta^{k-1}\right)$, that is, we let $X_k = \theta^*$ with probability α and let $X_k = \theta^{k-1}$ otherwise. In the Metropolis algorithm we consider the proposal distribution to be symmetric, that is $J\left(\theta^*|\theta^{k-1}\right) = J\left(\theta^{k-1}|\theta^*\right)$.

An important feature of MCMC sampling that makes it an useful technique in Bayesian inference is that we avoid having to compute the term (41), as during the sampling process, the term $P(\theta)$ is canceled when computing the ratio:

$$r\left(\theta^*|\theta^{k-1}\right) = \frac{P\left(\theta^*|y\right) J\left(\theta^{k-1}|\theta^*\right)}{P\left(\theta^{k-1}|y\right) J\left(\theta^*|\theta^{k-1}\right)} \tag{43}$$

$$= \frac{P\left(\theta^*|y\right)}{P\left(\theta^{k-1}|y\right)} = \frac{P\left(y|\theta^*\right)\pi(\theta^*)}{P\left(\theta^*\right)} \frac{P\left(\theta^{k-1}\right)}{P\left(y|\theta^{k-1}\right)\pi(\theta^{k-1})} \tag{44}$$

$$= \frac{P\left(y|\theta^*\right)\pi(\theta^*)}{P\left(y|\theta^{k-1}\right)\pi(\theta^{k-1})} \tag{45}$$

where in the second equality we used the symmetry of the proposal distribution, in the third equality we used Bayes formula (40), and in the fourth and last equality we simplified $P(\theta^*)$ with $P\left(\theta^{k-1}\right)$ as they correspond to the same number given by (41). We refer to $r\left(\theta^*|\theta^{k-1}\right)$ as the ratio of posterior densities. This ratio is then used to compute the probability α mentioned above, as we will discuss in the following section.

4.3.1 Random walk Metropolis algorithm with non-informative prior

In this section we describe the Metropolis algorithm when no prior information is used. Here, the proposal distribution is given by

$$J\left(\theta^*|\theta^{k-1}\right) = N\left(\theta^{k-1}, V\right) \quad or \quad J\left(\theta^*|\theta^{k-1}\right) = N\left(\theta^{k-1}, D\right) \tag{46}$$

where V is the covariance matrix of Θ and D is a diagonal matrix whose elements represent the scale corresponding to each parameter value. These choices for the proposal are motivated to scale the variability of each parameter component [68].

The algorithm to construct a chain X of length M is as follows:

1. We start by choosing an initial parameter θ^0 such that $P(\theta^0|y) > 0$
2. For $k = 1, \cdots, M$ we propose the candidate $\theta^* = \theta^{k-1} + Rz$, where $z \sim N(0,1)$ and R is the Cholesky decomposition of V.
3. Compute the ratio $r\left(\theta^*|\theta^{k-1}\right)$.
4. Set

$$\theta^k = \begin{cases} \theta^* & \text{, with probability} \quad \alpha = min(1, r), \\ \theta^{k-1} & \text{, otherwise.} \end{cases} \tag{47}$$

The step 2 of the algorithm corresponds to the Markov step, as θ^k depends only on the previous $(k-1)$-th iteration. The construction of θ^* ensures that $\theta^* \sim N(\theta^{k-1}, V)$ or $\theta^* \sim N(\theta^{k-1}, D)$ [68].

In the case of a non-informative uniform prior, the ratio $r\left(\theta^*|\theta^{k-1}\right)$ is reduced to the ratio of likelihoods

$$r\left(\theta^*|\theta^{k-1}\right) = \frac{P(y|\theta^*)}{P\left(y|\theta^{k-1}\right)} = e^{-\left[SS_{\theta^*} - SS_{\theta^{k-1}}\right]/2\sigma^2} \tag{48}$$

Therefore it is clear that $r > 1$ implies $P(y|\theta^*) > P\left(y|\theta^{k-1}\right)$ which in turn implies that $SS_{\theta^*} < SS_{\theta^{k-1}}$ and then we accept θ^* with probability 1, as θ^* provides a smaller sum of squares. On the other hand, if $r < 1$, we accept θ^* with probability $\alpha = r$. Finally, we note that when the prior distribution is non-symmetric, we obtained a generalized version of the Metropolis algorithm called the Metropolis-Hastings algorithm.

The covariance matrix V used in step 2 is estimated by

$$V = \sigma^2_{\hat{\theta}_{OLS}} \left[\chi^T\left(\hat{\theta}_{OLS}\right)\chi\left(\hat{\theta}_{OLS}\right)\right]^{-1} \tag{49}$$

and

$$\sigma^2_{\hat{\theta}_{OLS}} = \frac{1}{n-N}\sum_{i=1}^{n}\left[y_i - f(t_i, \hat{\theta}_{OLS})\right]^2 \tag{50}$$

where n is the number of data points, N is the number of unknown parameters, $\hat{\theta}_{OLS}$ is the parameter vector obtained in the OLS that corresponds to the best fit trajectory found in Section 4.2, and $\chi_{ik}(\theta) = \dfrac{\partial f(t_i,\theta)}{\partial \theta_k}$ is the sensitivity matrix.

Finally, if prior information is known about the parameters, step 2 is then adapted to include this prior. For example, if parameters are known to be normally distributed with mean μ and standard deviation σ, we propose candidates $\theta^* = z$ where $z \sim N(\mu, \sigma^2)$, [74].

The chain X consists of all accepted vector parameters θ^k. To allow the chain to reach stationarity and therefore converge to the posterior distribution it is required to disregard the first part of the chain that may have transition behavior across different local minima. This initial period is called the burn-in period. The exact length of the burn-in period is an entire topic of discussion. However, a standard technique is to monitor the paths of the chain associated to each parameter, [68].

4.3.2 Delayed rejection adaptive Metropolis algorithm (DRAM)

The DRAM algorithm was introduced by Hario et. al [37]. A simplified description of the algorithm and implementation can be found in [68]. Here we summarize the most important remarks addressed in [68].

Adaptive algorithms, including the DRAM algorithm, use information learned about the posterior distribution as the candidates parameters are accepted. As the name suggests, the

DRAM algorithm consists of two stages, an adaptive metropolis (AM) part and a delayed rejection (DR) part. The AM uses information learned about the posterior through the accepted chain candidates to update the proposal via the chain covariance matrix. DR alters the proposal function to improve mixing.

The AM part of the algorithm starts with an initial stage of length k_0 where adaptation has not begun. In this stage the chain values $\theta^0, \theta^1, \cdots, \theta^{k-1}$ are calculated using the initial covariance matrix $V_0 = V$ where V is given as in the Metropolis algorithm. Once this initial stage ends, adaptation begins by updating the covariance matrix at the k-step by

$$V_k = s_N \text{cov}\left(\theta^0, \theta^1, \cdots, \theta^{k-1}\right) + \epsilon I_N \tag{51}$$

where s_N is a design parameter that depends on the number of unknown parameters N, commonly chosen as $s_N = 2.38^2/N$, according to [37]. It is important to note that adaptive algorithms are no longer Markovian processes, as they use information about more than one previous state of the chain. The addition of the term ϵI_N allows V_k to be positive definite, where we take $\epsilon \geq 0$ and I_N is the $N \times N$ identity matrix.

As we discussed above, in the standard Metropolis algorithm the candidates are either accepted with probability $\alpha(\theta^*|\theta^k)$ or rejected, in which case the previous candidate θ^{k-1} is retained. The delayed rejection algorithm provides a second alternative candidate θ^{*2} which is chosen instead of rejecting and retaining the previous candidate.

We accept the second candidate with probability

$$\alpha_2\left(\theta^{*2}|\theta^{k-1}, \theta^*\right) = \min\left(1, \frac{P\left(\theta^{*2}|v\right) J\left(\theta^*|\theta^{*2}\right) J_2\left(\theta^{k-1}|\theta^{*2}, \theta^*\right)\left[1 - \alpha\left(\theta^*|\theta^{*2}\right)\right]}{P\left(\theta^{k-1}|v\right) J\left(\theta^*|\theta^{k-1}\right) J_2\left(\theta^{*2}|\theta^{k-1}, \theta^*\right)\left[1 - \alpha\left(\theta^*|\theta^{k-1}\right)\right]}\right) \tag{52}$$

where

$$J_2\left(\theta^{*2}|\theta^{k-1}, \theta^*\right) = N\left(\theta^{k-1}, \gamma_2^2 V_k\right) \tag{53}$$

is the proposal function to choose the second-stage candidate. The notation $J\left(\theta^{*2}|\theta^{k-1}, \theta^*\right)$ indicates that we are proposing θ^{*2} having started at θ^{k-1} and rejected θ^*. Here V_k is as in (51) and $\gamma_2^2 < 1$ to ensure the second proposal is narrower than the first one.

The combination of AM and DR provides two different mechanisms that complement each other to modify the proposal. With the chain covariance matrix, AM updates the

proposal using information learned about the posterior through accepted chain candidates. The DR improves mixing by modifying the proposal function in a predetermined manner. Such modifications in the proposal are temporary and have the goal to stimulate mixing. However, the AM produces permanent changes that reflect information learned about the posterior, [68].

The Metropolis algorithm uses parameter scaling and variability in the proposal as seen in equation (46). However, one of the advantages the DRAM algorithm offers is that it provides a mechanism to incorporate information obtained during the run of the chain about the posterior distribution [37], [68].

More details about the form of α_2 can be found in [68]. The construction of a jth-stage candidate, the acceptance condition, and more details about the DRAM algorithm can be found in [37]. The MATLAB toolbox used to run our MCMC simulations in the following sections can be found at the website `https://mjlaine.github.io/mcmcstat/`.

4.3.3 Space distribution of virtual subjects

In this section we describe the construction of an ensemble of virtual subjects using the DRAM algorithm. We denote this distribution X_{tot} as it will be used to resemble the space of all possible septic patients. Ideally this distribution will include patient heterogeneity observed in real patients. As the DRAM algorithm is based on the Metropolis algorithm, we need to define the sum of squares used in equation (48) to compute the ratio of likelihoods. In fact, when fitting survivors we use:

$$SS_\theta = \frac{1}{N_{pt}-1} SS_{LPS} + \frac{1}{N_{pt}} \left(SS_L + SS_{Elas} + SS_{Nit} \right) + \frac{1}{N_{pt}-3} SS_G \tag{54}$$

Here N_{pt} is the number of time points for the corresponding subject that is being fitted. When fitting survivors, $N_{pt} = 11$, but when fitting non-survivors N_{pt} varies depending of the time of death of the corresponding subject. That is, each sum of squares is normalized by the number of observed data points. Because subjects were fed during times t_7, t_8, and t_9, we will not consider these data points when fitting the glucose trajectory. Also, instead of imposing any heuristic on the first LPS data point, we decided to not include it in the fitting and allow the algorithm to freely choose at this time point.

In order to fit the non-survivors we define

$$\begin{aligned} SS_\theta = &\frac{1}{N_{pt}-1} SS_{LPS} + \frac{1}{N_{pt}} \left(SS_L + SS_{Elas} + SS_{Nit}\right) \\ &+ \frac{1}{N_{pt}-N_{gp}} SS_G + 100H(1 - D_{model}(N_{pt})) \end{aligned} \tag{55}$$

where the last term is a Heaviside function that is used as a heuristic to force the algorithm to search for parameters in the non-survival regime. Also, N_{gp} corresponds to the number of glucose points that are not being fitted. Because non-survivors data may or may not include t_7, t_8, and t_9, then N_{gp} can be either 0,1,2, or 3.

The individual sum of squares terms are given by

$$\begin{aligned} SS_{LPS} &= \sum_{i=2}^{N_{pt}} \left[\frac{\ln(LPS_{data}(t_i)) - \ln(LPS_{model}(t_i,\theta))}{\ln(LPS_{SD})}\right]^2 \\ SS_L &= \sum_{i=1}^{N_{pt}} \left[\frac{\ln(L_{data}(t_i)) - \ln(L_{model}(t_i,\theta))}{\ln(L_{SD})}\right]^2 \\ SS_{Elas} &= \sum_{i=1}^{N_{pt}} \left[\frac{\ln(Elas_{data}(t_i)) - \ln(Elas_{model}(t_i,\theta))}{\ln(Elas_{SD})}\right]^2 \\ SS_{Nit} &= \sum_{i=1}^{N_{pt}} \left[\frac{\ln(Nit_{data}(t_i)) - \ln(Nit_{model}(t_i,\theta))}{\ln(Nit_{SD})}\right]^2 \\ SS_G &= \sum_{\substack{i=1 \\ i\neq 7,8,9}}^{N_{pt}} \left[\frac{\ln(G_{data}(t_i)) - \ln(G_{model}(t_i,\theta))}{\ln(G_{SD})}\right]^2 \end{aligned}$$

where unlike in the OLS step, we are normalizing by the constant $\ln(V_{SD})$ which corresponds to the average of the standard deviation for measurement V at all time points. Finally, for simplicity, when computing $r(\theta^*|\theta^{k-1})$ in equation (48), we use $\sigma^2 = 1$.

To construct the total distribution X_{tot} we proceed as follows:

1. For $i = 1, \cdots, 16$
   a. Use DRAM to generate the chain X_i corresponding to the ith-subject.
   b. Take a random subsample of X_i called $\hat{X}_i$.
2. Let $X_{tot} = \bigcup_{i=1}^{16} \hat{X}_i$

In step 1.a we use the individual data for the i-th subject to fit the model using DRAM and thus obtain an ensemble X_i. Each ensemble X_i consists of $M = 200000$ parameter vectors of size $N_p \times 1$. Here, $N_p = 55$ is the number of free parameters to be estimated and M is the length of the chain, i.e. the number of virtual patients in the ensemble. We repeat this process for each subject to obtain 16 ensembles of size $M \times N_p$. The number M corresponding to the length of the chain was arbitrarily chosen and it can be increased or decreased. Keeping this number large however, will help to obtain convergence of the chain. In order to remove the initial transition of the chain to achieve a minima, a burn-in of length 50000 iterations was thrown away for each chain.

To illustrate this process, in Fig. 25 we present the marginal path trajectories obtained when fitting subject S89 with DRAM. The chain path does not stagnate suggesting the proposal is neither too narrow nor too wide. This situation is ideal as it suggests there was a rich chain mixing and substantial exploration of the parameter space. The stationarity of the chains indicates that they have burned-in and are sampling from the posterior density. As depicted in the figure, the length of each path trajectory is 2×10^4 where the burn-in portion of the chain has already been discarded.

Along with the chain, we compute marginal densities for each of the individual fits. Fig. 26 depicts the marginals obtained when fitting S89 with DRAM. More localized marginals provide a sense of the likelihood of each parameter. For example, for subject $S89$, it is more likely to observe β values between 0.8 and 0.94. Whereas for μ_A it is more likely to attain values between 21.2 and 29.08. On the other hand, flatter marginal distributions suggest that the corresponding parameters are not uniquely identifiable.

Each chain also allows us to quantify uncertainty on the observable and model trajectories. This uncertainty can be observed for instance in Fig. 27, which shows the envelopes of the observed variables for the four survivor subjects S89, S90, S100, and S101. Similarly, in Fig. 28 we also present the envelopes for four of the non-survivors; NS73, NS74, NS88, and NS98. We also present the envelopes of model trajectories for subjects S89 in Fig. 29 and NS73 in Fig. 30.

In step 1b, from each of the 16 distributions X_i, we select random samples of size $M/16 = 12500$ to obtain subsample distributions $\hat{X}_i$ of the same size. In step 2, we collect all these

subsamples and combine them to form the total space distribution X_{tot}. In other words, X_{tot} is a collection of 16 distributions, where each distribution was created by sampling parameters that fit each individual subject with certain probability. Therefore the ensemble in X_i is a set of parameters that resembles the uncertainty when collecting the data of the i-th subject. Moreover, this construction ensures that the total space distribution will consist of a chain of parameter vectors $\theta^1, \theta^2, \cdots, \theta^M$ such that when θ^i is evaluated into the model equations (12) - (25) its outcome results in either a survivor or a non-survivor trajectory.

The marginal densities of the total distribution X_{tot} are shown in Fig. 31. Because this is a combination of the marginals of all 16 subjects we obtain wider and flatter densities than in the individual case and no many conclusions can me made at first sight. However, this gives us a sense of how parameters are distributed within their initial domain in the entire virtual population and in some cases, like is the case with k_{pg}, β, k_A, etc, we can estimate their value based with certain likelihood.

Although no prior information is being used for the individual fits in step 1a, the DRAM algorithm requires bounds to define the domain of each of the sampling parameters. To define this domain, we use the parameter vector $\hat{\theta}_{OLS}$ found in Section 4.2, which corresponds to the best fit to the trajectory of the average of the survivors. Assuming patients behave more or less like the average of the survivors, we define the interval $I_{\hat{\theta}_{OLS}} = \left[\frac{1}{2}\hat{\theta}_{OLS}, 2\hat{\theta}_{OLS}\right]$ to determine the parameter bounds to be used in the DRAM algorithm.

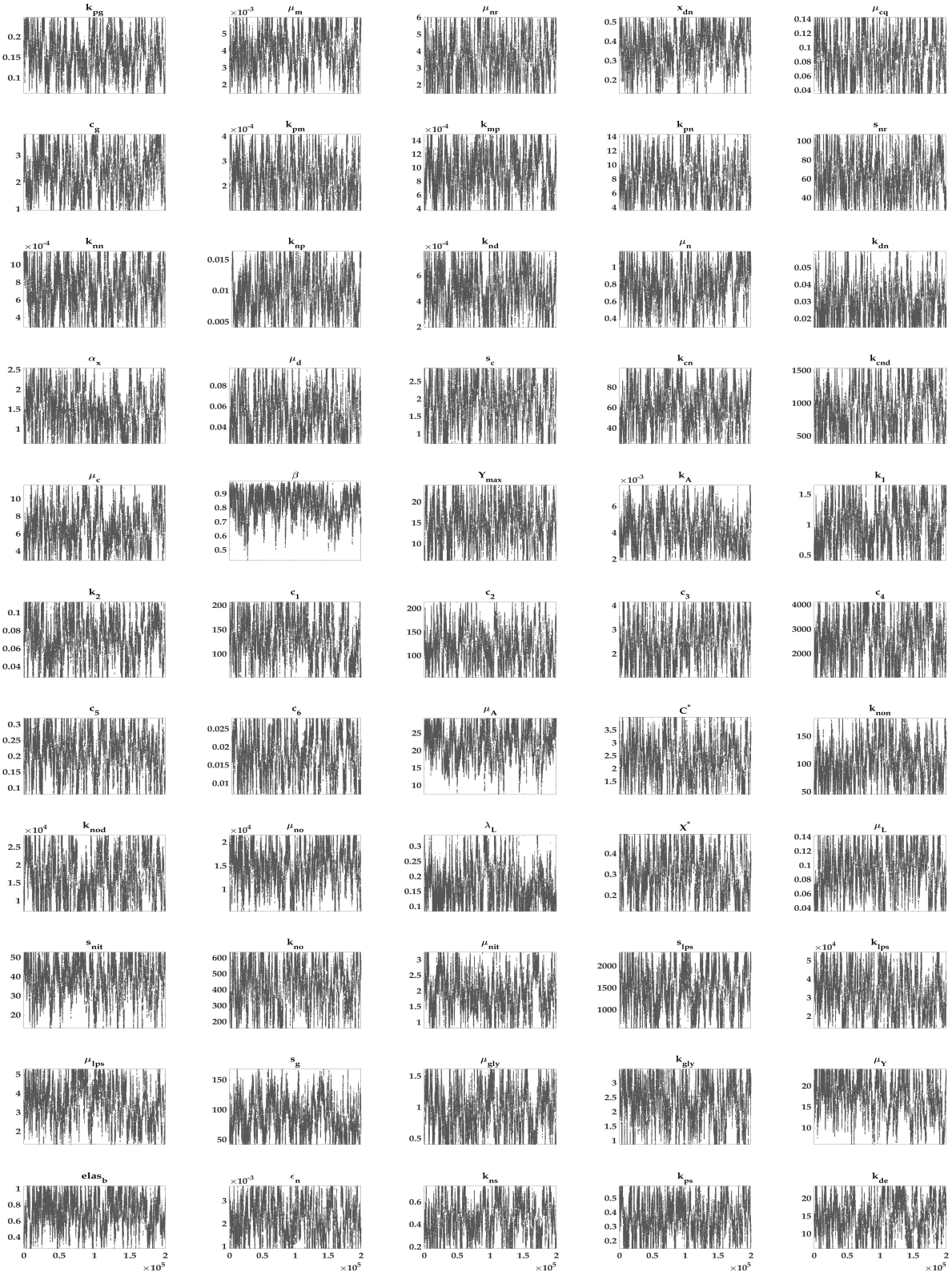

Figure 25: Parameter chain paths obtained with DRAM when fitting S89. The y-axes contain the parameter domains and in the x-axes the number of elements in the chain.

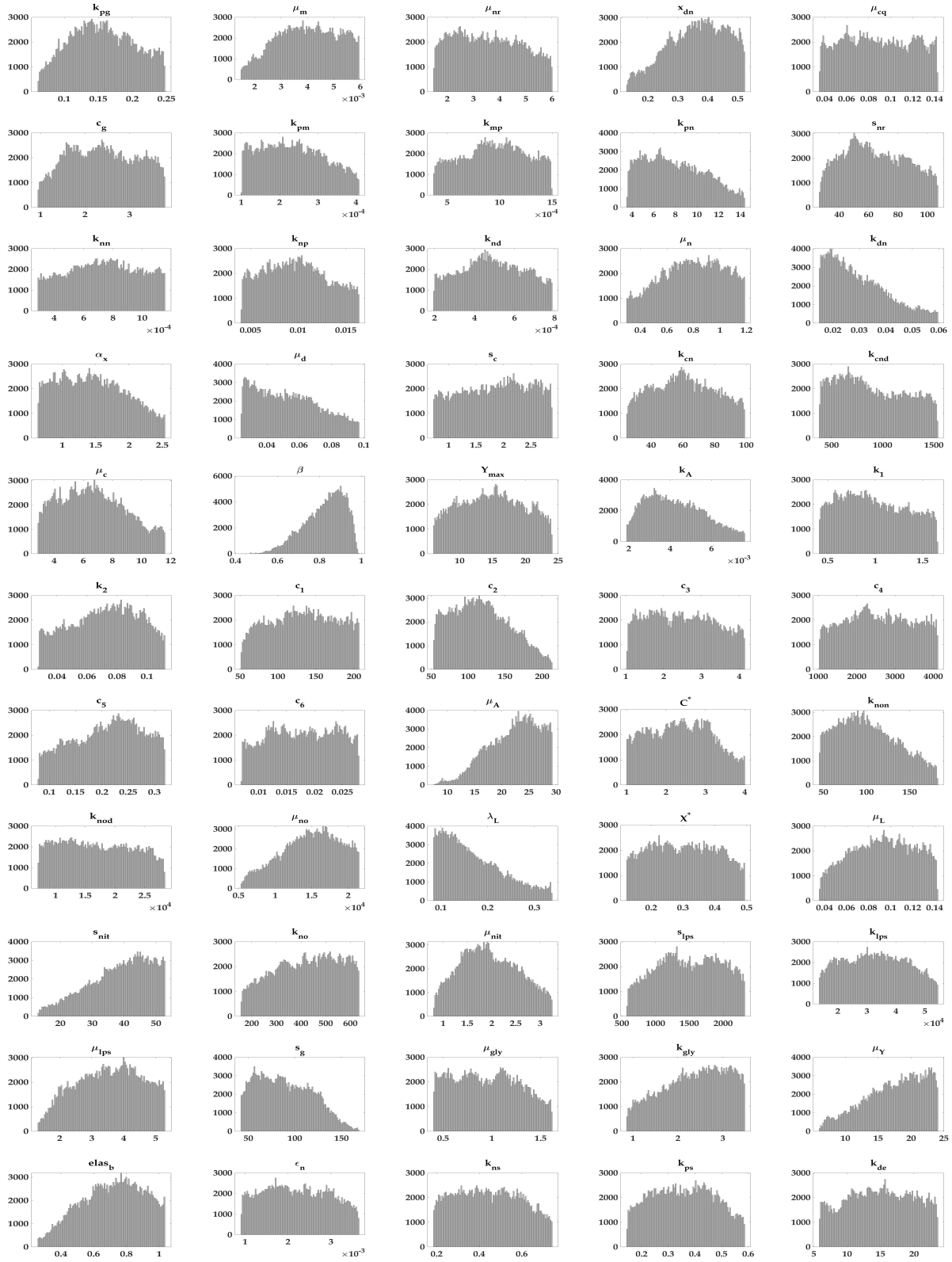

Figure 26: Marginal parameter densities obtained with DRAM when fitting S89. The parameter domains are shown in the x-axes whereas parameter frequency are shown on the y-axes.

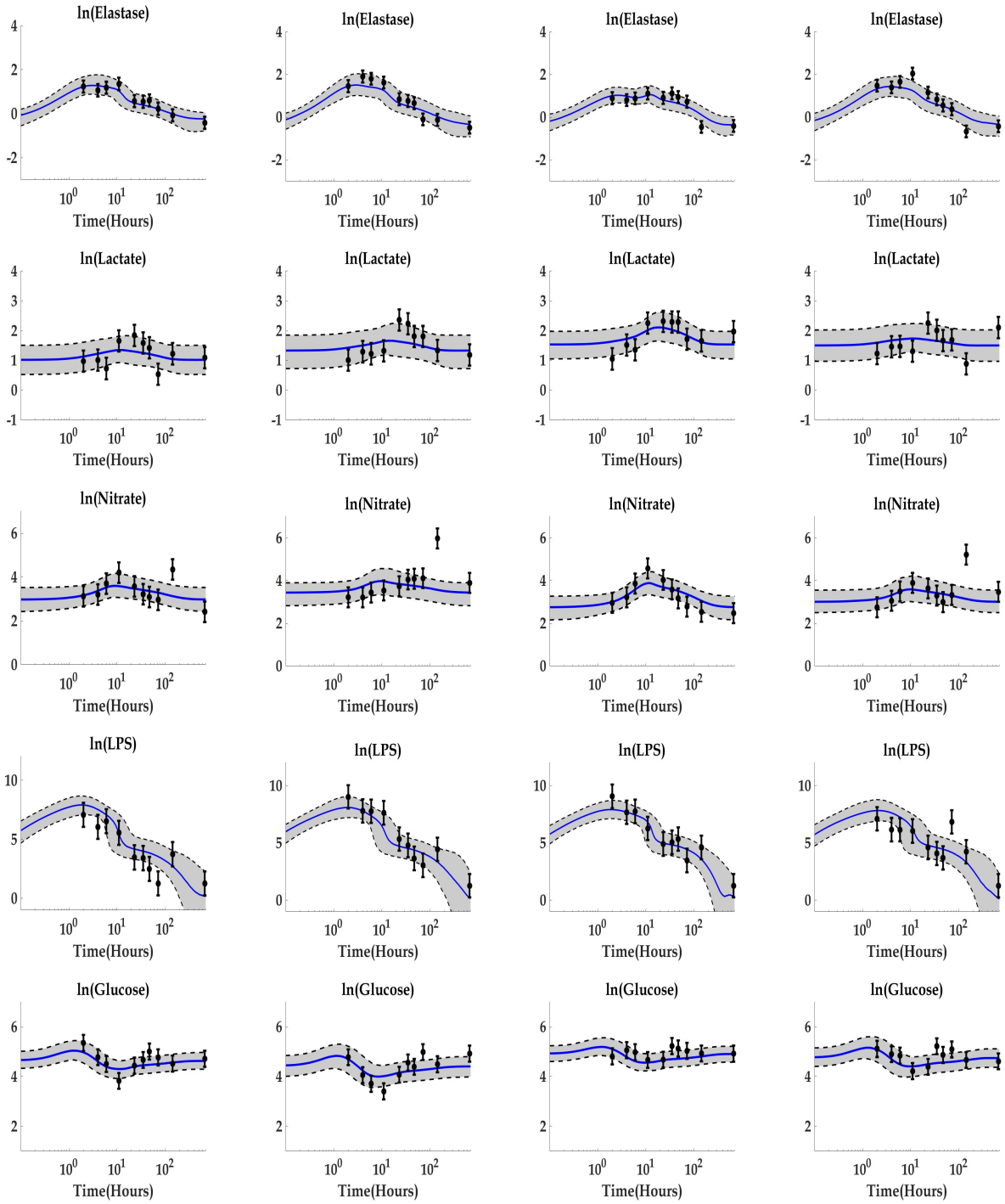

Figure 27: Envelopes of observed trajectories for subjects (a) S89, (b) S90, (c) S100, and (d) S101 obtained with DRAM. The solid blue line corresponds to the median of the sampled trajectories and the shaded gray regions enclose the $5\% - 95\%$ confidence intervals. The black dots correspond to the data and the bars the average of the standard deviation of the treated non-survivors.

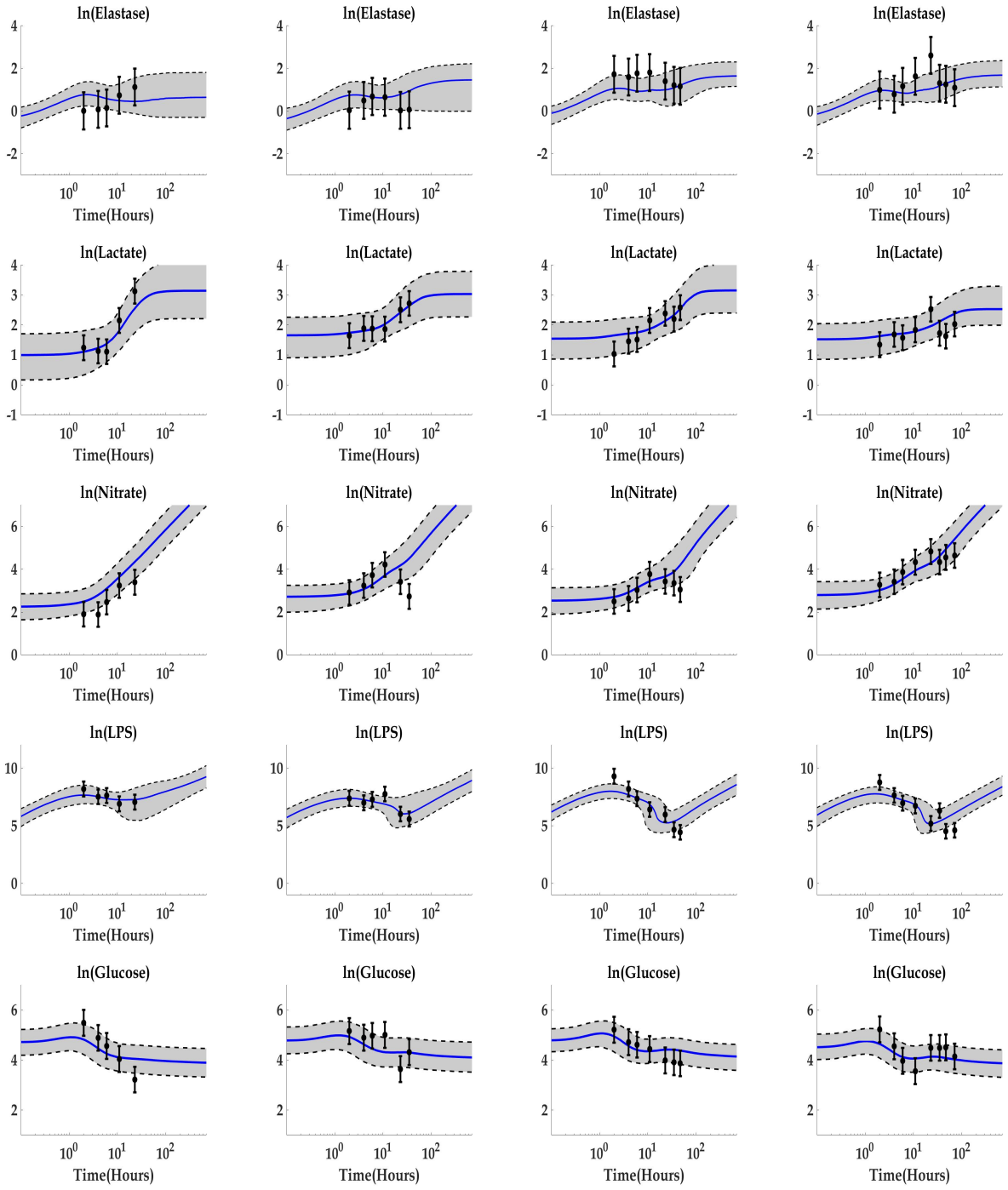

Figure 28: Envelopes of observed trajectories for subjects (a) NS73, (b) NS74, (c) NS88, and (d) NS98 obtained with DRAM. The solid blue line corresponds to the median of the sampled trajectories and the shaded gray regions enclose the $5\% - 95\%$ confidence intervals. The black dots correspond to the data and the bars the average of the standard deviation of the treated non-survivors.

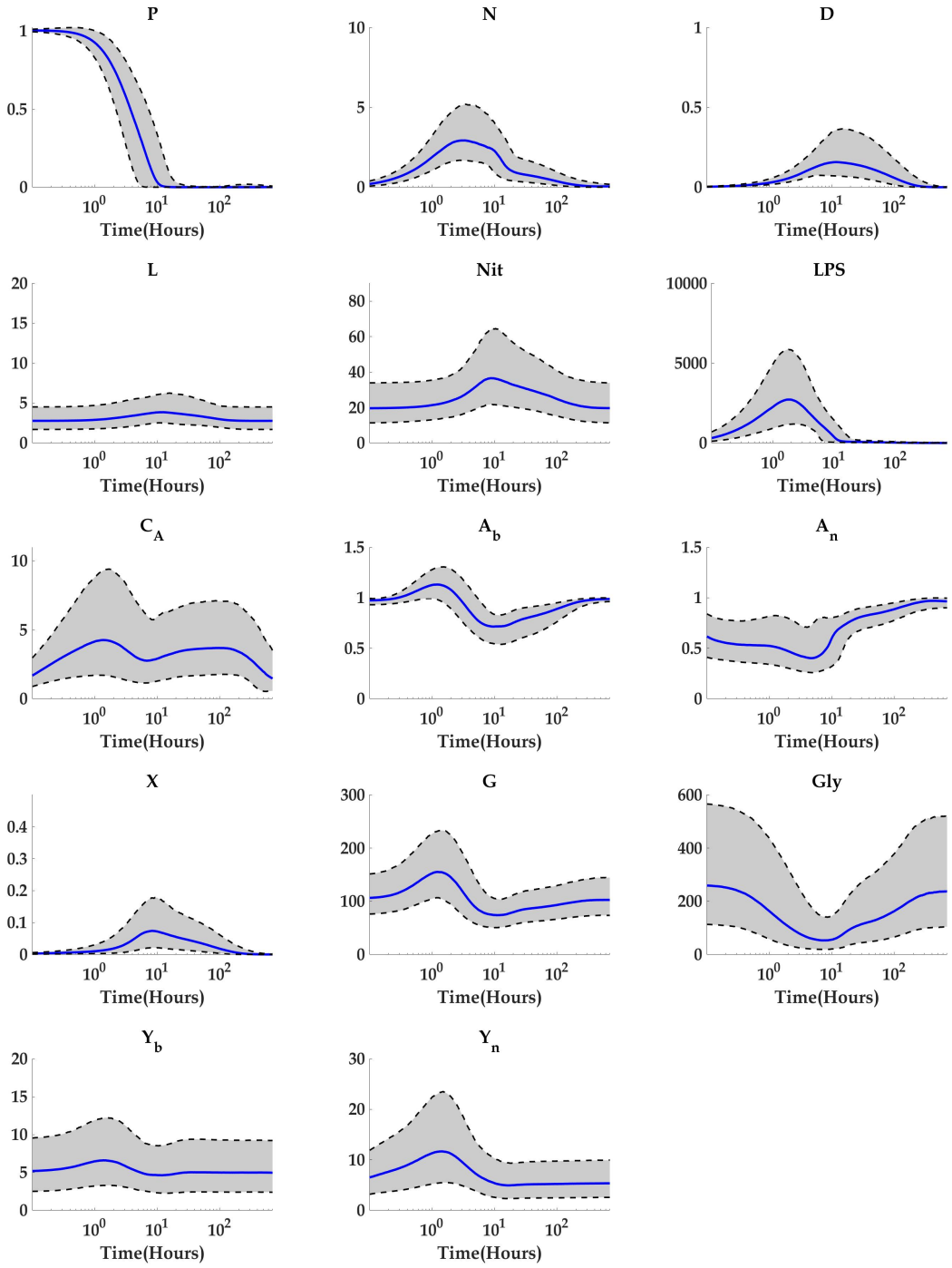

Figure 29: Predicted intervals of model trajectories obtained with best fit for subject S89. The solid blue line corresponds to the median of the sampled trajectories and the shaded gray region bounded by the black dashed lines enclose the $5\% - 95\%$ confidence interval.

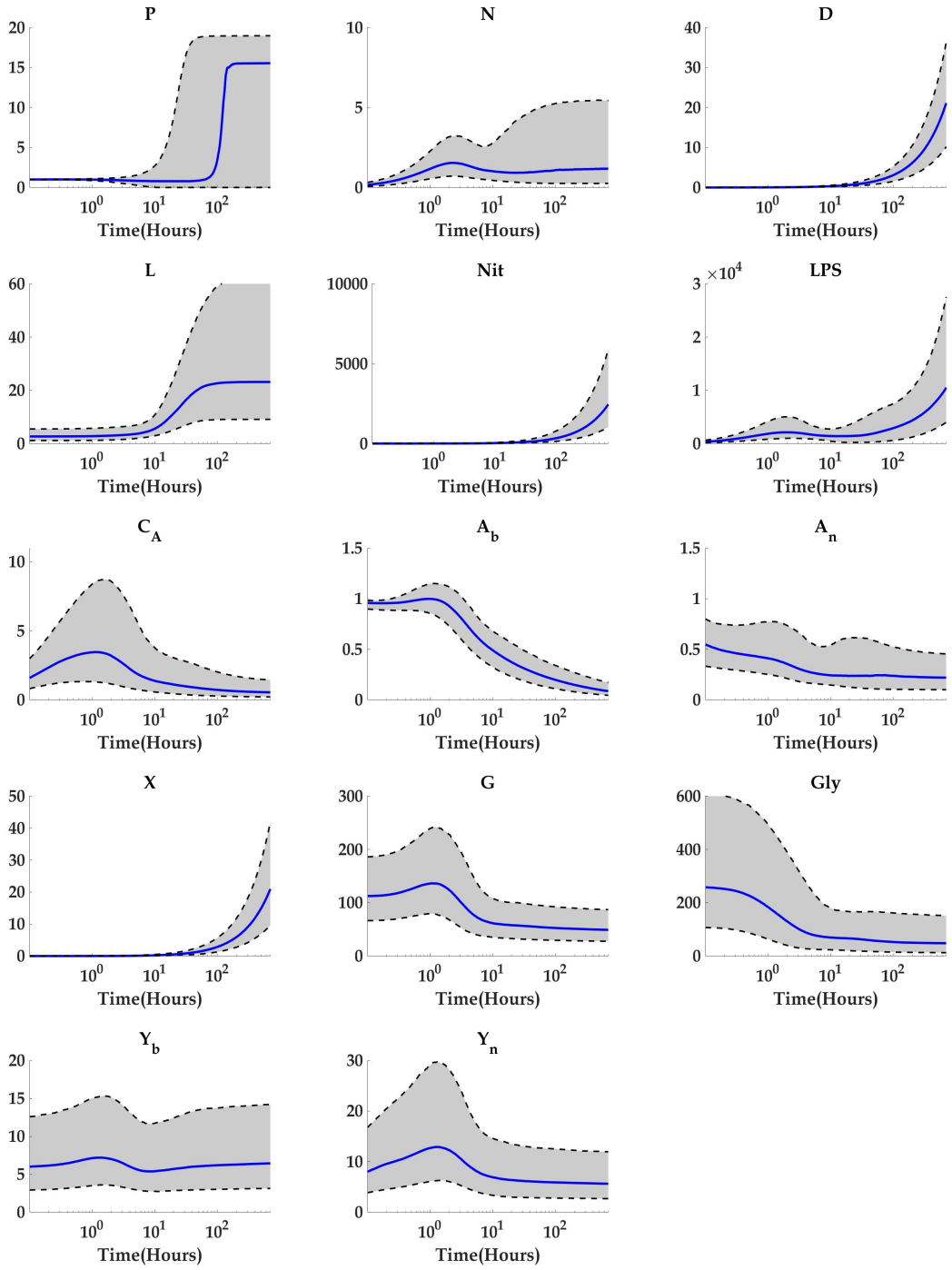

Figure 30: Predicted intervals of model trajectories obtained with best fit for subject NS73. The solid blue line corresponds to the median of the sampled trajectories and the shaded gray region bounded by the black dashed lines enclose the $5\% - 95\%$ confidence interval.

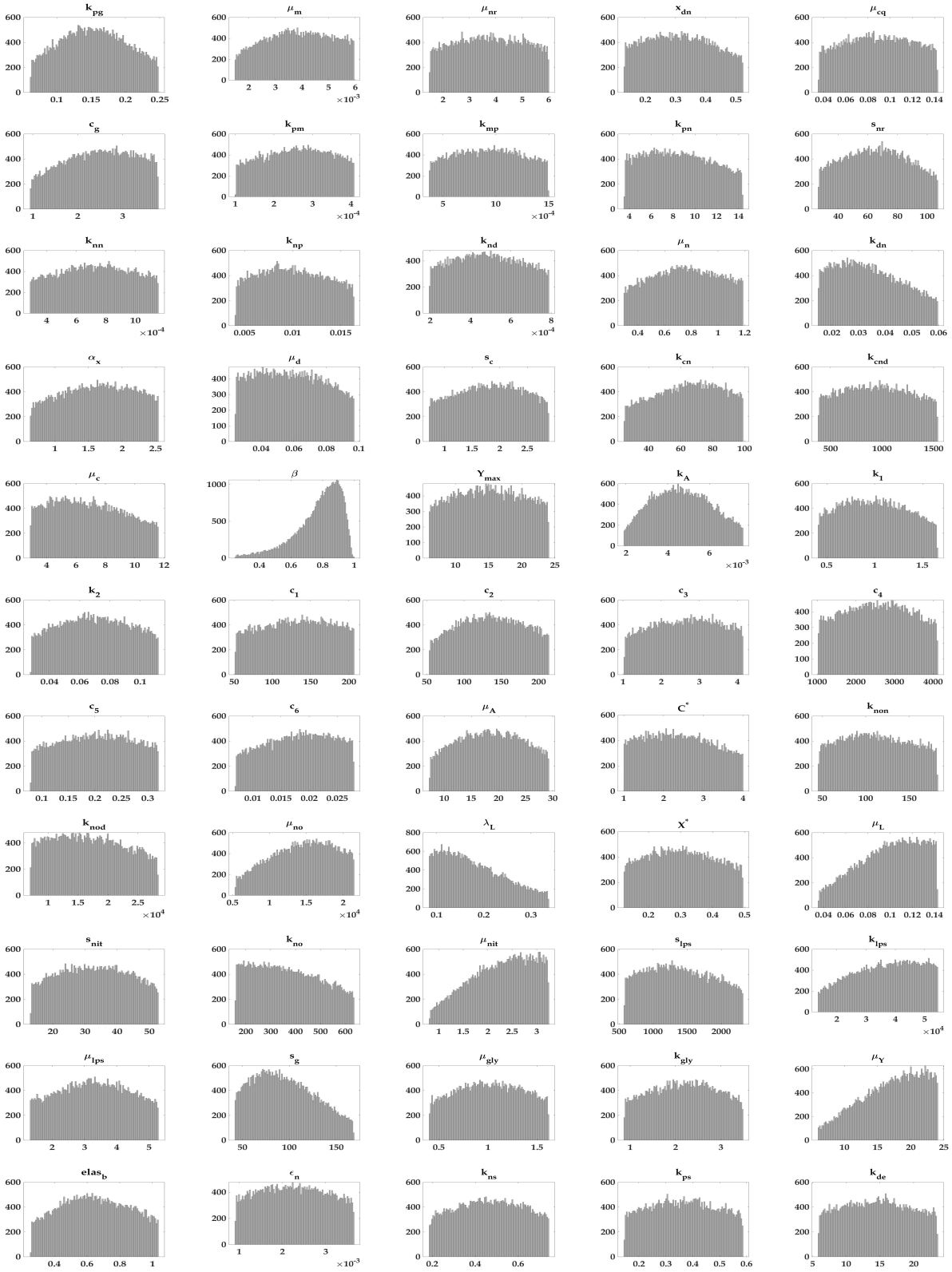

Figure 31: Marginal parameter densities of total distribution X_{tot}. The y-axes contain parameter frequencies and x-axes parameter domains.

4.3.4 Validation of the total distribution

In this section, we use the Random Walk Metropolis Algorithm described in Section 4.3.1, but this time with an informative prior. In particular, proposed candidates will be randomly chosen from the total distribution X_{tot} rather than with the process described in step 2 in Section 4.3.1. However, candidates θ^* at the $k-$th stage will still be accepted with probability α or taken as θ^{k-1} if rejected.

We use the Metropolis algorithm with informative prior to fit each of the 16 subjects data in the placebo group, to determine whether the model can provide results that are consistent with the data. For instance, if we plug the data of the survivor subject S89 into our Metropolis algorithm with informative prior, we expect to obtain a high survival probability. Similarly, if we plug the data of a non-survivor subject like NS66, we expect the model to predict high mortality probability.

Table 8: Metropolis with informative prior: individual fits for non-treated subjects

Subject	Prob. Surv.	Prob Non-Surv	Subject	Prob. Surv.	Prob Non-Surv
NS66	2.46%	97.54%	S89	100%	0%
NS67	36.58%	63.42%	S90	100%	0%
NS69	0.08%	99.2%	NS92	0.5%	99.5%
NS73	0.72%	99.28%	NS97	3.92%	96.08%
NS74	58.8%	41.2%	NS98	49.78%	50.22%
NS76	2.04%	97.96%	S100	100%	0%
NS80	6.76%	93.24%	S101	100%	0%
NS88	56.06%	43.94%	NS104	17.32%	82.68%

On Table 8, we present a summary of the results of what the model predicts when implementing Metropolis with X_{tot} as informative prior to fit each of the 16 sets of data from the non-treated cohort. For the most part, the model is able to predict patient outcome for the available data, with the exception of the non-survivor subjects NS67, NS74, NS88,

and NS98. There are several reasons of why the algorithm is not providing an accurate prediction for these cases. According to Fig. 32a, when fitting subject NS67, the algorithm chooses parameters from several distributions but mostly from the distributions obtained with NS67 and S100, with a slightly higher amount from NS67. This suggests that the data sets of these two subjects are relatively similar and therefore high survival probability is estimated for subject NS67, despite the fact that NS67 is a non-survivor subject. The same behavior is observed when fitting the data of subject NS98 seen in Fig. 32d, although this time the algorithm is also selecting parameters from the distributions of S90, S100, and S101, suggesting again that NS98 and these three survivors have similar data trajectories. A similar situation is observed when fitting NS74 and NS88, as depicted in Fig. 32b and Fig. 32c, respectively. Here we note that Metropolis experiences difficulties and selects considerably more trajectories from S100, resulting in high survival probability contradicting the fact that these two data set trajectories are of two non-survivor subjects.

Finally, these four subjects survived at least for 35 hours and therefore the model might be biased towards survival because of the length of the data. Based on this last observation, we study the case where we consider only the first 5 and 6 time points on each of these subjects. As shown in Table 9, reducing the number of time points results in more accurate predictions from our model. This suggest that the proper recording of measurements during the first 11 and 23 hours is crucial to predict patient outcome.

In Fig. 33 we observe the evolution of the algorithm when NS88 is fitted with 5, 6, and 9 data points. We note that in the fewer data point cases the algorithm picks parameters mostly from the non-survivor distributions rather than the survivor distributions leading to a more accurate prediction.

The algorithm performs remarkably well when predicting survival, as it predicts with 100% probability that subjects S89, S90, S100, and S101 are survivors. However, we are interested to know whether our model can predict survival at earlier times. In particular, we note that when using only 5 and 6 data points we still obtain positive results in 3 out of these four subjects, as observed in Table 10. In Fig. 34 we note how when using all 11 data points for S89, the algorithm selects parameter sets only from the four survivor distributions. But as we reduce the number of data points to 6 and 5, the algorithm starts accepting parameter

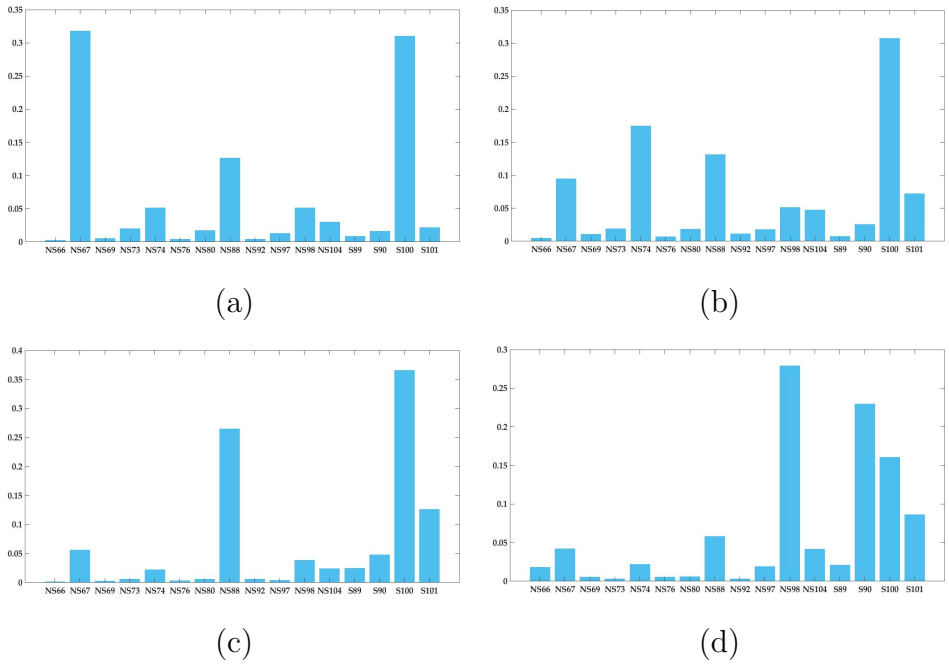

Figure 32: Test results for NS67, NS74, NS88, NS98. The x-axes indicate the distributions constructed with DRAM of the 16 non-treated subjects. The y-axes contain the percentage of occurrence of each distribution.

sets from other distributions. However the algorithm soon recognizes this data is coming from the S89 distribution, resulting in predicting high probability of survival in both cases. Similar behavior is observed in S90 and S101.

In the case of S100 with 5 time points, the model predicts only 41.84% of survival probability and with 6 time points it improves to 59.10%. This suggest that for the first 11 hours, subject S100 was not doing well, but later in the experiment its health improved. The fact that when using the first 5 time points S100 has a relatively high probability of not surviving of 58.16%, is also consistent with what we observed in Fig. 32, where the model seems to find similarities between some non-survival trajectories and S100.

In Fig. 35 we present envelopes of the observable variables along with data when fitting S89 with 5, 6 and 11 time points. As expected, the uncertainty would be larger when fitting

Table 9: Metropolis with informative prior: individual fits on non-survivors non-treated with 5 and 6 data points

	5 time points		6 time points	
Subject	Prob. Surv.	Prob Non-Surv	Prob. Surv.	Prob Non-Surv
NS67	9.7%	90.3%	11.46%	88.54%
NS74	26.76%	73.24%	24.69%	73.31%
NS88	26.74%	73.26%	19.52%	80.48%
NS98	28.33%	71.67%	13.74%	86.26%

less data points than when fitting all 11 data points. However the median trajectory does not vary much across the three cases. The data points that were excluded in each case are colored in red and the first data point at $t = 0$ hours is not shown in the envelopes as time is in logarithmic scale. Similarly, the envelopes of NS88 for 5, 6, and 9 time points are shown in Fig. 36, where we observe that including all data points force trajectories, to level down and hence predicting high survival.

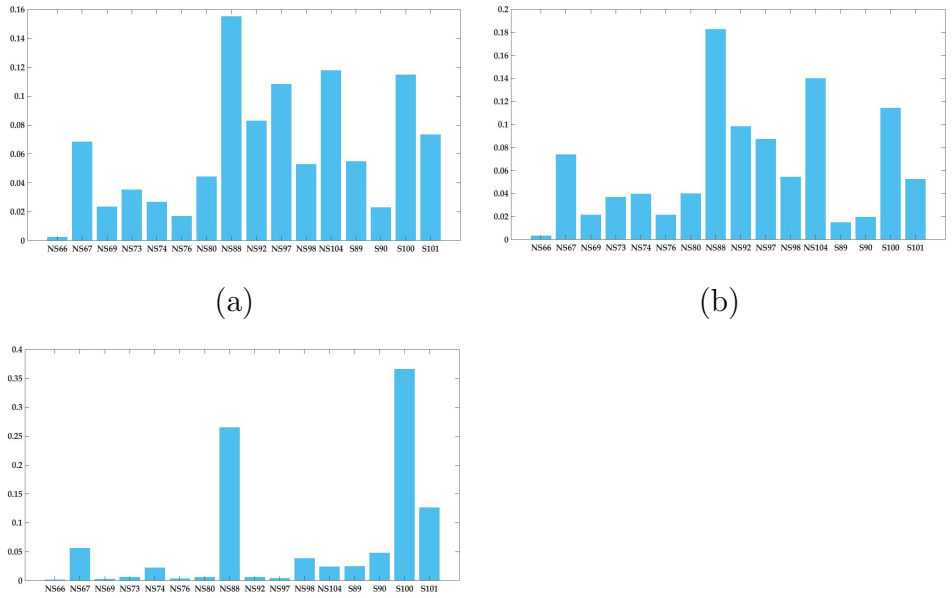

Figure 33: Test results for NS88 with (a) 5 time points, (b) 6 time points, and (c) 9 time points. The x-axes indicate the distributions constructed with DRAM of the 16 non-treated subjects. The y-axes contain the percentage of occurrence of each distribution.

Table 10: Metropolis with informative prior: individual fits on survivors non-treated with 5 and 6 data points

	5 time points		6 time points	
Subject	Prob. Surv.	Prob Non-Surv	Prob. Surv.	Prob Non-Surv
S89	59.18%	40.82%	90.50%	9.50%
S90	60.84%	39.16%	75.20%	24.80%
S100	41.84%	58.16%	59.10%	40.90%
S101	67.10%	32.90%	68.29%	31.71%

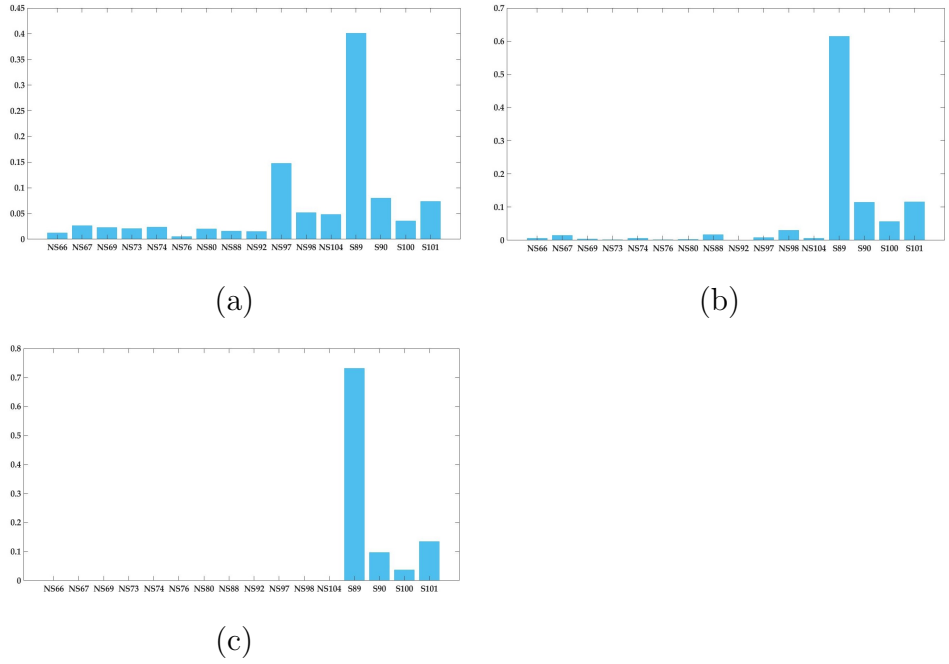

Figure 34: Test results for S89 with (a) 5 time points, (b) 6 time points, and (c) 11 time points. The x-axes indicate the distributions constructed with DRAM of the 16 non-treated subjects. The y-axes contain the percentage of occurrence of each distribution.

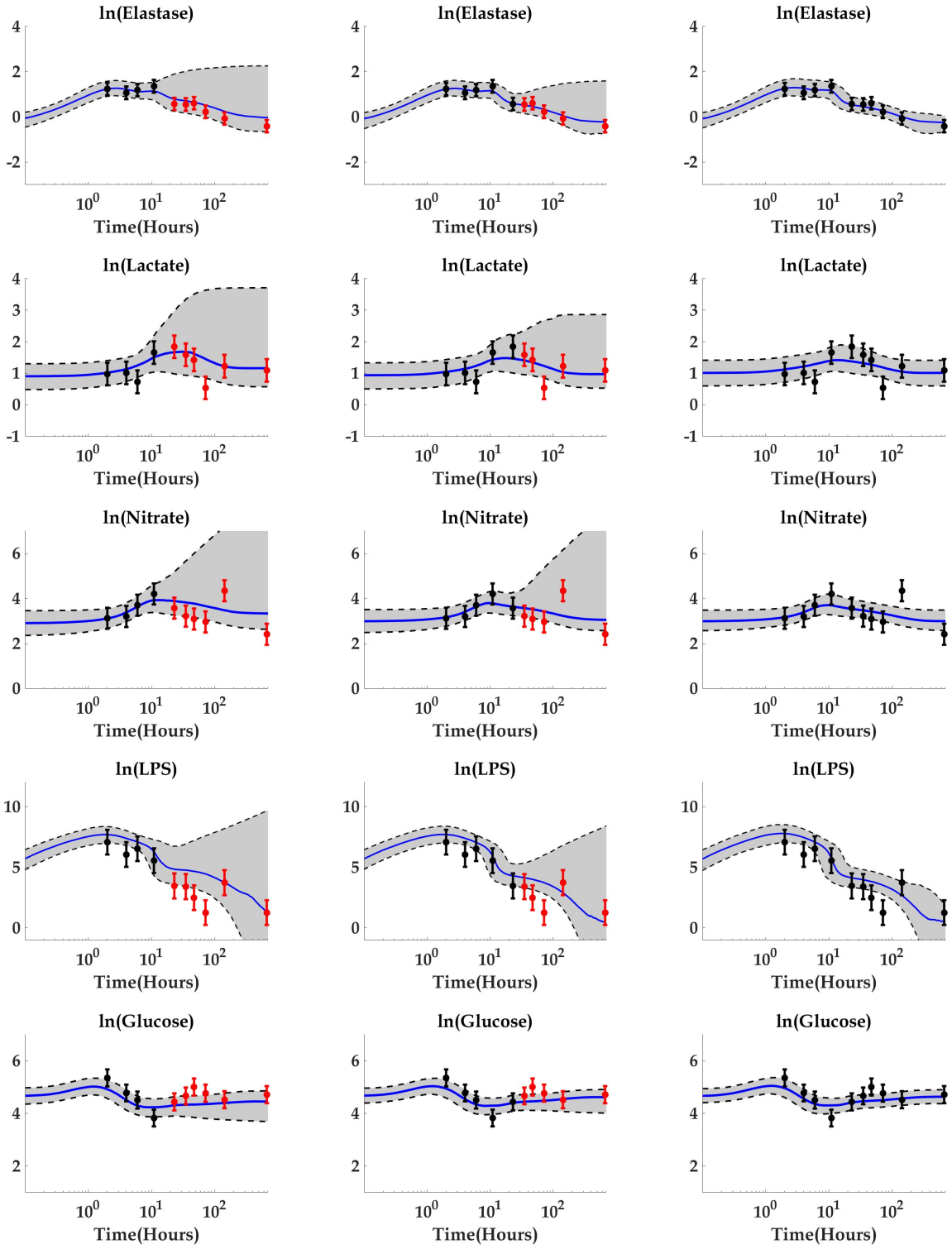

Figure 35: Envelopes for S89 with Metropolis with informative prior using (a) 5 time points, (b) 6 time points, and (c) and 11 time points.

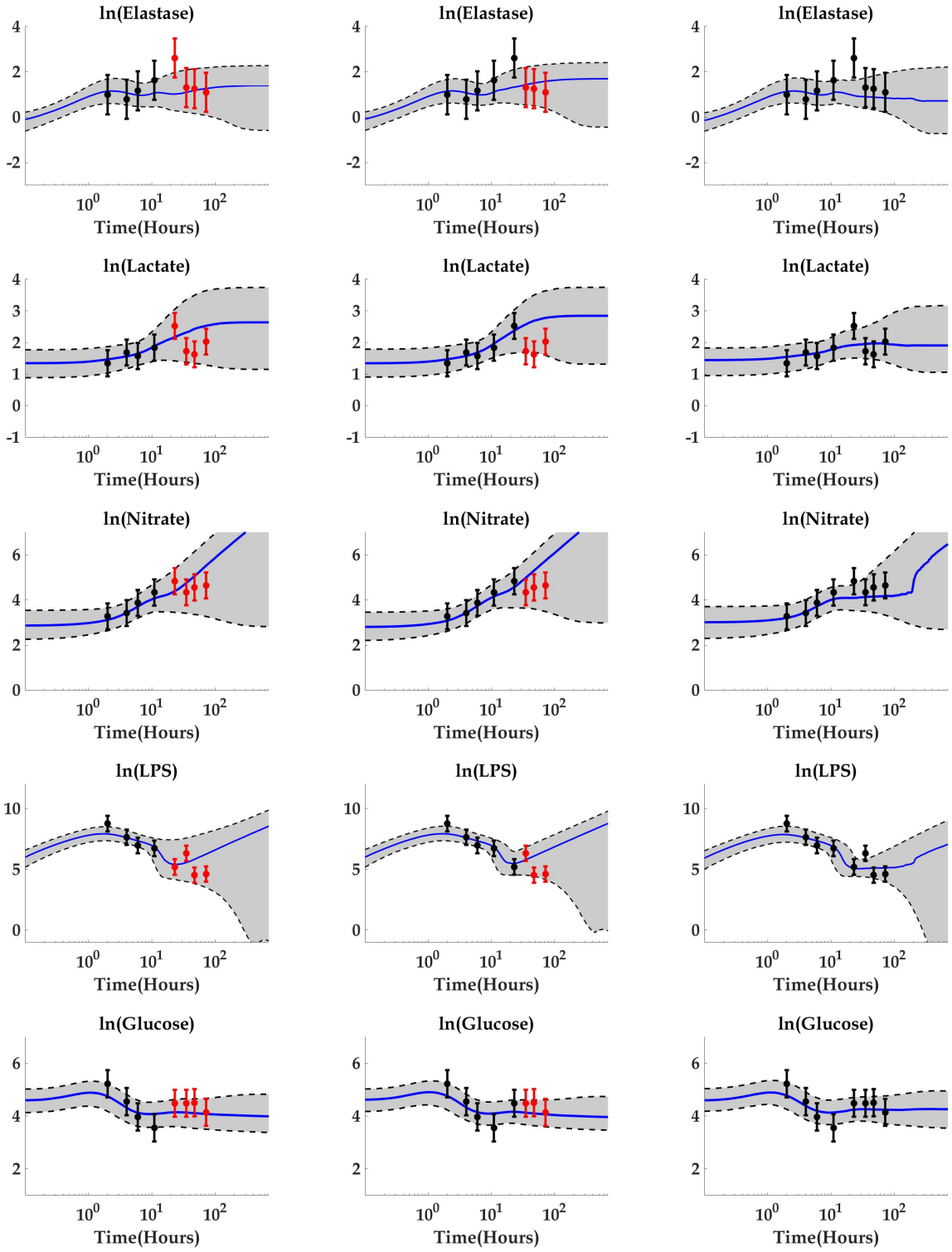

Figure 36: Envelopes for NS88 with Metropolis with informative prior using (a) 5 time points, (b) 6 time points, and (c) 9 time points.

4.4 Discussion

This chapter constitutes an inverse problem on which the goal was to extract information from data to estimate model parameters. Initially, we used an ordinary least squares like approach to find parameter estimates for the average of the 4 survivors observed in the animal study described in Section 3.2. This is based on the assumption that survivors have a similar immune response to overcome the infection. Similarly, we assumed non-survivors immune response is a deviation from a survivor response.

Using the first parameter estimates for the average of the survivors, we then used a Bayesian approach to construct a distribution of parameters called X_{tot}, which reflects the uncertainty observed in a population of septic patients. More specifically, we used a sampling algorithm called DRAM, to first find parameter distributions that quantify the uncertainty observed in the measurements collected for each of the 16 subjects in the animal study. Combining the uncertainties observed in the entire study, we constructed X_{tot}. We assumed that X_{tot} contains enough variability to reflect the heterogeneity a physician may encounter in a diverse population of septic patients. Next, we used X_{tot} as a prior distribution to validate our model via a Metropolis algorithm and the observed data. As a result, we obtained mortality probabilities, that for the most part, were consistent with the true outcome (survivor or non-survivor) of the original data.

We showed that our model can be used to predict probability of mortality given new potential data. The validation process presented in Section 4.3.4 shows that our model can be used to find similarities between data trajectories and predict patient outcome. The model has difficulties predicting outcome for non-survivor subjects who have relatively long time series. However, our results suggest that with 5 and 6 time points it is more likely to obtain a reasonably accurate probability of survival. For this reason, it is important to collect data points during the first phase of infection, that is, within the first 11 to 23 hours after pathogen invasion.

The methods presented in this chapter can be used as a tool to predict patient outcome with certain probability given data measurements of the five observable variables used in our model: elastase, lactate, glucose, LPS, and nitrate. However, caution must be used

when interpreting the results as there are certain limitations. For instance, it is unlikely that our total distribution X_{tot} encloses enough variability to reflect the dynamics of all possible septic patients. Therefore, even if the probability of survival is high, patients health may become compromised for a number of reasons, including preexisting conditions or other biological processes that are not included in the scope of our model. Nevertheless, our model can be used as a complementary tool to evaluate patient's evolution of the infection and help physicians to make more informed decisions. Even though our model is highly complex and allows us to explore the dynamics of an acute immune response during sepsis, the corresponding envelopes do not capture all data points. This is part of the challenges of working with aggregated patient data and to deal with heterogeneity in a real population of septic patients.

The large value estimates in parameters like μ_c, k_{cn}, and s_c, suggest a relatively rapid anti-inflammatory response. One of the model limitations is that we do not capture heterogeneity of different anti-inflammatory cytokines in the body. However, making this distinction would increase the number of state variables and the number of unknown parameters.

Step 3 in the Metropolis algorithm involves the numerical solution of the model for sufficient number of samples. This is a computational expensive process, especially when the model consists of many state variables and high dimensional parameter spaces, which is our case. To speed-up this process we use CVODE as provided through SUNDIALS [40] to solve the system of differential equations. Although CVODE considerably reduces the computational time, it still may take several hours to complete one chain simulation. In order to obtain chain convergence it is recommended make several simulations and therefore increase the computational time. This complicates the use of our model to provide predictions in a reasonable amount of time to treat real patients. Also, the price paid for using CVODE is that for certain parameter choices, the solver does not integrate or even crashes. For those parameters for which the CVODE solver does not perform well we use the stiff solver ode15s in MATLAB 2020a. However, still for a small amount of cases ode15s may also have troubles integrating. Because the number of times this happened was sufficiently low compared to the number of total simulations, it does not affect the results.

Although DRAM improves the standard MCMC sampler, there are other available tools

that can be also used to improve computational time and/or sampling selection. Valderrama-Bahamóndez et. al [81] presented a comparison of the performance of different MCMC techniques including Metropolis-Hastings, parallel tempering MCMC, adaptive MCMC, and parallel adaptive MCMC. They found better results in parallel adaptive MCMC when used to estimate parameters in five ODE models in Systems Biology. Most recently, Bianconi et. al [7], presented an alternative Bayesian method called Conditional Robust Calibration (CRC) and compared it with DRAM and other state of the art approaches such as Profile Likelihood and Approximate Bayesian Computational Sequence Monte Carlo. They found a reduction in computational cost and robust solutions when applying CRC to three biological models. Lastly, improvements in efficiency can be achieved when evolution algorithms combined with self-adaptive randomized sub-space sampling. This is the case of Differential Evolution Adaptive Metropolis (DREAM) [82], [68].

Recent efforts have contributed to the field of inflammation where mathematical models and a variety of parameter estimation tools have been used to calibrate such models to human and animal data. These tools include sensitivity analysis, parameter space reduction, and Latin Hypercube Sampling, [79], [32], [21].

Possible future work to improve our results includes to explore more efficient sampling algorithms like the ones mentioned above, and the addition of new data to extend the prior distribution X_{tot} to enclose higher patient heterogeneity.

5.0 Applications of data-driven model

5.1 Introduction

The use of mathematical models to develop *in silico* trials in virtual patients has been growing in the study of several diseases including cancer, heart disease, and sepsis, [20] [25] [45] [67]. These trials allow us to reproduce patient responses similar to those observed in real patients, with the advantage that they can be repeated as many times as needed and can be used to explore the pros and cons of potential drug therapies.

In this chapter, we begin by using a set of virtual patients constructed in previous sections to explore patient outcome when experiencing underlying metabolic conditions like hypoglycemia and hyperglycemia. We also extend our model to include the dynamics of an NOS inhibitor and explore patient outcome when treating our virtual subjects. Further, we discuss the importance of both early diagnosis and therapy.

We use logistic regression models to identify key biological processes that can be responsible to classify subjects. In particular, we are interested in distinguishing differences in both the placebo and treated groups, first between survivors and non-survivors, and within the non-survivors, differences between septic and aseptic subjects. We also want to understand the effects of energy and energy-related conditions on patient outcome. Lastly, we explore the role of anti-inflammatory mediators and glucose. In particular, we explore how high and low C_A and glucose sources affect a virtual population.

5.2 Inducing hypoglycemia and hyperglycemia

In Section 2.4, we discussed about the role of certain altered metabolic conditions such as hyperglycemia, hypoglycemia, and hypoxia during sepsis. Because our initial model did not include any glucose dynamics in it, we artificially modeled these conditions by tuning some parameters that were involved in ATP availability and in the potential negative effects such conditions have been reported to present during sepsis. We explore the effects of hypoglycemia and hyperglycemia in the baseline population X_{tot} by following a similar approach to that done in Section 2.4. However, the fact that our extended model includes glucose dynamics allows us to induce these conditions in a more direct way. As hypoglycemia is defined as low glucose levels in the blood, we create a hypoglycemic virtual population by reducing glucose production rate by 25% by setting s_g to 3/4 of its original value in all subjects. Similarly, the pro-inflammatory effects of hypoglycemia can be included by increasing phagocyte proliferation-activation by 10%. This is achieved by increasing parameter s_{nr} by 10% for each patient. The choice of 25% and 10% was arbitrary and they can be changed to illustrate other possible scenarios.

Similarly, a hyperglycemic virtual population is constructed. As hyperglycemia corresponds to high levels of blood glucose, we increase glucose uptake by 10% by setting parameter s_g to 1.1 of its original value for every virtual subject. Moreover, hyperglycemia is also known to have negative effects in phagocyte performance, slowing down phagocytosis and in general phagocytic activity. We include this negative effect by reducing phagocytosis by 50%, that is, by reducing k_{pn} to half of its original value for every subject in the virtual population.

We compare these two new virtual populations with a baseline set, which is distributed into 75% non-survivors and 25% survivors. Table 11 shows the percentage effect of hypoglycemia and hyperglycemia when induced in a baseline population of 5000 virtual subjects. Inducing hypoglycemia leads to an increase in the percentage of non-survivors to 96%. Although not as deadly as hypoglycemia, hyperglycemia also increases the probability of death to 80%. This is consistent with the observations made in Chapter 2, on which we noted that hypoglycemia and hyperglycemia benefit sepsis, and that hypoglycemia has a higher

mortality rate.

Numerical issues were found in 8 of the hypoglycemic and 11 of the hyperglycemic subjects and were taken out of the corresponding population without representing any significant impact to the results. We observe a transition from healthy and aseptic subjects into the septic regime in both metabolic conditions. Table 11 also suggest that after inducing these two conditions into an entirely healthy population, we can expect about 85% mortality from hypoglycemia and about 21% mortality in hyperglycemic patients.

Table 11: Inducing metabolic conditions in total population X_{tot}

	Baseline	Hypoglycemia	Hyperglycemia
Health	1252	182	989
Aseptic	3035	2311	2951
Septic	713	2499	1049
Total	5000	4992	4989
Prob. Non-Surv.	75%	96%	80%

The effect of hypoglycemia in the entire population can be seen in the corresponding envelopes shown in Fig. 37. Insufficient glycogen production after the first 10 hours of infection, prevents glucose from recovering in hypoglycemic subjects. As a result, low glucose compromises energy production and with it all the energy dependent processes. In particular, we observe a reduction in phagocytic activity, as well as in anti-inflammatory mediators, compromising both pathogen elimination and down-regulation of the inflammatory response.

An important observation is that the baseline population is not free of hypoglcyemic individuals. As there are some subjects who already have low glucose levels or some other who could eventually become hypoglycemic because their energy is unable to keep up with the demand.

Although hyperglycemia in principle could be thought to be beneficial because of the higher glucose and therefore higher energy levels, in reality hyperglycemia compromises the effectiveness of phagocytosis. This improper phagocytic activity can be better visualized

in the envelope trajectory of the energy flux that corresponds to the energy spent during phagocytosis Φ_2, shown in Fig. 38. The envelopes of all model trajectories of hyperglycemic subjects versus baseline are shown in Fig. 38. In hyperglycemia we also observe an early rise in anti-inflammatory mediators triggered by the initial glucose uptake that last for about the first 10 hours. Later on, glucose starts to be transformed into ATP, as an effort to sustain inflammation. However the poor phagocyte response cannot respond quickly enough to fight the rise in bacteria.

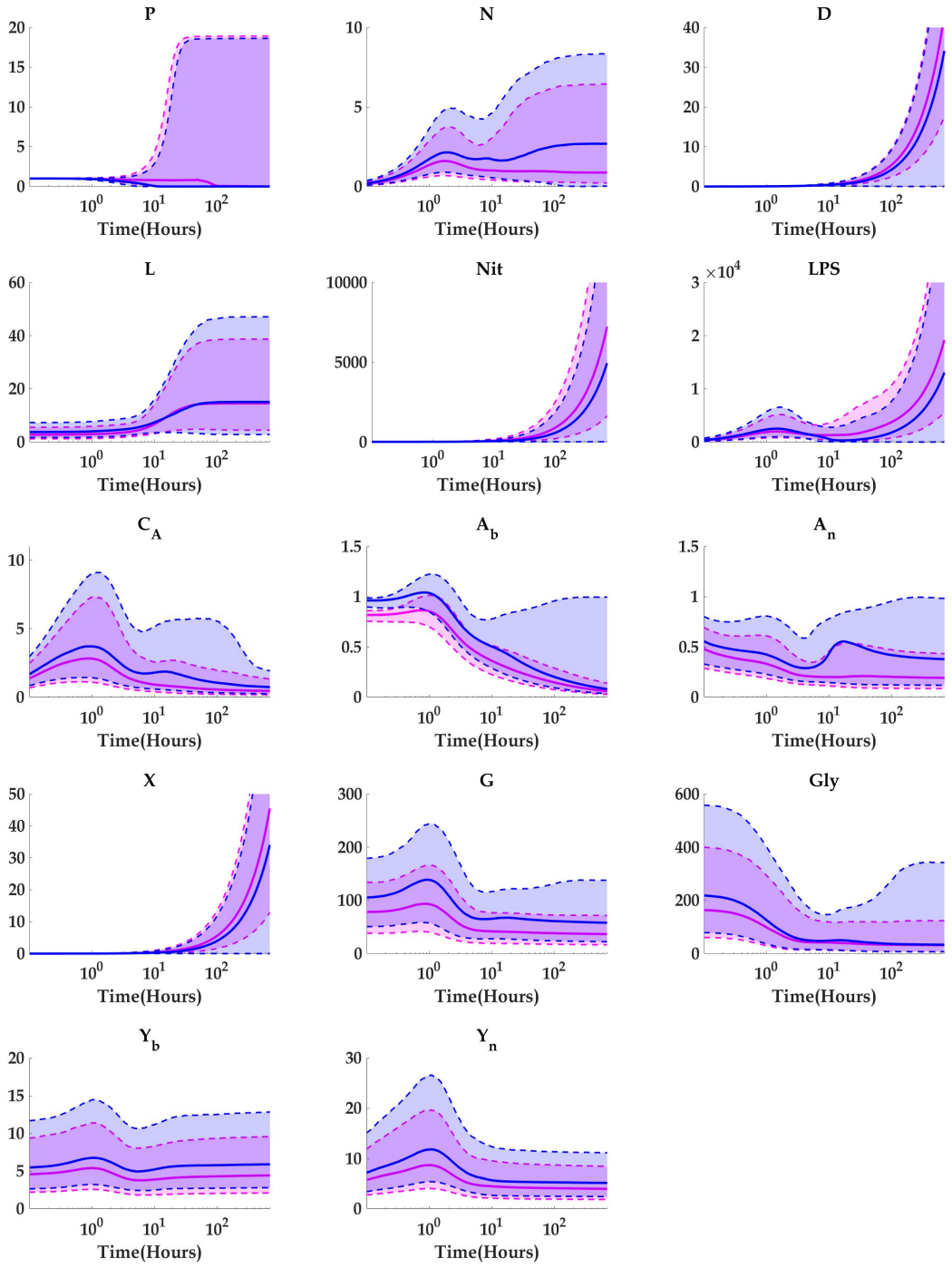

Figure 37: Predicted envelopes of model trajectories obtained with both baseline parameters and inducing hypoglycemia. Baseline trajectories are colored in blue whereas hypoglycemic trajectories are colored in magenta. The solid blue and magenta lines correspond to the median of the sampled trajectories and the shaded regions bounded by the dashed lines enclose the corresponding $5\% - 95\%$ confidence intervals.

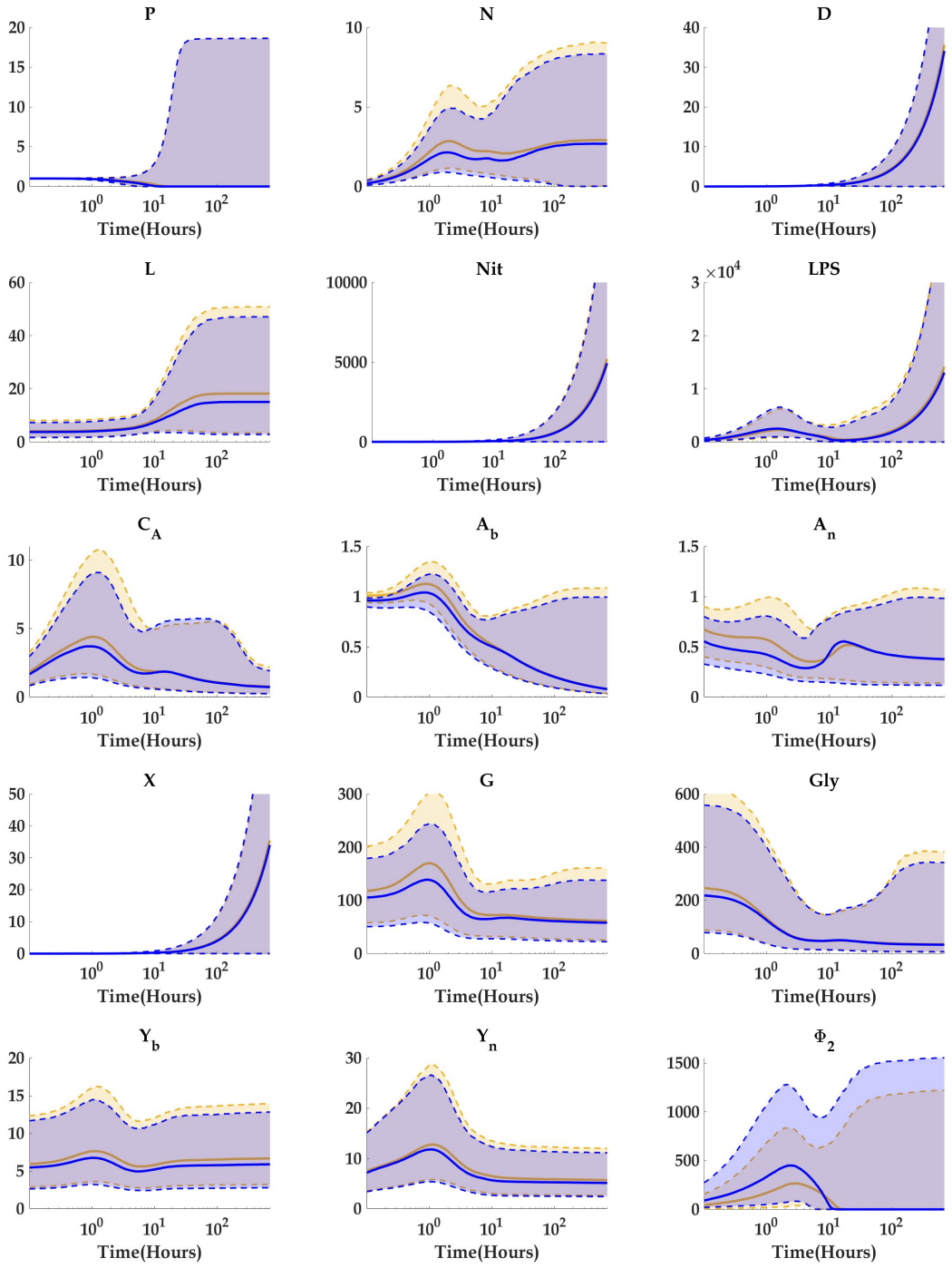

Figure 38: Predicted envelopes of model trajectories obtained with both baseline parameters and inducing hyperglycemia. Baseline trajectories are colored in blue while hyperglycemic trajectories are colored in orange. The solid blue and orange lines correspond to the median of the sampled trajectories and the shaded regions bounded by the dashed lines enclose the corresponding $5\% - 95\%$ confidence intervals.

5.3 Introducing therapy

5.3.1 Modeling therapy

The use of NOS inhibitors to treat septic patients has been an entire topic of discussion over the past two decades, [53], [71]. Although the NOS inhibitor L-NMMA was successful in the baboons study in [62] obtaining 12 out of 16 survivors, the use of this inhibitor in human septic patients has been a source of debate. In fact, a phase II study using the 546C88 inhibitor showed promising results in humans [36], but a subsequent phase III trial was prematurely terminated due to increase in mortality in the treated cohort, [50].

In this section however, we are interested in studying the effect of therapy in the group of baboons who were administered a continuous infusion of the NOS inhibitor 546C88 L-NMMA at 12 hours after sepsis induction. A dose of 5 mg/kg/per hour was given for 36 hours (i.e. until 48 hours after sepsis induction). This inhibitor has been reported to have detrimental effects including tissue and organ damage, increase in the production of pro-inflammatory cytokines, and increase in mortality. However, the authors claim they carefully checked for these and other potential problems and found no negative side effects of 546C88 therapy in the treated cohort, [62].

For this reason when modeling the dynamics of therapy we only include its inhibitory effects on the nitric oxide production. This inhibition effect appears on the updated X equation (56) where k_{th} denotes therapy strength. Therapy itself is modeled by the smooth step function given in equation (57).

$$\frac{dX}{dt} = \frac{1}{1 + k_{th}S} f\left(\frac{C_A}{C^*}\right)(k_{non}N + k_{nod}D) - \mu_{no}X \tag{56}$$

$$S = \frac{1}{\left(1 + e^{500(12-t)}\right)\left(1 + e^{500(t-48)}\right)} \tag{57}$$

The use of 500 in the exponential function in S provides a rapid rise-decay when therapy is turned on-off. As all subjects were given the same dosage, we fixed drug strength at k_{th}=1000. Initially the total population X_{tot} consists of 25% survivors and 75% non-survivors. After applying therapy to this distribution, we obtain a treated distribution which we will denote $X_{tot,th}$, and it now consists of 46% survivors and 54% non-survivors. If therapy is applied

exclusively to the non-survivors in X_{tot}, it results on 30% survivors and the remainder 70% die, even when treatment is administered. This was the highest effect we observed with therapy regardless of considering higher therapy strengths. Variations on S can include a more slow decay rate of drug treatment that can account for the half life of the inhibitor. However, since the half life of the NOS inhibitor used in the study is about 1 hour, we did not observe any significant differences in the effectiveness of treatment.

5.3.2 Metropolis algorithm with informative prior on treated subjects

Once again we use the Metropolis algorithm with informative prior to fit individual data and validate our model. This time the data is taken from the 16 subjects who were treated with an NOS inhibitor. We use the population distribution $X_{tot,th}$ as a prior to find a posterior distribution by following the same procedure described in Section 4.3.4.

Table 12: Metropolis with informative prior: individual fits of treated subjects

Subject	Prob. Surv.	Prob Non-Surv	Subject	Prob. Surv.	Prob Non-Surv
NS68	37.62%	62.38%	S91	96.22%	3.78%
S70	94.62%	5.38%	S93	94.52%	5.48%
NS71	23.71%	76.29%	NS94	89.78%	10.22%
S72	96.72%	3.28%	S95	79.69%	20.31%
S77	96.18%	3.82%	S99	98.46%	1.54%
NS78	55.10%	44.9%	S102	97.28%	2.27%
S79	95.79%	4.21%	S103	99.02%	0.098%
S83	96.73%	3.27%	S106	99.14%	0.86%

In Table 12 we summarize the probabilities of survival obtained when fitting each of the subjects in the treated group with the Metropolis algorithm. Overall the results are consistent with the actual outcome of the corresponding subject, as survivors are predicted to survive with high probability and most of the non-survivors are predicted to die with

relatively high probability. We note however that there are some cases on which the algorithm seems to have difficulties deciding between survivor and non-survivor. That is the case of subject NS78 which is estimated to be a non-survivor with a probability of only 44.89%, despite the fact that this is originally a non-survivor subject. A similar situation occurs when fitting subject NS94, which according to the model it has only 10.22% probabilities of not surviving.

According to the fits, shown in Fig. 39, at the last time points in the data trajectories of NS78 and NS94 (47 and 72 hours, respectively), lactate decreases and levels off at similar values to those before treatment making their trajectories similar to survivor trajectories and hence a lower probability of dying, even after therapy has been stopped. On the other hand, not only NS68 and NS71 have fewer data points, but also there is a rise in their lactate data at 23 and 35 hours. This rise is most likely the reason why their lactate trajectories are predicted to ramp up and saturate at high levels. Although our model is not capturing this rise in lactate during therapy for the non-survivors, the model is able to predict high lactate response at a later time and still predicting high probability of not survival for NS68 and NS71. Work still needs to be done to obtain an earlier rebound in lactate as a consequence of therapy as suggested by the non-survivor data. However, the model is still able to provide important insight on the effect of therapy at the population level, as we discuss in Section 5.4.4.

We also note there is a consistent increased behavior in lactate measurements during therapy across non-survivors, although it appears more evident in NS68, NS71, and NS78. In fact, when comparing non-survivor trajectories with survivors we note that this elevated response in lactate does not occur in survivors, as it can been seen in Fig. 40, where we show the fits and envelopes of 4 of the 12 survivors.

To complement the envelopes of the observed variables, we also present the envelopes of model trajectories of one of the non-survivor subjects, NS68 in Fig. 41. We note that by the time therapy is administered to the subject, pathogens are almost completely gone, leaving tissue damage to be driven mainly by nitric oxide. And as a consequence the fact that therapy down regulates X helps tissue damage to keep decreasing. This effect indirectly affects variables such as C_A , A_b, and L. However, as soon as therapy is over, nitric oxide

jumps back in and is followed by tissue damage and lactate. This rebound in D is soon out of control exhausting the levels of A_b that is in charge of tissue healing.

We also illustrate, how the model performs when fitting survivors by showing the envelopes of the model trajectories of S102 in Fig. 42. The model fits well the effect of therapy in the nitrate trajectory. As a consequence, we note that therapy seems to have an important effect in tissue damage, allowing all inflammatory effects some time to be down-regulated by the high C_A that can be sustained by both ATPs.

Following the same approach done in Section 4.3.4, we recompute the probabilities of survival for subjects NS78 and NS94 by fitting their data trajectories using only their first 5 and 6 time points. It is important to note that the fifth time point occurs one hour before therapy starts and the sixth time point is at 23 hours, while treatment ends until 48 hours.

For subject NS78, the probability of non-surviving improves to be 56.52% when using 5 data points and 52.71% when using 6 data points. For subject NS94, the results also improve compared to when using all the data points. However, the probabilities of non-surviving are still considerably low for the 5 and 6 time points.

Table 13: Metropolis with informative prior: individual fits of treated subjects with 5 and 6 time points

	5 time points		6 time points	
Subject	Prob. Surv.	Prob Non-Surv	Prob. Surv.	Prob Non-Surv
NS78	43.48%	56.52%	47.29%	52.71%
NS94	75.9%	24.1%	56.05%	43.95%

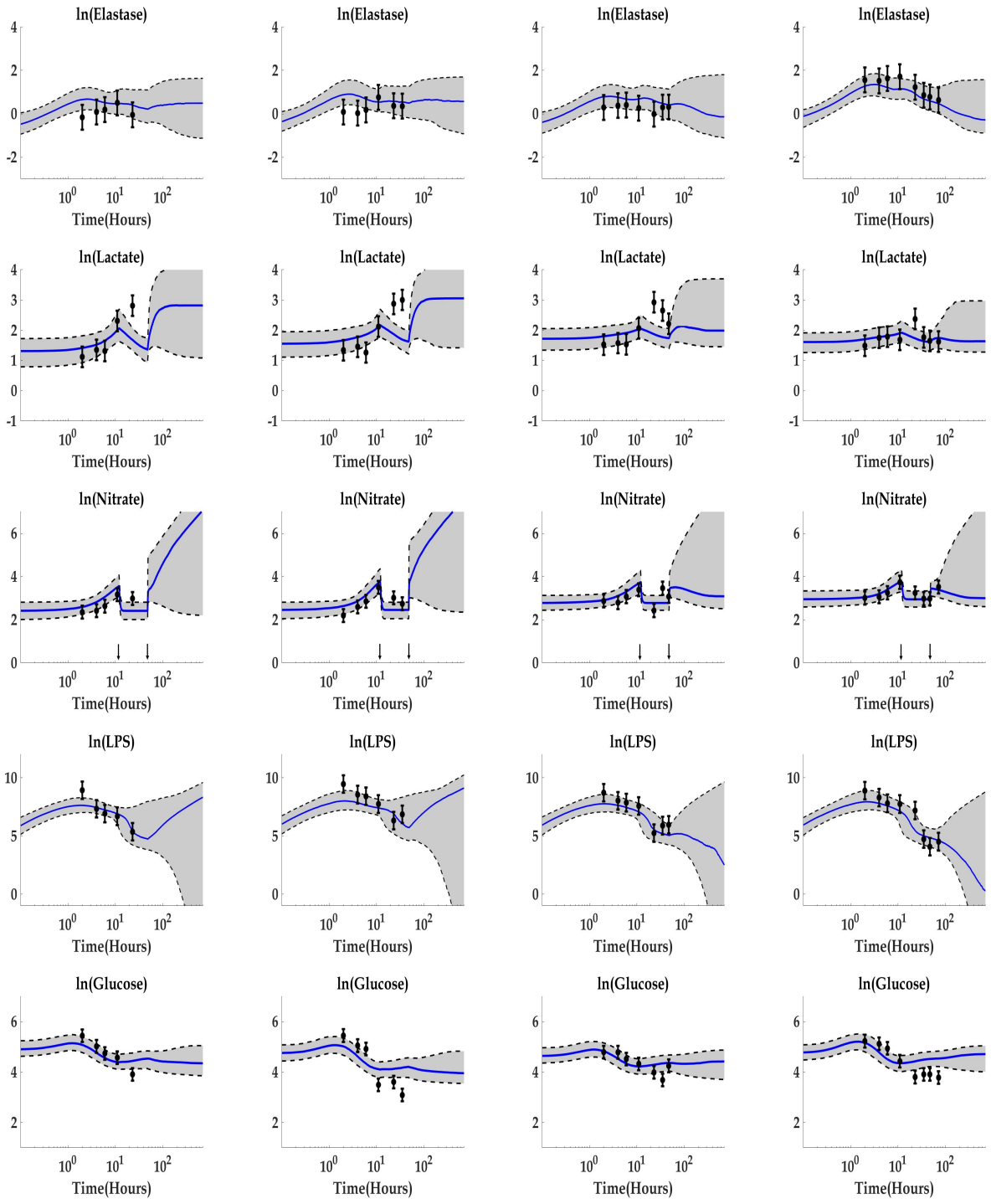

Figure 39: Envelopes of model trajectories corresponding to posterior density for treated subjects (a) NS68, (b) NS71, (c) NS78, and (d) NS94 obtained with Metropolis with informative prior. Subjects were treated with an NOS inhibitor from 12 hours until 48 hours, indicated by arrows in the Nitrate panels.

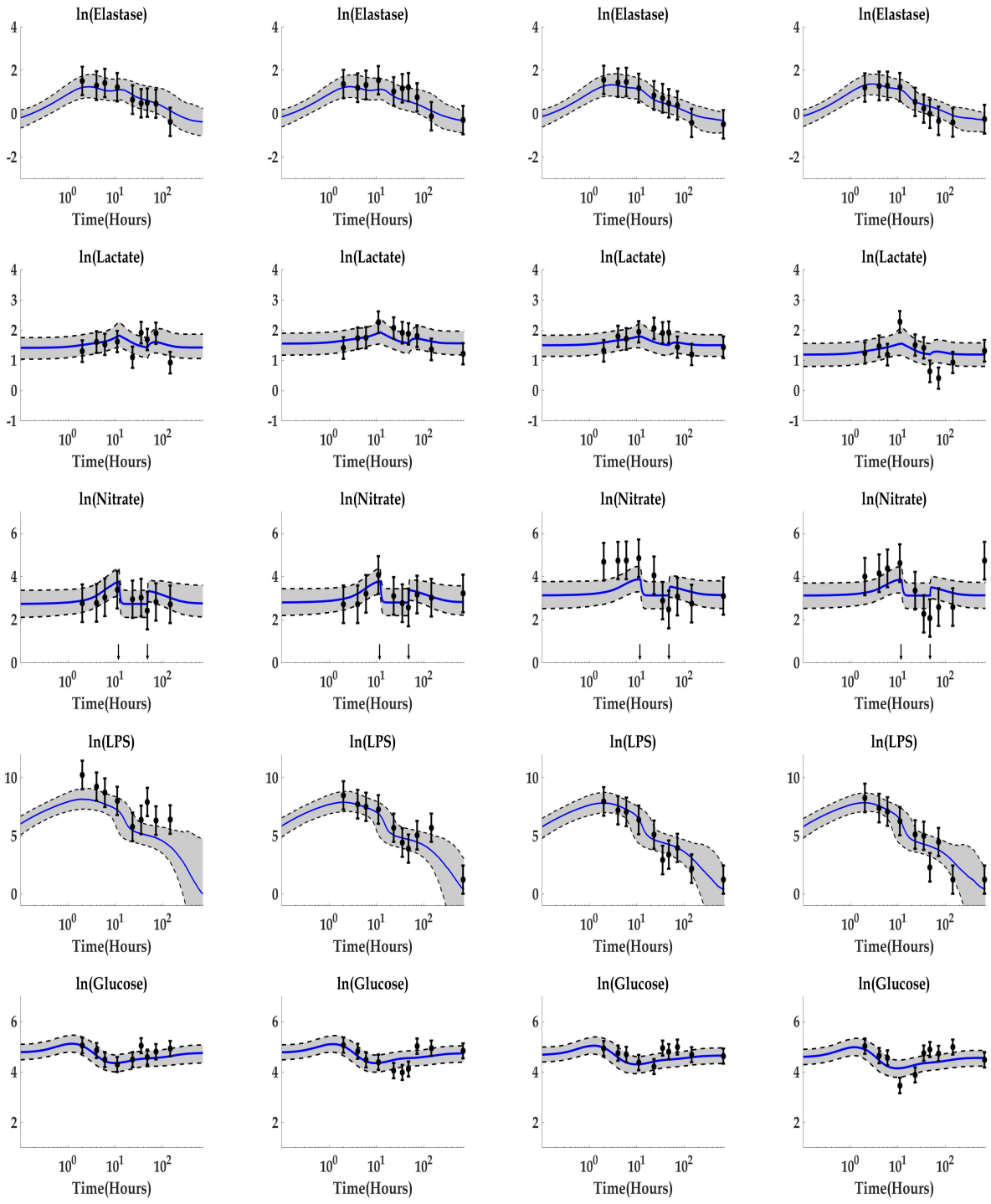

Figure 40: Envelopes of model trajectories corresponding to posterior density for treated subjects (a) S91, (b) S102, (c) S103, and (d) S106 obtained with Metropolis with informative prior. Subjects were treated with an NOS inhibitor from 12 hours until 48 hours, indicated by arrows in the Nitrate panels.

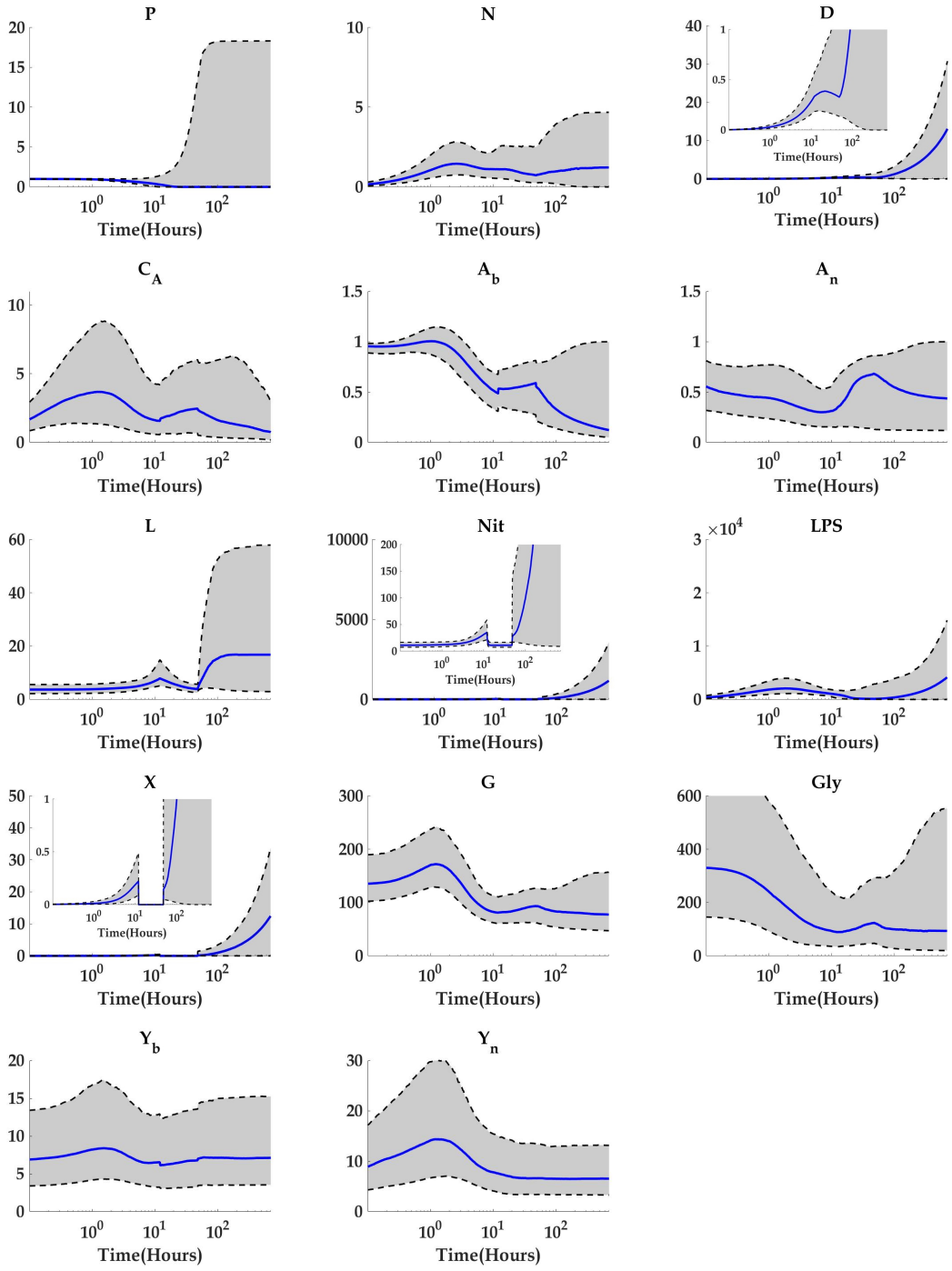

Figure 41: Predicted intervals of model trajectories obtained with metropolis fitting NS68. The solid red and blue lines correspond to the medians of the sampled trajectories and the shaded regions bounded by the dashed lines enclose the $5\% - 95\%$ confidence interval. Insets show a close-up of the effect of therapy in D, Nit, and X.

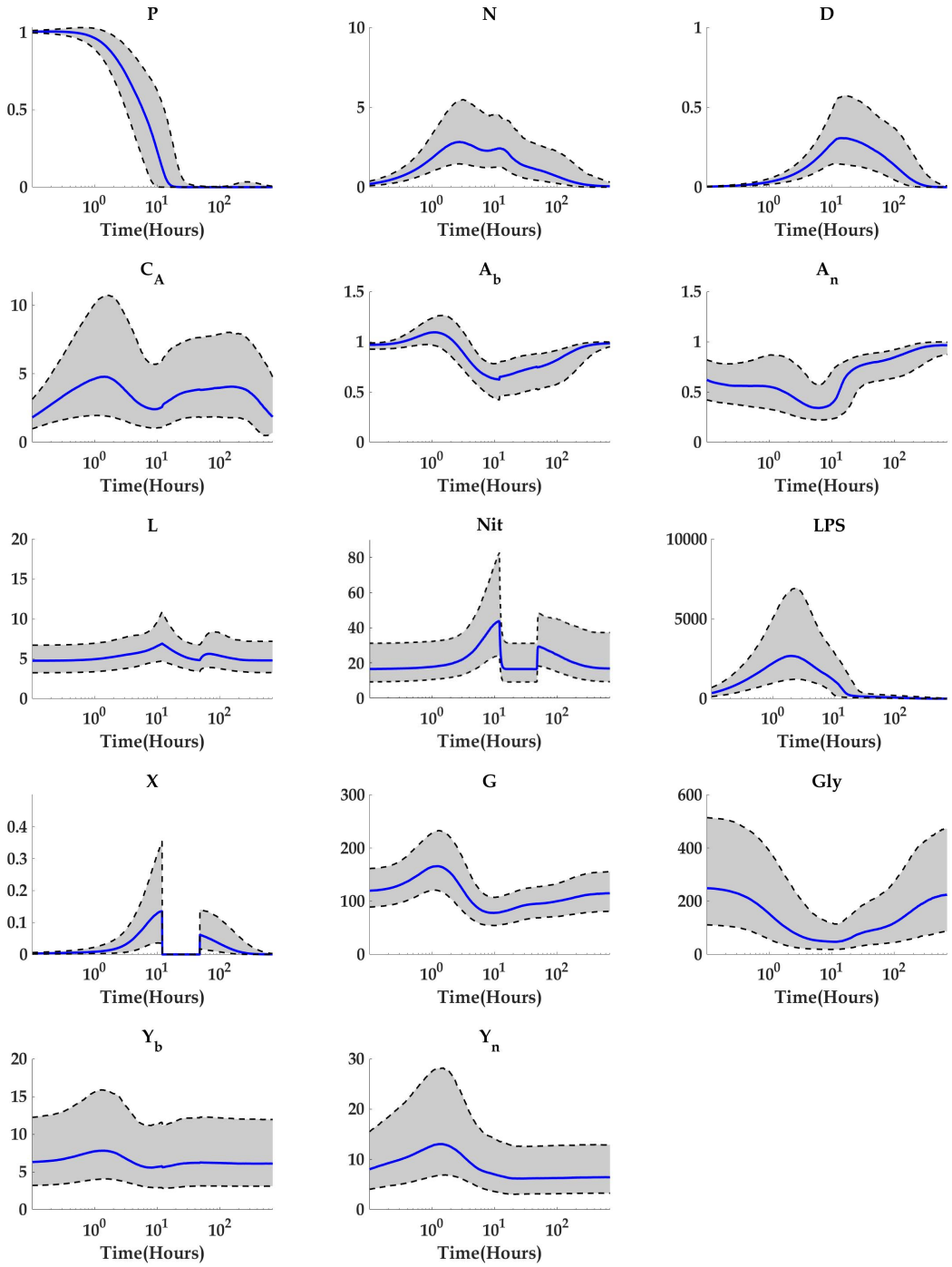

Figure 42: Predicted intervals of model trajectories obtained with metropolis fitting S102. The solid red and blue lines correspond to the medians of the sampled trajectories and the shaded regions bounded by the dashed lines enclose the $5\% - 95\%$ confidence interval.

5.3.3 Alternative scenarios of treatment induction

According to the authors in [62], several considerations were made to decide the therapy protocol implemented in their study. For instance, they first measured mean arterial blood pressure (MAP) in a pilot group of animals. They observed MAP started to decline between 12-18 h. Second, they also studied induction of increased NOS activity by looking at nitrite/nitrate measurements and found increased NOS activity after 4 hours, with an increase nitrate levels at 8 and 24 hours. Based on these observations, they decided to start infusion of the NOS inhibitor at 12 hours. Starting therapy at this time has also clinical reasons, as sepsis diagnosis and therefore therapy usually occurs several hours after pathogen invasion.

Table 14: Alternative therapy protocols

Therapy Interval	Health (±35)	Aseptic (±34)	Septic (±25)	Total	Prob. Surv.
$[12, 48]$	2281	2017	698	4996	45.66
$[2, 38]$	2824	1459	713	4996	56.53
$[8, 44]$	2671	1638	685	4994	53.48
$[10, 46]$	2476	1832	685	4993	49.59
$[12, 40]$	2189	2129	679	4997	43.81
$[12, 50]$	2346	1906	745	4997	46.95
$[12, 60]$	2479	1757	760	4996	49.62
$[12, 80]$	2821	1460	715	4996	56.47
$[14, 50]$	2152	2128	718	4998	43.06
$[14, 60]$	2260	2039	688	4987	45.32
$[16, 52]$	1989	2310	695	4994	39.83

We use our model to explore other possible scenarios including, earlier and later therapy infusion with 36 hours duration, and shorter and longer therapy duration. We applied therapy (with $k_{th} = 1000$) to a subsample of X_{tot} which initially is distributed with 75% non-survivors and 25% survivors. We compare these scenarios with the baseline case when

therapy is administered as in the baboon study from 12 hours until 48 hours, shown in the first row of Table 14. We computed the standard deviations shown with the formula $\sqrt{np(1-p)}$, where n is the total number of subjects for each case and p is the probability of occurrence of health, asepsis, and sepsis. As all results were fairly similar, we took the average.

Our results suggest that early therapy infusion improves mortality outcome. In fact, starting therapy at 10 hours and during the same period of 36 hours, results in an increase in the probability of survival of 3.93%, as shown in the last column of Table 14. If therapy starts even earlier, at 8 hours after infection, probability of survival improves to 53%. However, starting therapy too early is unlikely as patients must be diagnosed first. In practice, NOS inhibitor therapy must be applied not earlier than increased NOS activity starts. However, our model does not account for this and it predicts higher survival when treatment starts as early as 2 hours after infection.

On the other hand, starting therapy at 14 hours decreases survival probability to 43.06%, even if treatment is administered during the same 36 hours period of time. If therapy is administered much later at 16 hours, probability of survival decreases to 39.83%, even if treatment is extended for the same duration of 36 hours. Lastly, we also observed that starting at 12 hours and administering therapy for only 34 hours instead of 36 hours, does not significantly change survival. Similarly, extending duration of therapy until 50 hours and starting at 12 hours, does not significantly improve survival. However, our model suggest that further increasing therapy duration improves survival. In fact, therapy needs to be applied from 12 to 60 hours to increase survival to 49.62% and up to 80 hours for a survival probability of 56.47%.

It is clear from Table 14 that with early therapy intervention we should expect a positive effect on aseptic patients. However, sepsis does not seem to be highly affected by therapy. Work still needs to be done to explore further therapeutic routines. For instance, optimal control techniques can be applied to find best treatment strategies that can include intervals of therapy application while minimizing potential side effects.

5.4 Logistic regression: identifying outcome from patient characteristics

5.4.1 Preliminaries

Logistic regression is a statistical tool similar to linear regression that is commonly used to describe the relation between one binary or dichotomous variable Y and one or more independent variables or predictors $X_1, X_2, \cdots, X_k$. The dependent variable is dichotomous, because it only assumes binary values, such as 0 or 1, male-female, pass-fail, etc. Logistic regression is commonly used in the medical scientific community to evaluate risk factors in patient outcome [65], [20], [78]. Seymour et al. used logistic regression to relate patient characteristics to outcomes, and thus estimate the probability of a patient dying of sepsis, [65].

Mathematically, logistic regression models how the binary variable Y depends on the predictor or explanatory variables by the relation

$$\ln\left(\frac{p}{1-p}\right) = b_0 + b_1 X_1 + \cdots + b_k X_k \tag{58}$$

The distribution of Y is assumed to be binomial and p is the probability of success, i.e. $p = P(Y = 1)$. The left hand side of equation (58) is called the logit function which models the dependent variable by a linear combination of independent variables, and it corresponds to the log of the odds of an event occurring. The coefficients $b_0, b_1, \cdots, b_k$ are selected in such a way that maximize the likelihood of predicting with high probability for observations belonging to one class, say 1, and low probability for observations belonging to the other class, say 0. This process is called maximum likelihood estimation, and is used in logistic regression to identify the strongest linear combination of independent variables that increases the likelihood of detecting the observed outcome.

It is important to understand the difference between odds and probability. The odds correspond to the ratio of the probability that an event occurs over the probability that the event does not occur. In symbols, the odds of an event occurring with probability p is given by:

$$\text{Odds} = \left(\frac{p}{1-p}\right) \tag{59}$$

For example, if the probability of an event happening is 0.75, then odds of the event occurring is $0.75/0.25 = 3$. In other words, the event will occur 3 times for every time the event does not occur.

Combining equations (59) and (58), we obtain a formula for the odds that an event occurs depending on the predictor variables and their coefficients:

$$\text{Odds} = e^{b_0+b_1X_1+\cdots+b_kX_k} \tag{60}$$

Using equations (59) and (60) we also obtain a formula for the probability of the event occurring, also known as the logistic function:

$$p = \frac{1}{1+e^{-(b_0+b_1X_1+\cdots+b_kX_k)}} \tag{61}$$

To illustrate how to interpret the resulting coefficients $b_0, b_1, \cdots, b_k$ given in the logistic regression, we consider the following example. Suppose we are modeling a binary dependent variable that takes either the values diabetes or healthy. Suppose that $p = P(Y = 1)$ is the probability of a patient becoming diabetic. And that we have several predictor variables $X_1, \cdots, X_k$. In particular, we want to determine whether or not increasing one of the predictor variables, say X_1 =glucose, by one unit has any influence in the outcome of the dependent variable. Suppose that for this variable we obtained the coefficient $b_1 = 1.6$. Then the odds of a patient becoming diabetic given that glucose=g is

$$\ln\left(\text{Odds}_{\text{diabetes}|glucose=g}\right) = b_0 + (1.6)g + \cdots + b_kX_k \tag{62}$$

Similarly, the odds of a patient becoming diabetic given that glucose increases by one unit is

$$\ln\left(\text{Odds}_{\text{diabetes}|glucose=g+1}\right) = b_0 + (1.6)(g+1) + \cdots + b_kX_k \tag{63}$$

Subtracting the two previous equations we obtain

$$\ln\left(\text{Odds}_{\text{diabetes}|glucose=g+1}\right) - \ln\left(\text{Odds}_{\text{diabetes}|glucose=g}\right) = 1.6 \tag{64}$$

And finally, exponentiation gives us the odds ratio (OR):

$$\frac{\left(\text{Odds}_{\text{diabetes}|glucose=g+1}\right)}{\left(\text{Odds}_{\text{diabetes}|glucose=g}\right)} = e^{1.6} = 4.953 \tag{65}$$

In other words the OR corresponds to the exponential of the regression coefficient e^{b_j}. In our example, the OR tells us that by holding fixed all the other predictor variables and increasing glucose by one unit, the odds of becoming diabetic increase by about 395.3%.

In this section we use logistic regression to determine which parameters have an influence in the model output. In particular, we will consider three different scenarios (see Fig. 43):

1. When the total virtual population is classified into either survivors or non-survivors.
2. When the non-survivor virtual population is classified into either septic or aseptic.
3. When the non-survivors that undergo treatment is classified into either survivors or non-survivors.

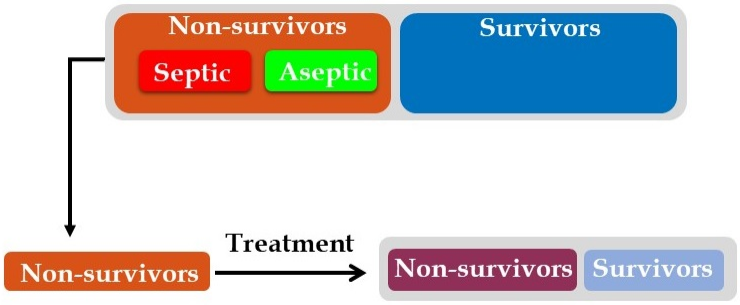

Figure 43: Diagram of three different scenarios studied with logistic regression.

5.4.2 Logistic regression on survivors and non-survivors non-treated

In this section, we consider a random sub-sample of X_{tot}. Every subject from this sample can either be a survivor or a non-survivor depending on the model output. Survivors are those subjects whose model trajectories converge to the healthy steady state. Whereas non-survivors are those subjects whose model trajectories are either septic or aseptic. Each virtual subject in this population consists of 55 parameters, that when plugged into our model have associated either a survivor or a non-survivor trajectory. Our goal here is to determine which parameters out of the 55 can be considered as patient outcome predictors.

As this sub-sample contains parameters with different orders of magnitude, we standardize it by subtracting the mean and dividing by the standard deviation. We will do this same step in all three cases where we used logistic regression in the following sections. We let p be the probability that a subject will survive, i.e. $p = P(\text{Survives} = 1)$ and use the Classification Learner App in Matlab 2020a to run a logistic regression model with 55 predictor parameters and 5-fold cross validation to avoid over-fitting. With the 55 predictor parameters, the model has a classification accuracy of 93.1%. Interestingly enough, reducing the number of predictor parameters to 12 does not significantly lower the accuracy, as the accuracy of classification in this case is 86.5%. The choice of these 12 parameters was based on a threshold of 1 in the magnitude of their corresponding estimated coefficients given in the logistic regression with 55 variables.

Higher estimates have higher contribution to predict patient outcome. All of these 12 parameters had a p-value well below 0.05 but their standard error were relatively high due to the large number of variables used. We run logistic regression again but this time only considering these 12 parameters as possible predictor variables. Their corresponding p-values were again below 0.05 indicating that they are still statistically significant. Moreover, all their corresponding tstat values are above 2 in magnitude confirming they are statistically significant, according to the Wald test. A summary of the results from logistic regression including coefficient estimates, tstats, odds ratios, and 95% confidence intervals are shown in Table 15.

Table 15: Logistic regression summary for non-treated subjects when classifying subjects between survivors and non-survivors

Variable	Coefficient	tstat	Odds	95% CI Odds	% of change
(Intercept)	-0.250	-15.110	0.779	(0.754, 0.804)	-22.114
c_2	-1.762	-74.541	0.172	(0.163 , 0.179)	-82.835
α_x	-1.014	-56.727	0.363	(0.350 , 0.375)	-63.714
k_{nod}	-0.911	-49.741	0.402	(0.387, 0.416)	-59.805
k_{dn}	-0.799	-42.695	0.450	(0.433 , 0.466)	-55.033
c_3	-0.752	-43.425	0.471	(0.455 , 0.487)	-52.862
k_{pg}	-0.736	-38.960	0.479	(0.461, 0.497)	-52.089
μ_{gly}	-0.639	-36.665	0.528	(0.510 , 0.546)	-47.196
k_A	-0.622	-34.951	0.537	(0.518 , 0.555)	-46.314
μ_{no}	0.582	33.178	1.790	(1.729, 1.853)	79.039
k_{pn}	0.639	36.234	1.895	(1.830 , 1.961)	89.475
x_{dn}	1.366	68.548	3.919	(3.769, 4.075)	291.906
μ_A	2.768	92.037	15.934	(15.021 , 16.901)	1493.413

The confusion matrix shown in Fig. 44a, summarizes the accuracy of the logistic regression algorithm in predicting surviving versus non surviving with the 12 parameters mentioned above. In the main diagonal (colored in blue) we observe the True Positives (TP) and the True Negatives (TN), respectively. 85.5% are TP which corresponds to the percentage of subjects that did not survive and were correctly classified by the algorithm as non-survivors. On the other hand, 87.5% are TN which corresponds to the percentage of subjects that survived and were correctly identified by the algorithm as survivors. In the anti-diagonal (colored in red), we observe the False Positive (FP) and False Negative (FN) groups. In the FP, 12.5% corresponds to the percentage of subjects that survive but were incorrectly classified by the algorithm as non-survivors. Whereas 14.5% is the percentage of FN, which corresponds those

Table 16: Standard deviation of significant parameters when classifying non-treated subjects between survivors and non-survivors

Parameter	STD	Parameter	STD
c_2	43.279	μ_{gly}	0.3306
α_x	0.52665	k_A	0.0014045
k_{nod}	5894.4	μ_{no}	4172.9
k_{dn}	0.012103	k_{pn}	2.9452
c_3	0.86863	x_{dn}	0.10641
k_{pg}	0.047989	μ_A	5.8403

subjects that did not survive but were incorrectly classified by the algorithm as survivors.

As shown in Fig. 44b, the discrimination of these 12 predictor variables for survival as expressed by the receiver operating characteristic area under curve (ROC) was 0.94. The ROC gives the rate of successful classification by the logistic model. The higher the AUC the better the algorithm is at predicting survivors and non-survivors. The AUC is determined by the threshold of classification given by having a false positive rate of 0.13 and a true positive rate of 0.85. This threshold was automatically chosen by the classification learner algorithm.

Although many biological processes are condensed into the dynamics of our model, from our results we learned that some energy related processes have an important role in determining patient outcome. Its large estimate coefficient indicates that μ_A is the parameter that better predicts outcome between survivors and non-survivors. In fact, holding all other parameters fixed and increasing one standardized unit of μ_A results in an increase in the odds of surviving by 1493.4%, where one standardized unit of μ_A is 5.8403 units. The standard deviations of all 12 parameters are shown in Table 16.

As we pointed out in Section 3.5, μ_A is the energy rate constant. The exact role it plays

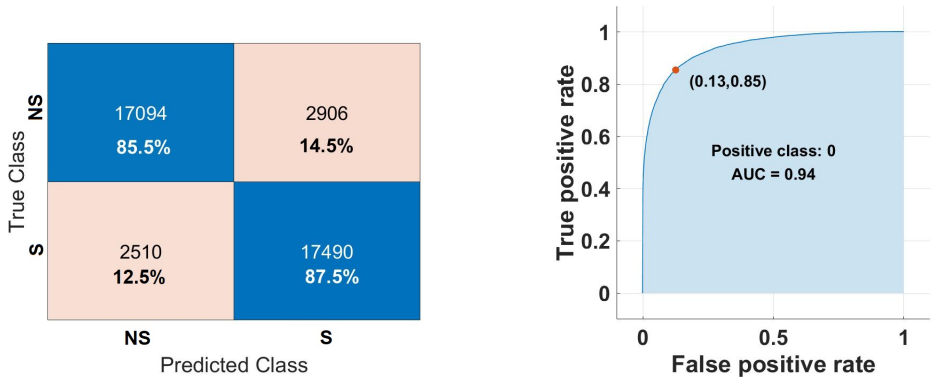

(a) (b)

Figure 44: (a) The confusion matrix contains information about actual and predicted classifications between survivors and non-survivors non-treated. (b) The ROC and AUC curve for the classification between survivors and non-survivors non-treated. The red point indicates the true positive rate and true positive rate used in the classification. The area under the curve AUC provides a sense of the degree or measure of separability of the model. The higher the AUC, the better is the model in classifying survivors and non-survivors.

in the dynamics of our model is not straight forward as μ_A is also involved in the production and depletion of both ATPs, as it was noted in equations (28) and (29).

The high estimates for parameters k_{pn}, and c_2 indicate that phagocytosis and the energy required for this process to take place are also part of the parameters with higher contribution to predict patient outcome. Although its odds ratio suggests that an increase of one standardized unit of k_{pn} represents an increment of 89.4% in the odds of surviving, the quartile plots indicate that survival is better attained when it lies within the second and third quartile. Quartile plots for the 12 most significant parameters are shown in Fig. 45. On the other hand increasing c_2 has a negative effect in survival. In fact, there is an 82.8% reduction in the odds of survival per increment of one standardized unit of c_2. This says that if all other parameters were to be kept fixed and there is a increment in the energy consumed in pathogen elimination through phagocytosis, we should expect a reduction in the odds of

surviving. This negative effect is even more significant for higher values of c_2, as detailed in Fig. 45.

Tissue damage marker is also an important predictor, mostly determined by its half saturation value x_{dn}. In fact, this parameter ranks second in terms of odds ratios. In the quartile plots, we observed that the higher this half saturation can get, the better the percentage of survival. In fact, 67% of the subjects whose x_{dn} value lies in the fourth quartile survive. Another tissue damage related parameter that was highlighted in the logistic regression results was α_x. This parameter however, does not have an intrinsic biological meaning as it is used as a scaling parameter to balance the number of pathogens and molecules of nitric oxide. However we interpret that the higher its value, the more impact nitric oxide has on tissue damage production, which is consistent to the higher percentage on non-survivors when α_x lies over the third and fourth quartiles shown in Fig. 45.

The odds ratio column shown in Table 15 shows the effect that each parameter contributes to survival when all the other parameters are held fixed. On the other hand, the quartile plots indicate the survival percentage for a portion of the ensemble with a specified range of each parameter, without holding any restrictions on the other parameters. Lastly, the parameter densities shown in Fig. 46 provide a measure of the frequency of each parameter value taken by members of the ensemble.

Finally, it is important to note that although the quartile plots indicate that higher kpg is associated to higher survival probability, it is unclear what is the combination with the other parameters that will lead to such higher probabilities to explain this counter intuitive behaviour. However, in Fig. 47d we note that for survivors it is more likely to observe higher values of μ_A. This suggest that if we observe a patient whose pathogen load growth is high, we would recommend to increase the energy rate to improve chances of survival. This does not occur within the non-survivor population as we can see in Fig. 47a, where these two parameters are positively correlated.

Overall parameters are not highly correlated. The only pair correlation higher than 0.5 was between s_g and k_A in the survivor population where they are positively correlated with a correlation coefficient of 0.58. A scatter plot of these two parameters is shown in Fig. 47f. Additionally in Fig. 47 we also present pair scatter plots of μ_A vs k_{pg} and μ_A vs x_{dn}

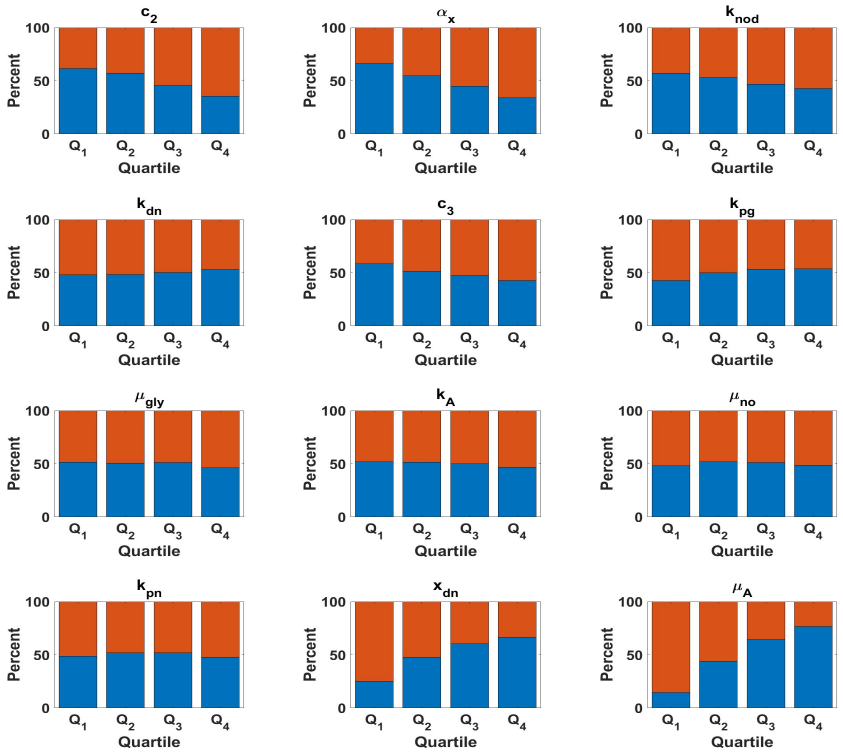

Figure 45: Quartiles of most contributing parameters when non-treated subjects are classified between non-survivors and survivors. Survivors are colored in blue whereas non-survivors are colored in orange.

within the non-survivor group in (a) and (b), respectively. Similarly, scatter plots of these parameters within the survivor cohort are also shown in (d) and (e), respectively. These parameters were shown to be relevant to decide patient outcome in the logistic regression results.

5.4.2.1 Envelopes for non-survivors and survivors The envelopes of the two distributions of survivors and non-survivors are depicted in Fig. 48. There is a clear distinction between survivors and non-survivors in the ATP trajectories that is more evident after the first few hours. During the first 3 hours both A_b and A_n have similar transient behavior. However, there is a rebound in both survivor ATPs that starts at about 4 hours after in-

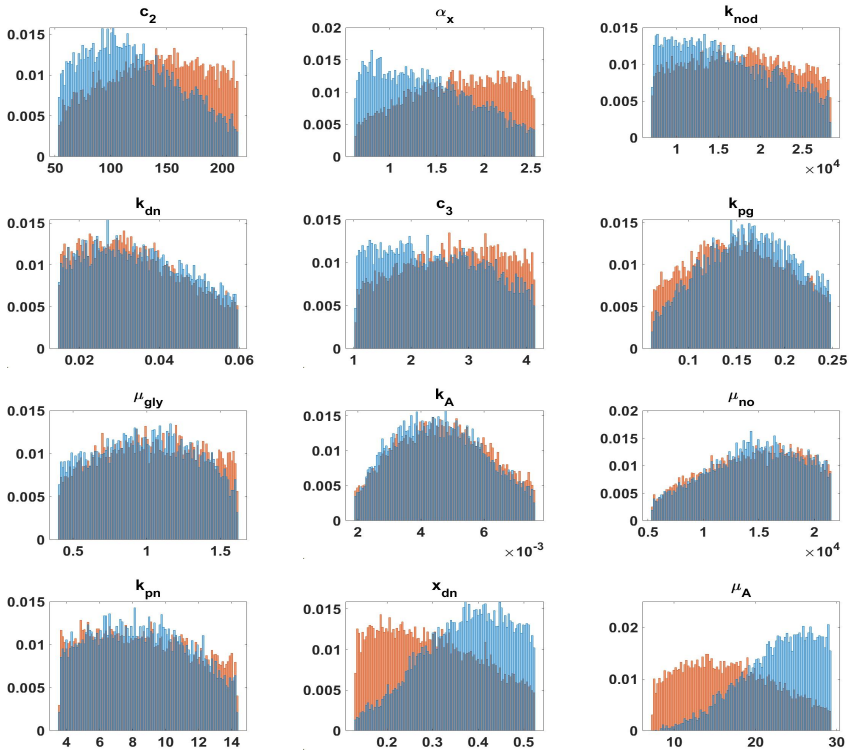

Figure 46: Densities of most contributing parameters when non-treated subjects are classified between non-survivors and survivors. Survivors are colored in blue whereas non-survivors are colored in orange.

duction of infection. A similar rebound is observed in non-survivor A_n at a later time at about 11 hours. This rebound is however not strong enough and it soon stabilizes to a low energy steady state. This difference in energy between the two populations is in part a result of different glucose levels, where survivors have an overall higher glucose level compared to non-survivors.

Although more phagocyte activity is present during the first 10 hours in the survivor trajectories, the fact that enough ATP is available for survivors during this initial period of time, fuels their anti-inflammatory response C_A to make it more efficient in maintaining a balance in the inflammation process. These elevated levels on anti-inflammatory mediators regulate inflammatory markers including nitric oxide and lactate. Also, the higher levels of

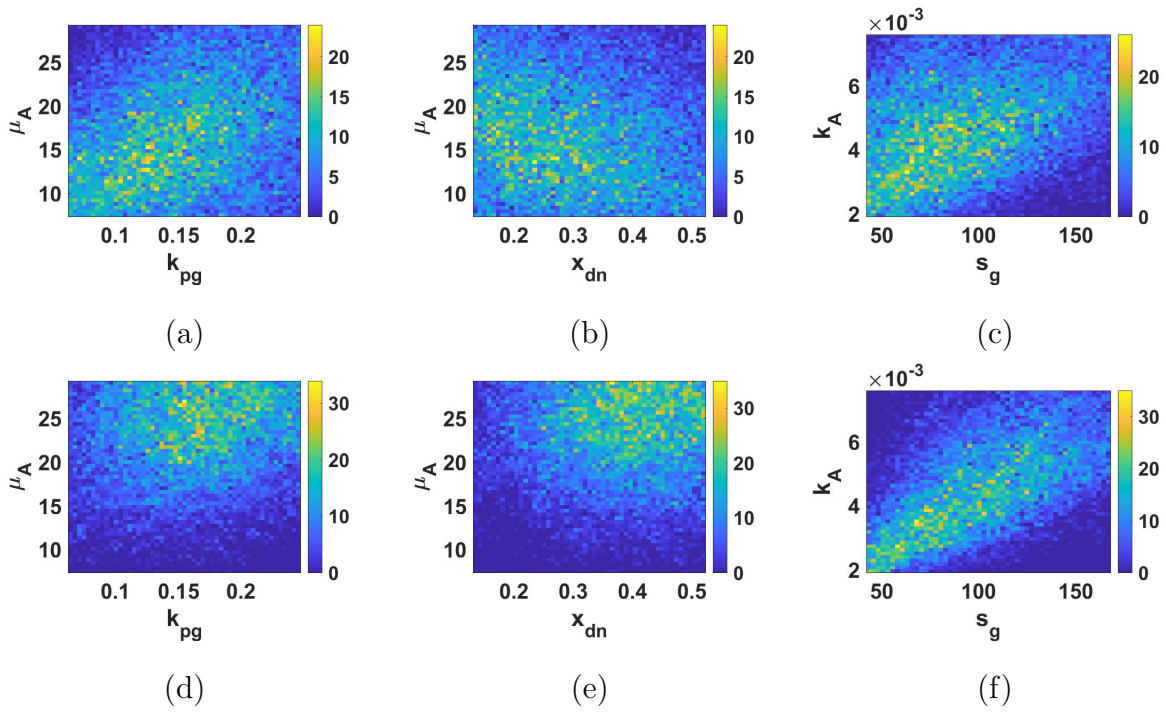

Figure 47: Pair correlations of some parameters in the survivors and non-survivors cohorts. (a) μ_A vs k_{pg} in non-survivors, (b) μ_A vs x_{dn} in non-survivors, (c) s_g vs k_A in non-survivors, (d) μ_A vs k_{pg} in survivors, (e) μ_A vs x_{dn} in survivors, and (f) s_g vs k_A in survivors.

A_b in survivors rapidly takes care of tissue damage as it can be observed in the bifurcation occurring at about 5 hours between the two D trajectories. The same bifurcation occurs at different times also in the L, LPS, X, and Gly trajectories. In lactate this bifurcation suggests a shift on energy metabolism from aerobic to anaerobic respiration in non-survivors. This shift is partial as some ATP is still produced through phosphorylation.

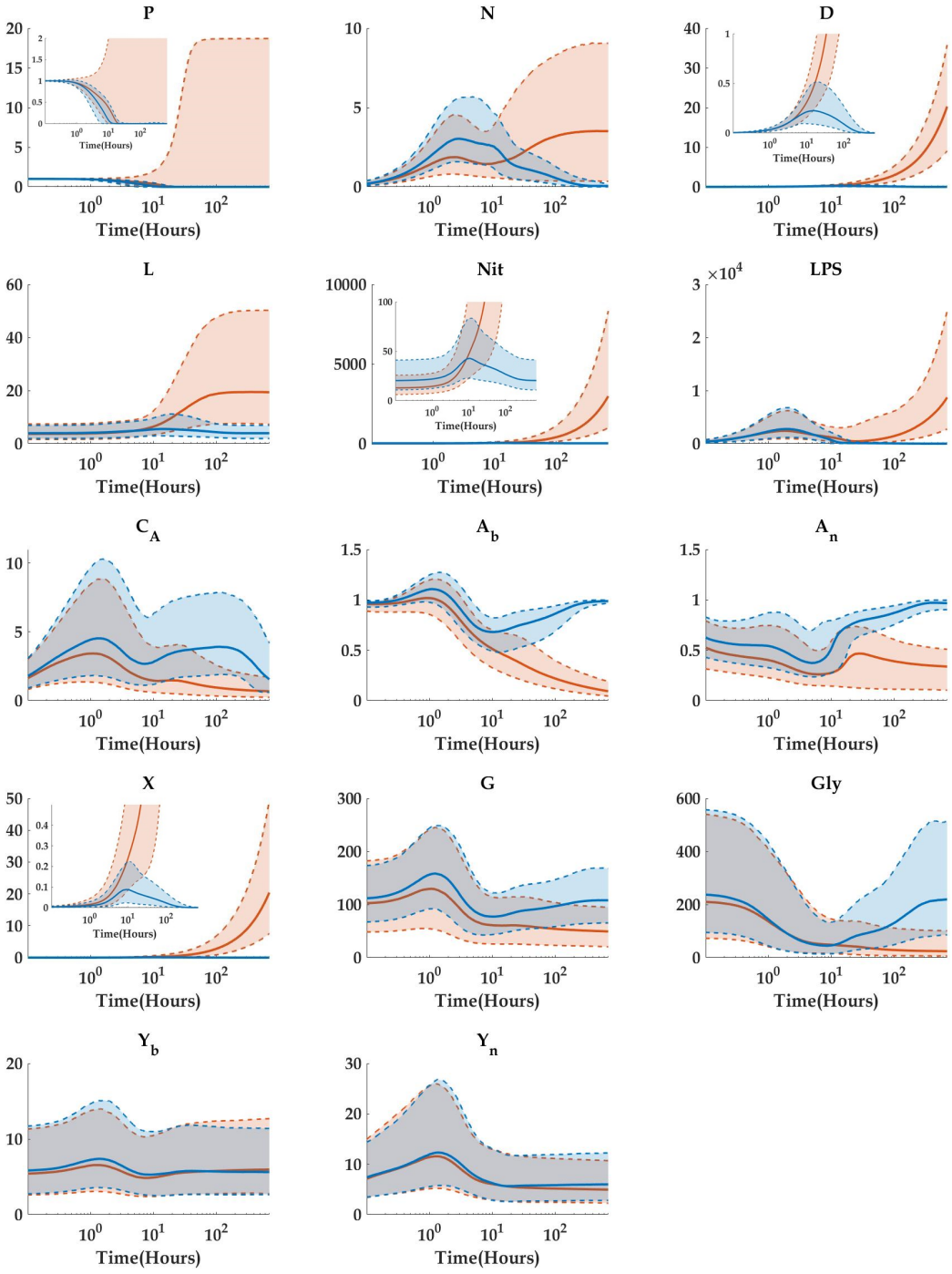

Figure 48: Predicted intervals of model trajectories obtained with parameters from a survivors and non-survivors distributions from non-survivors non-treated distribution. Non-survivors envelopes are colored in orange whereas survivors envelopes are blue. The solid red and blue lines correspond to the medians of the sampled trajectories and the shaded regions bounded by the dashed lines enclose the $5\% - 95\%$ confidence interval.

5.4.3 Logistic regression on non-survivors non-treated: septic and aseptic

As we have already discussed earlier, our virtual population of non-survivors non-treated can be separated into either septic or aseptic individuals. However, it is unclear what specific mechanisms differentiate one group from the other. This is once again a perfect opportunity to use logistic regression to model patient outcome from patient characteristics. We begin by randomly selecting from X_{tot} column vectors to form a sub matrix X_{nsnt} of size 55×20000, where $nsnt$ stands for non-survivors non-treated. We then use our extended model to classify virtual subjects into either septic or aseptic. As a result, we obtain that 3928 (19.64%) are classified as septic and 16072 (80.36%) are aseptic. Because this is again a binary classification, we extend X_{nsnt} by one extra column and assign 1 to septic subjects and 0 to aseptic. We standardize X_{nsnt} as we did in the previous section and use logistic regression initially with 55 features with 5-fold cross validation, to obtain 93.6% of accuracy. We then select the parameters whose coefficient estimate is larger in magnitude than 1 and obtained a classification accuracy of 89.9%. This is summarized in the confusion matrix shown in Fig. 49, where 95.9% aseptic were correctly classified while the other 4.1% where incorrectly classified as septic. Similarly, 64.8% of the septic subjects were correctly classified whereas the other 35.2% were incorrectly classified as aseptic. Moreover, the area under the curve ROC was 0.94.

As it can be observed in Table 18, both pathogen growth rate and energy rate, play a fundamental role in predicting outcome of patients between septic and aseptic. In fact, an increment of one standardized unit of k_{pg}, i.e. an increment of 0.0489 units in the rate of pathogen growth, results in an increment in the odds of becoming septic by 1160%. Table 17 contains the standard deviations of the 5 selected parameters.

We observe in Fig. 51 that septic patients are more likely to have higher k_{pg} values than aseptic patients. This is consistent with the results found in Chapter 2. In fact, 38.52% of the non-survivor subjects whose k_{pg} lies within the fourth quartile are septic, while the other 61.48% are aseptic. In contrast, only 2.96% of the non-survivors whose k_{pg} lies within the first quartile is septic. We also observe that patients with lower μ_A have higher risk of becoming septic. In fact, for every time μ_A increases 5.6613 units, the odds of becoming

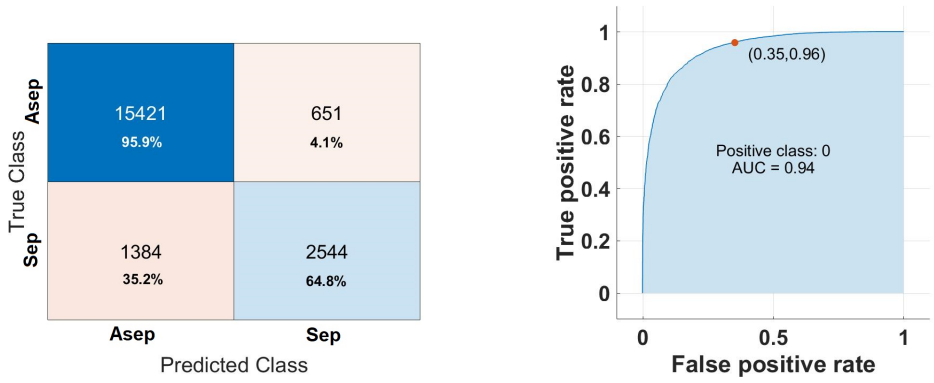

(a) (b)

Figure 49: (a) The confusion matrix contains information about actual and predicted classifications between non-survivors non-treated septic and aseptic. (b) The ROC and AUC curve for the classification between non-survivors non-treated septic and aseptic. The red point indicates the true positive rate and true positive rate used in the classification. The area under the curve AUC provides a sense of the degree or measure of separability of the model. The higher the AUC, the better is the model in classifying non-survivors between septic and aseptic.

septic decrease by 90.561%.

We note that here the two groups under consideration are non-survivors and therefore, as we mentioned in the previous section, it is expected that μ_A tends to be on the lower side for both groups. However, as seen in Fig. 52, septic patients are more likely to have smaller μ_A compared to aseptic subjects. Also, according to the quartile plots, 34.58% of the subjects whose μ_A lies in the first quartile are septic, while only 8.66% of the subjects whose μ_A lies within the fourth quartile are septic.

Parameter c_2 is the proportionality rate of the phagocytosis energy flux. And our results suggest that the more energy is spent during this process, the higher the risk of sepsis. In fact, holding all variables fixed, for every time c_2 increases one standardized unit, i.e. 43.363 units, there is 447.278% increase in the odds of becoming septic. Similar conclusions can be

made from the estimates of μ_m and k_{pm}, which are involved in the elimination of pathogens through non-specific means.

Again parameters are not highly correlated across the two populations. However as a matter of comparison we also show the pair scatter plot of k_{pg} vs μ_A for septic in Fig. 50a and for the aseptic population in Fig. 50b. Although not at a high value k_{pg} vs μ_A are positively correlated in the aseptic group with a correlation factor of 0.36.

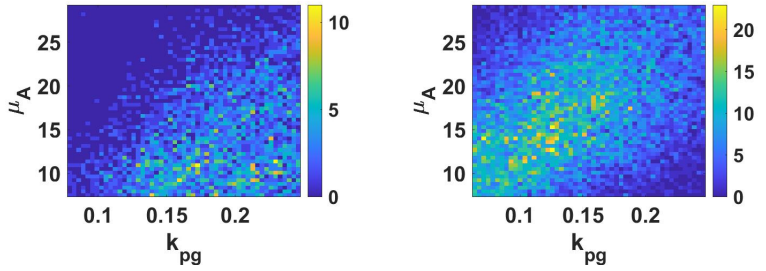

(a) (b)

Figure 50: Pair correlations septic and aseptic. (a) μ_A vs k_{pg} in the septic population, (b) μ_A vs k_{pg} in the aseptic population.

Table 17: Standard deviation of parameters in septic versus aseptic within non-treated non-survivors

Parameters	STD
μ_A	5.6613
k_{pm}	0.0003
μ_m	0.0012
c_2	43.363
k_{pg}	0.0489

Table 18: Logistic regression summary for non-survivors after treatment that are classified between septic and aseptic

Variable	Coefficient	tstat	Odds	95% CI Odds	% of Change
(Intercept)	-2.920	-67.007	0.054	(0.049, 0.058)	-94.605
μ_A	-2.360	-52.890	0.094	(0.086, 0.103)	-90.561
k_{pm}	-1.094	-36.365	0.335	(0.315 , 0.355)	-66.501
μ_m	0.985	33.412	2.677	(2.526, 2.836)	167.716
c_2	1.700	45.924	5.473	(5.089 , 5.884)	447.278
k_{pg}	2.534	55.998	12.607	(11.537, 13.777)	1160.712

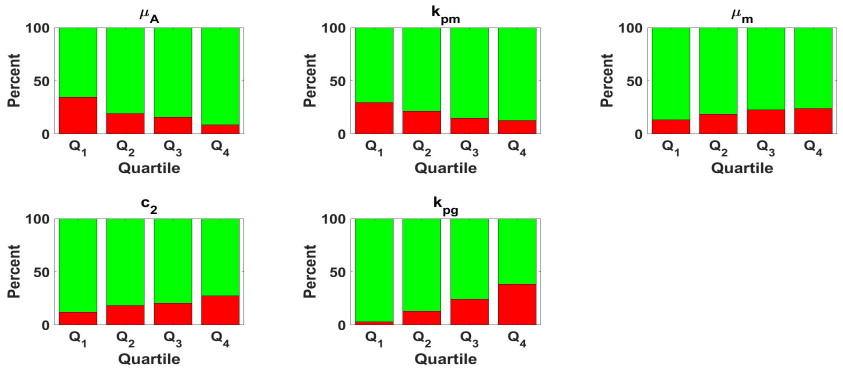

Figure 51: Quartiles of most contributing parameters for non-survivors non-treated when classified between septic and aseptic. Septic are colored in red whereas aseptic are colored in green.

5.4.3.1 Envelopes for septic and aseptic As the two groups here are non-survivors their envelopes are fairly similar in most of the trajectories. By definition the P envelopes in aseptic are converging to baseline levels while in sepsis P saturates at its carrying capacity. Inflammatory variables such as tissue damage, nitric oxide, and lactate are basically the same

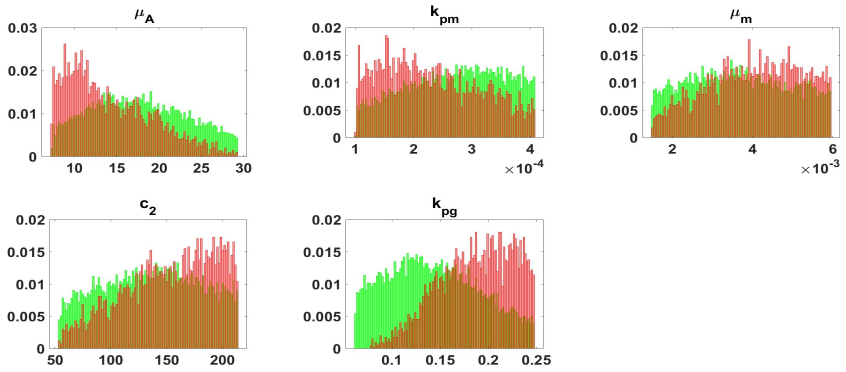

Figure 52: Densities densities of most contributing parameters for non-survivors non-treated when classified between septic and aseptic. Septic are colored in red whereas aseptic are colored in green.

across the two groups. However important differences are observed in the A_n trajectories, indicating that this form of ATP could be determinant for separating septic from aseptic. We note an early A_n recovery in the aseptic group starting at about 3 hours. This rebound continues up until 12 hours, and even though it levels down again, it converges to a much higher value than for those in the septic cohort. This difference in A_n is also clear on the way phagocytes fight the infection, as there is a much higher response in phagocytic activity in the aseptic group. This phagocytic activity is controlled by an also higher anti-inflammatory response, which is even more stronger in aseptic after the first hour and continues until the end of the simulation. Having this higher C_A response in aseptic, allows them to at the very least take care of the infection, by eliminating pathogens out of the system within the first two hours. However, the anti-inflammatory response fails to control the other inflammatory markers, hence the high inflammation and tissue damage lead to the eventual death of the aseptic population.

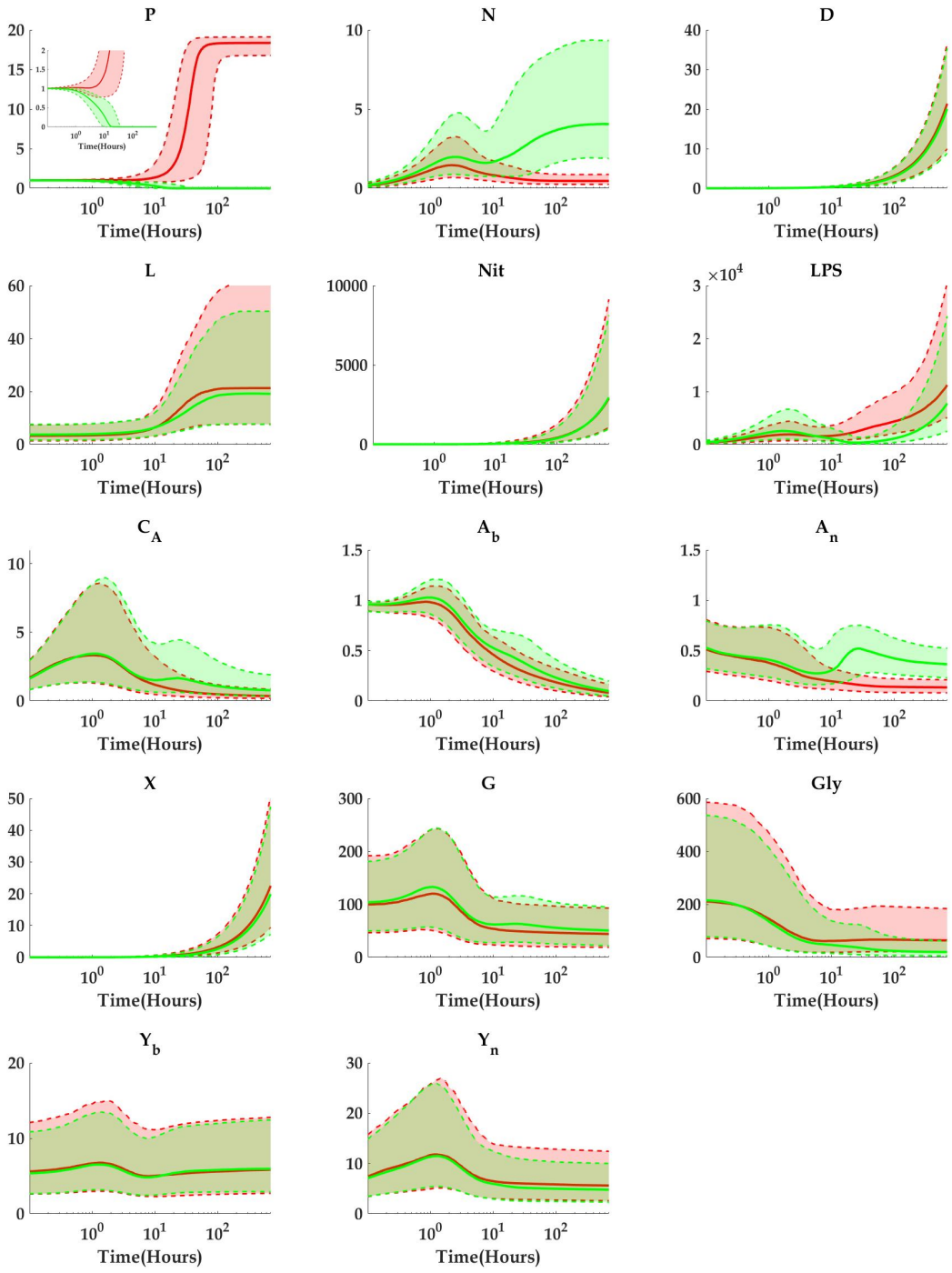

Figure 53: Predicted intervals of model trajectories obtained with parameters from a septic and aseptic distributions from non-survivors non-treated distribution. Septic envelopes are colored red whereas aseptic envelopes are green. The solid red and green lines correspond to the medians of the sampled trajectories and the shaded regions bounded by the dashed lines enclose the $5\% - 95\%$ confidence interval.

5.4.4 Logistic regression on non-survivors with therapy

We are interested in determining parameters that can be used to predict patient outcome. In particular, in this section our goal is to identify key parameters that can predict patient outcome when therapy is administered. We start by taking a random sub-sample of non-survivors from the total distribution X_{tot}. We introduce therapy to this sub-sample the same way it was described in Section 5.3.1. As patient outcomes are binary - either survivor or survivor- we assign 1 to survivors and assign 0 to those that do not survive; we then use a logistic regression model to determine the parameters that better predict a patient's outcome after treatment is administered.

As different parameters have different orders of magnitude, we standardize the sub-sample parameter matrix by subtracting the mean and dividing by the standard deviation, so that every parameter would have zero mean and standard deviation one. Using the Classification Learner App in Matlab 2020a with all 55 parameters as predictor variables and with a 5-fold cross validation to prevent over fitting, we obtain 83.1% of accuracy. That is, 83.1% of the total number of subjects were correctly classified by the logistic regression model.

Many of the resulting estimate coefficients had a p-value well below 0.05. But just some of them had a coefficient with relatively high magnitude compared to the rest. This could be due to the large amount of predictor variables that were used in the model. We observe that there are 19 parameters whose corresponding coefficients are larger in magnitude than a threshold of 0.4. These parameters also coincide with those with the smallest p-value, which indicates that they are statistically significant.

In order to reduce variability and therefore to obtain more accurate coefficient estimates, we run the logistic regression algorithm again but this time only using these selected 19 parameters. The accuracy of the model is still considerably high at 81.5% when using only these 19 parameters. The logistic regression results of the model along with these 19 predictors are summarized in Table 19. The tstat column corresponds to the coefficient estimate divided by its standard error and according to the Wald test, predictors whose tstat magnitude is larger than 2 indicate that they are statistically significant. This is consistent

to their corresponding low p-value (p-value< 0.05).

We obtained that the energy rate μ_A again plays a major role in predicting patient outcome in treated subjects. This can be seen by its large value of the coefficient estimate shown in Table 19. Its contribution is even more evident when looking at the percentage of change, which indicates that an increment of one standardized unit of μ_A, (i.e. 5.69 units), increases the odds of surviving by about 576.7%. Fig. 56 suggests that patients with larger μ_A, in particular within the fourth quartile, are more likely to survive after therapy. This is also seen in Fig. 55, which depicts the parameter densities of most contributing parameters.

Our results also suggest that treatment is more likely to reduce mortality in subjects whose pathogen growth rate lies within the first quartile Q_1, i.e. when k_{pg} is between 0.06 and 0.11. Also, the odds ratio of k_{pg} is 0.31, which indicates that the odds of surviving after therapy decrease by about 68.4% per increment of one standardized unit of k_{pg}. This means that an increment of k_{pg} by one standard deviation i.e., 0.049, results in a decrease on the odds of surviving by about 68.4%. The standard deviations of the most contributing parameters can be found in Table 20.

Overall parameters are not highly correlated across the two populations of survivors and non-survivors. However we show the pair scatter plot of k_{pg} vs μ_A for non-survivors in Fig. 54a and for the survivors population in Fig. 54b. Although not at a high value, k_{pg} vs μ_A are positively correlated in the survivor group with a correlation factor of 0.37 and in the non-survivor group with a correlation factor of 0.22.

As the intuition may suggest, the model reveals that patients whose tissue damage remains under control have better odds of surviving if treatment is administered. In particular, sustaining lower levels of tissue damage production, which is governed by k_{dn} and α_x, as well as higher half tissue damage accumulation x_{dn} can improve survival in treated patients. This is also illustrated on the quartiles plots shown in Fig. 56.

The confusion matrix shown in Fig. 57a, summarizes the accuracy of the logistic regression algorithm in predicting surviving versus non surviving with the 19 parameters mentioned above. We note that 89.8% of subjects that did not survive after treatment were correctly classified, whereas the other 10.2% were incorrectly classified as survivors. Similarly, 60.8% of survivors were correctly classified and the other 39.2% were incorrectly classified as non-

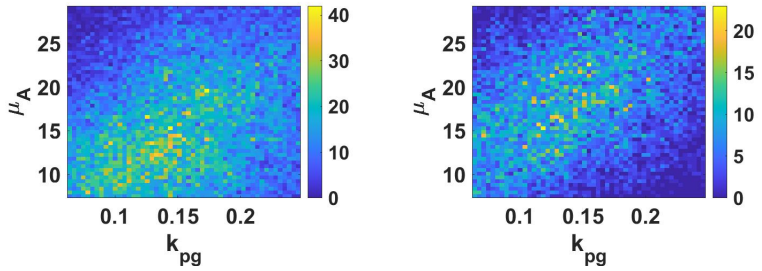

(a) (b)

Figure 54: Pair correlations of some parameters for non-survivors treated that survive or do not survive. (a) survivors μ_A vs k_{pg}, (b) non-survivors μ_A vs k_{pg}.

survivors.

Lastly, the ROC curve and the AUC shown in Fig. 57b provide complementary information to validate the accuracy of the algorithm. The ROC gives the rate of successful classification by the logistic model. In this case the AUC=0.88, which is determined by the threshold of classification given by the coordinate point (0.39,0.9) in the false positive rate vs true positive rate plane. This threshold is automatically chosen by the algorithm.

Table 19: Logistic regression summary for non-survivors after treatment that are classified between survivors and non-survivors

Variable	Coefficient	tstat	Odds	95% CI Odds	% of Change
(Intercept)	-1.749	-97.902	0.174	(0.168 , 0.180)	-82.608
k_{dn}	-1.596	-82.554	0.203	(0.195 , 0.211)	-79.727
k_{pg}	-1.151	-66.535	0.316	(0.306 , 0.327)	-68.373
k_{nod}	-0.991	-62.541	0.371	(0.360 , 0.383)	-62.895
c_2	-0.921	-54.527	0.398	(0.385 , 0.411)	-60.194
α_x	-0.874	-59.463	0.417	(0.405 , 0.429)	-58.272
c_g	-0.783	-54.806	0.457	(0.444 , 0.470)	-54.304
μ_c	-0.721	-49.835	0.486	(0.473 , 0.500)	-51.362
C^*	-0.645	-44.738	0.525	(0.510 , 0.540)	-47.524
μ_m	-0.513	-36.920	0.599	(0.583 , 0.615)	-40.138
c_4	-0.440	-33.551	0.644	(0.628 , 0.661)	-35.608
μ_n	-0.353	-26.672	0.703	(0.685 , 0.721)	-29.727
c_3	-0.349	-26.134	0.706	(0.687 , 0.724)	-29.447
k_A	-0.251	-19.136	0.778	(0.758 , 0.798)	-22.218
k_{pn}	0.296	22.390	1.345	(1.311 , 1.381)	34.514
k_{cn}	0.461	33.907	1.586	(1.545 , 1.629)	58.627
k_{pm}	0.596	42.669	1.815	(1.766 , 1.865)	81.479
μ_{no}	0.908	59.367	2.480	(2.407 , 2.556)	148.042
x_{dn}	1.118	69.961	3.058	(2.964 , 3.156)	205.835
μ_A	1.912	84.706	6.768	(6.475 , 7.074)	576.769

Table 20: Standard deviation for parameters in non-survivors treated

Parameter	STD	Parameter	STD
k_{dn}	0.012	μ_n	0.244
k_{pg}	0.049	c_3	0.857
k_{nod}	5890.5	k_A	0.001
c_2	43.119	k_{pn}	3.024
α_x	0.513	k_{cn}	20.422
c_g	0.777	k_{pm}	8.45e-5
μ_c	2.405	μ_{no}	4233.8
C^*	0.824	x_{dn}	0.107
μ_m	0.001	μ_A	5.69
c_4	850.47		

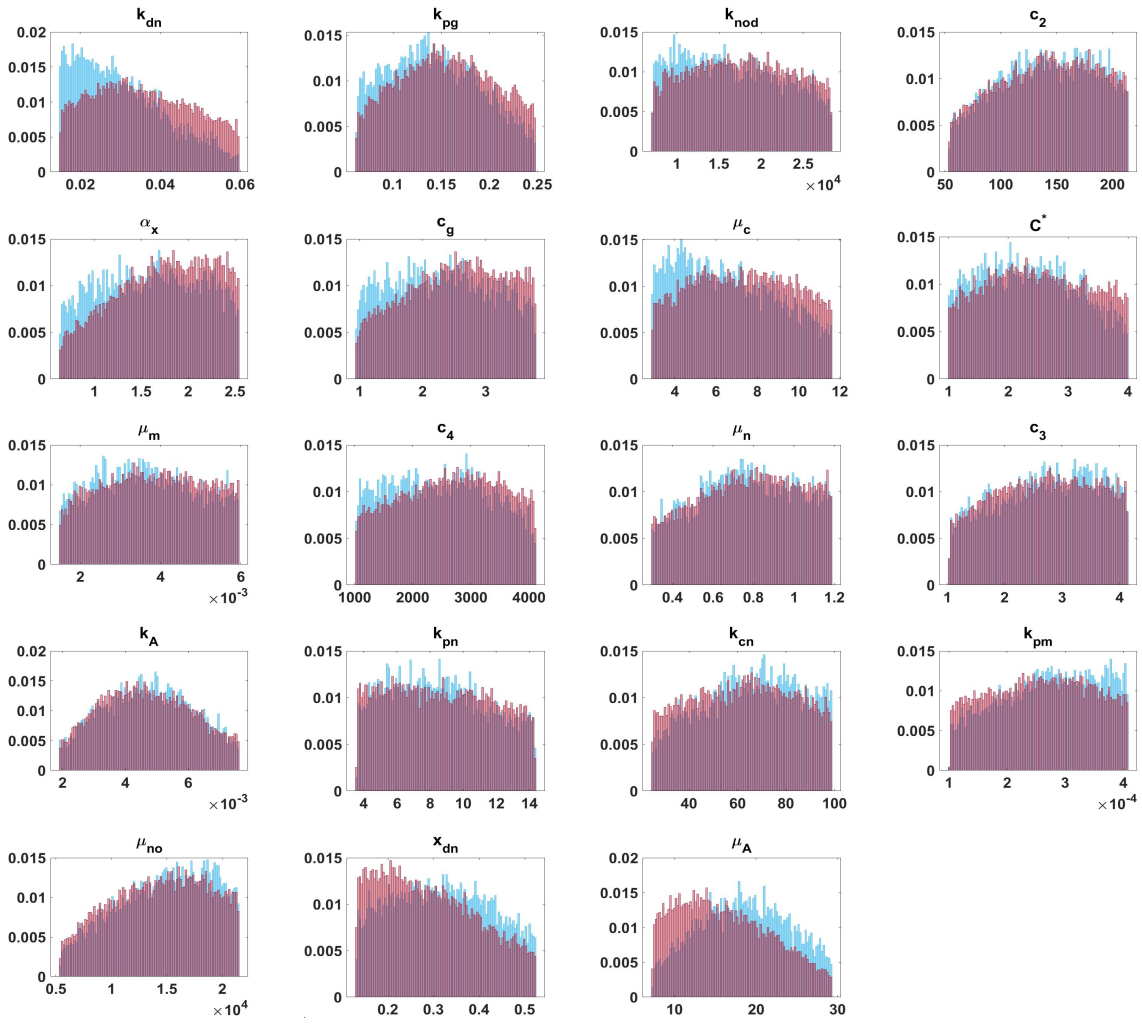

Figure 55: Densities of most contributing parameters for non-survivors after treatment. Non-survivors are colored in maroon whereas survivors are colored in light blue.

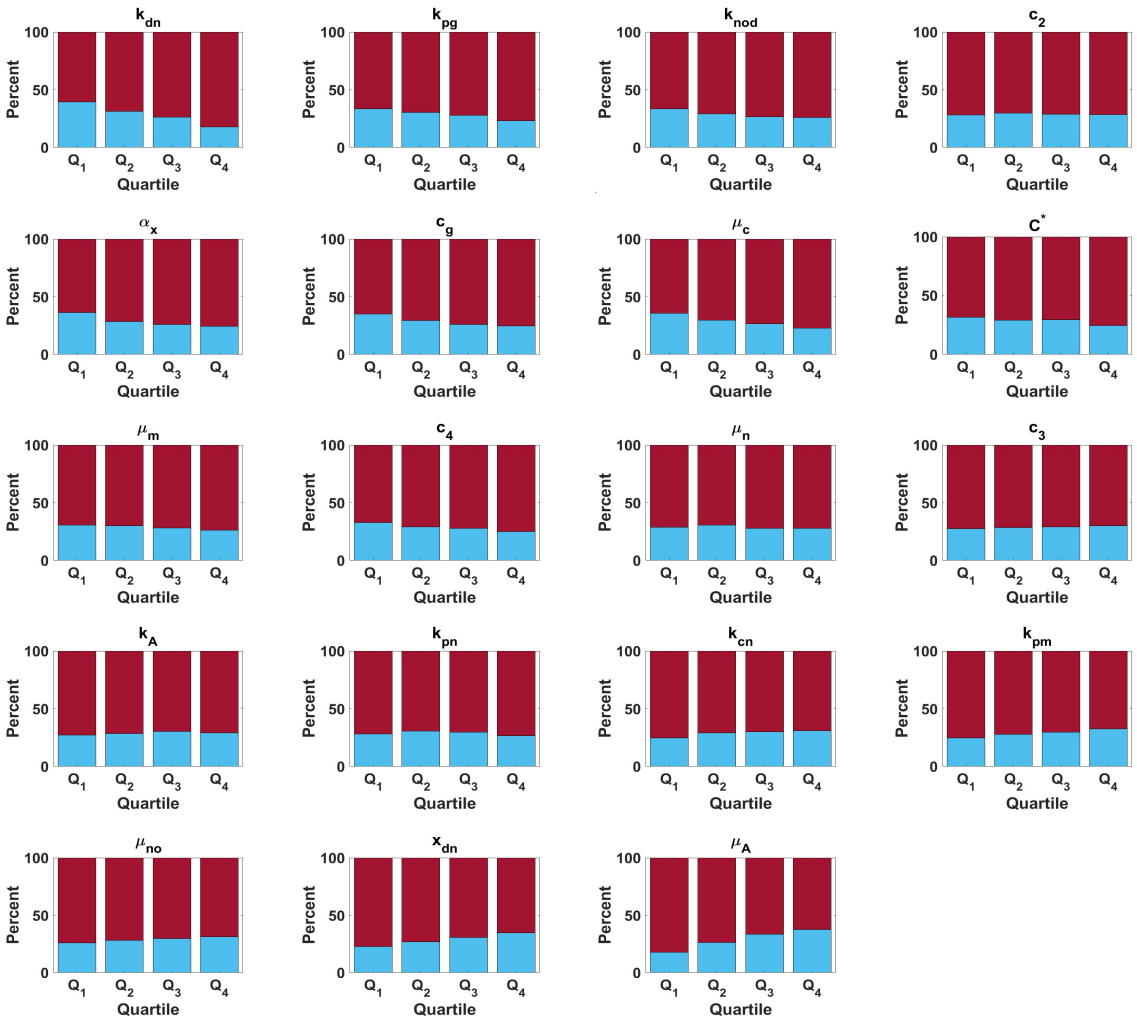

Figure 56: Parameter quartiles of most contributing parameters for non-survivors after treatment. Non-survivors are colored in maroon whereas survivors are colored in light blue

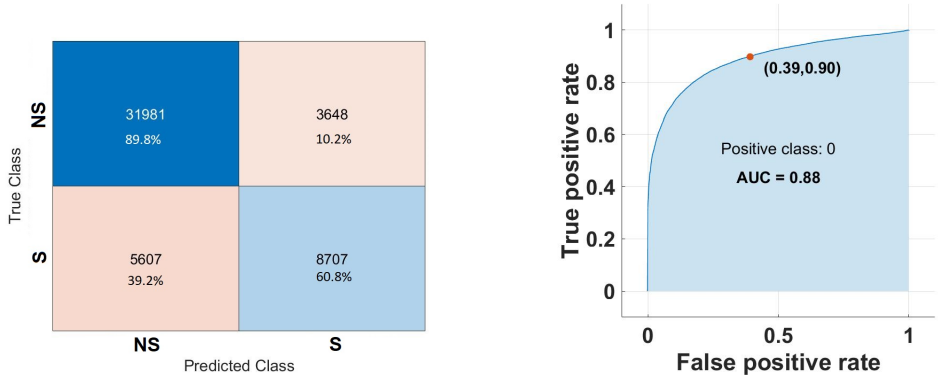

(a) (b)

Figure 57: (a) The confusion matrix contains information about actual and predicted classifications. (b) The ROC and AUC curve for non-survivors after treatment. The red point indicates the true positive rate and true positive rate used in the classification. The area under the curve AUC provides a sense of the degree or measure of separability of the model. The higher the AUC, the better is the model in classifying survivors and non-survivors after treatment.

5.4.4.1 Envelopes for non-survivors treated: survivors and non-survivors In Fig. 58 we observe that there is a clear separation between survivors and non-survivors in the C_A trajectory even before treatment was administered. This early anti-inflammatory response is key in separating the two groups as it sustains inflammatory markers at reasonably lower levels, so that therapy could be more efficient and improve survival. In fact, treatment seems to be more efficient on those subjects whose pathogens are almost completely eliminated around time of drug injection. Once pathogens are sufficiently low, tissue damage depends mostly on X. Then, during the time therapy is applied, from 12 h to 48 h, low levels of X allow tissues to heal. Further, because pathogens are almost eliminated, and damage is on track of recovery, energy can be spent in fueling C_A, which in turn down-regulates phagocytes and other inflammatory markers. In summary, a combination of high levels of anti-inflammatory mediators with proper energy availability seems to play a major role in the path of recovery if treatment is administered.

5.4.4.2 Envelopes for non-survivors treated: septic and aseptic The non-survivor cohort, can be further classified between septic and aseptic. The corresponding envelopes are shown in Fig. 59. We observe that sepsis is associated to lower phagocytic activity due to A_n depletion. In the aseptic group, pathogens are almost eliminated at the time of therapy induction and therefore tissue damage is depending only on nitric oxide. Therapy then allows tissue damage in aseptic to slightly recover or at least to grow at a slower pace compared to septic subjects. This allows A_b to recover, as it is no longer needed to fight P anymore. A small rebound in glucose also helps the recovery of A_n, which can be used to produce N and C_A to keep balancing inflammation. However, the continuous pathogen replication in sepsis requires more and more activation of phagocytes which leads to high levels of X and L.

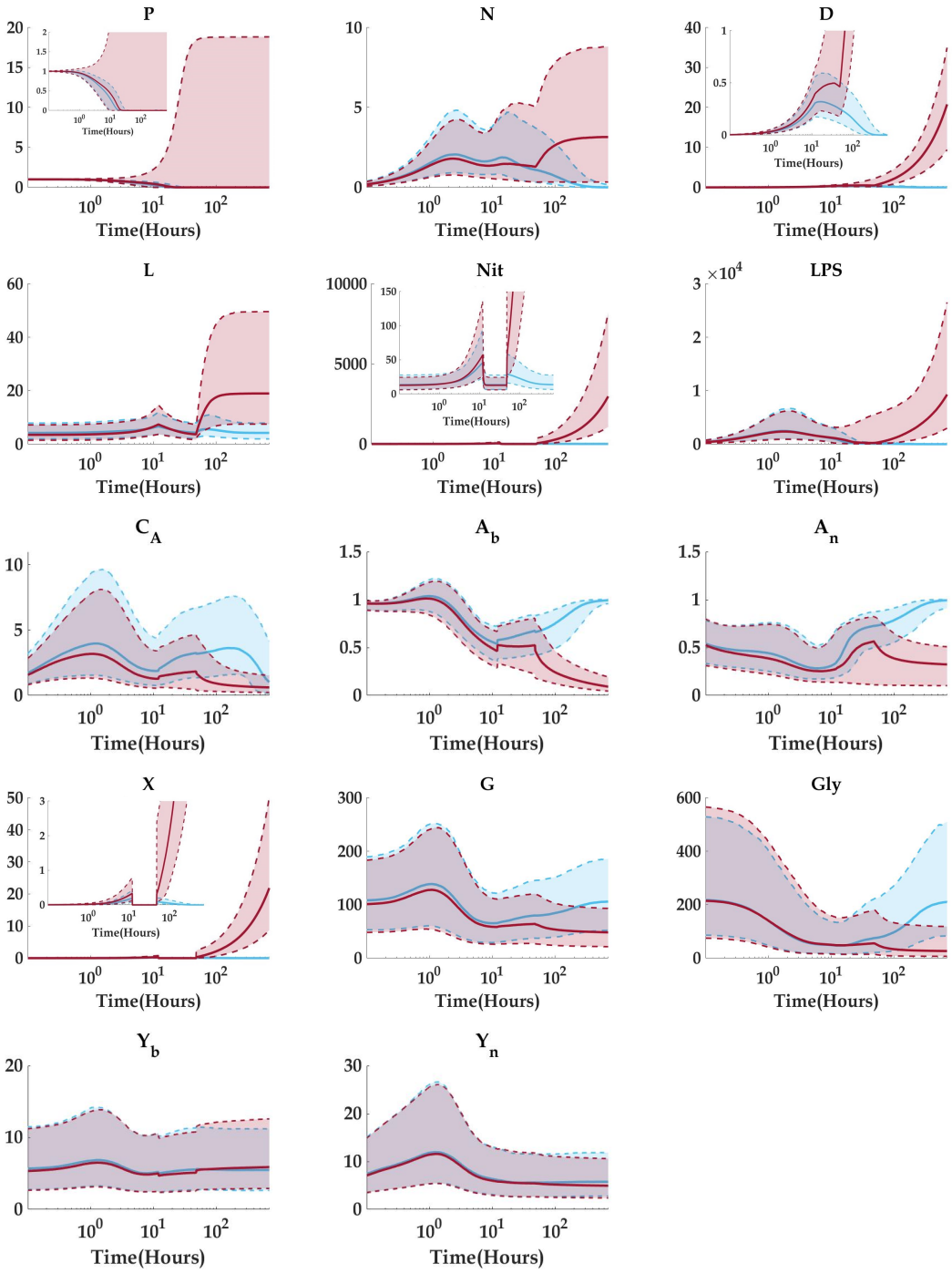

Figure 58: Predicted intervals of model trajectories obtained with parameters distributions of non-survivors treated. After treatment subjects either survive or die. Non-survivors envelopes are colored maroon whereas survivors envelopes are light blue. The solid maroon and light blue lines correspond to the medians of the sampled trajectories and the shaded regions bounded by the dashed lines enclose the $5\% - 95\%$ confidence interval.

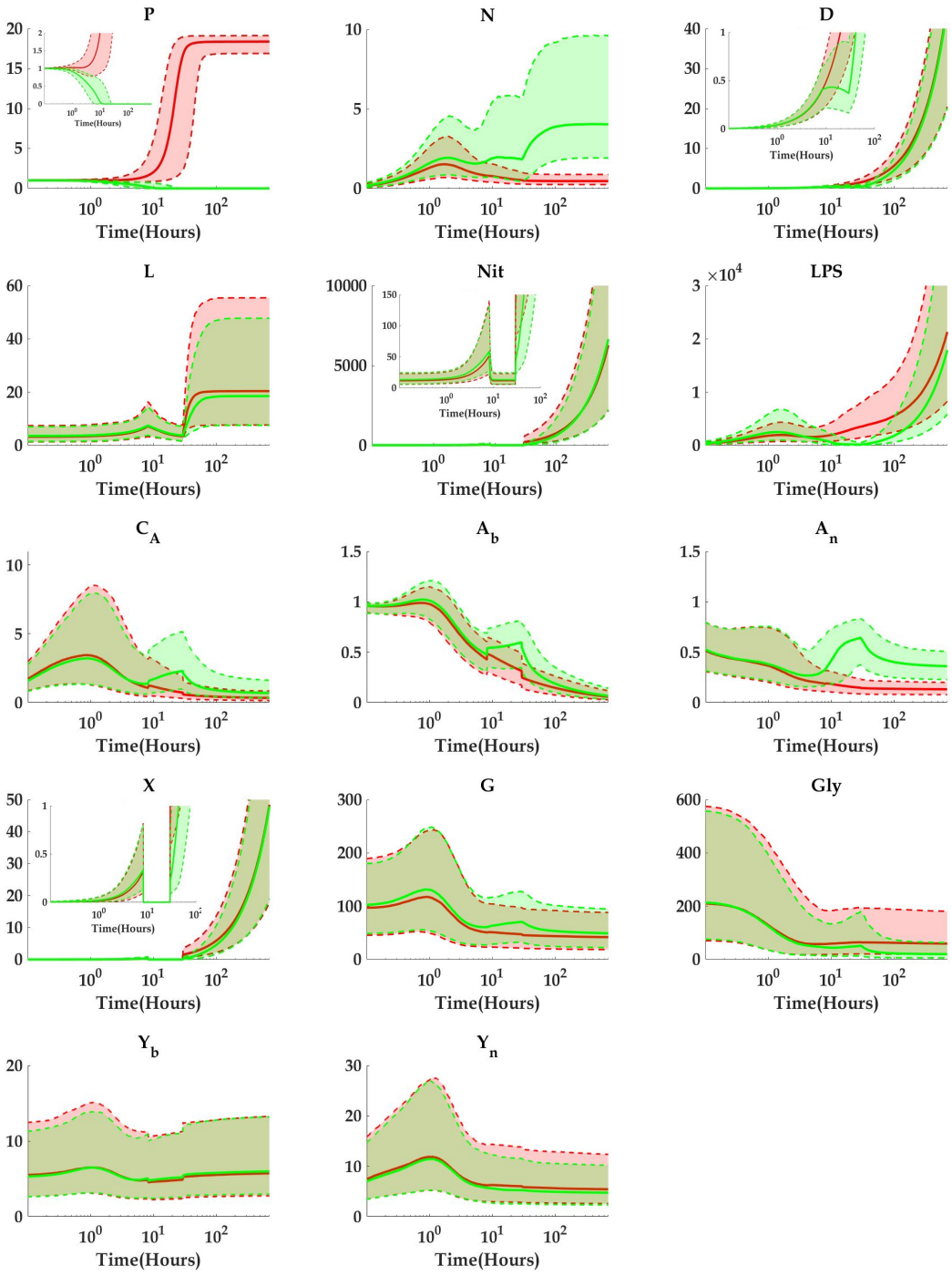

Figure 59: Predicted intervals of model trajectories obtained with parameters distributions of non-survivors treated. Non-survivors are either septic or aseptic. Aseptic are colored in green and septic are in red. The solid red and green lines correspond to the medians of the sampled trajectories and the shaded regions bounded by the dashed lines enclose the $5\% - 95\%$ confidence interval.

5.5 The role of anti-inflammatory mediators and glucose

In this section we explore different scenarios where we vary either the anti-inflammatory source parameter s_c or the glucose intake parameter s_g. With this, we aim to understand the individual role of C_A and glucose in an entire population. In particular we consider four cases: low s_g, high s_g, low s_c and high s_c.

Our model suggests that increasing the source of anti-inflammatory mediators (high s_c) could lead to two different outcomes. In some cases higher C_A could be beneficial as inflammation is controlled, down-regulation of nitric oxide production occurs and consequently diminishing collateral tissue damage. However, in some other cases, higher anti-inflammation over inhibits phagocytic activity, compromising pathogen elimination and in turn, septic cases increase. Because phagocytes are highly inhibited, the only resource for pathogen elimination is non-specific killing. This can be observed in the compromised N trajectory after 10 hours, and the increased Φ_1 shown on Fig. 60. These results are also consistent to the findings in [61]. The results of high anti-inflammatory source are shown in the last column of Table 21.

On the other hand, lowering s_c does not show a significant difference in neither the distribution of cases between health, septic, and aseptic nor in the probability of survival. This is shown in Table 21 where we decreased the anti-inflammatory source s_c by 75% in every subject. The reason why decreasing s_c does not have a major impact in the population is because there is enough circulating C_A whose production has already been triggered as a response to phagocyte activation and tissue damage. This is a result the relatively large estimates in parameters like k_{cn}, μ_c, and s_c, which suggest a relatively rapid anti-inflammatory response that dominates in the process.

We also explored the potential consequences of varying glucose intake. We note that energy plays a major role in patient outcome and in the dynamics of our model. As a matter of fact, for the high s_g case, an increment of 20% in the glucose source parameter, s_g leads to a reduction in mortality of 32%. Such mortality reduction mostly coming from aseptic subjects that are able to recover from over-inflammation due to better ability to heal tissue damage as seen in Fig. 61. On the other hand, lowering glucose availability (low s_g) results

on a significant increment in mortality of 18.8% with respect to baseline. A combination of poor anti-inflammatory mediators and insufficient energy to fuel phagocytosis leads to an increment of 287% in septic cases. This was obtained by reducing s_g by 20% for each subject in the virtual population.

Table 21: Exploring role of glucose and anti-inflammatory mediators

	Baseline	Low s_g	High s_g	Low s_c	High s_c
Health	1252	309	2804	1248	1438
Aseptic	3035	2623	1684	3063	2486
Septic	713	2049	507	689	1064
Total	5000	4981	4995	5000	4988
Prob. Non-Surv.	75%	93.8%	43.86%	75%	71.17%

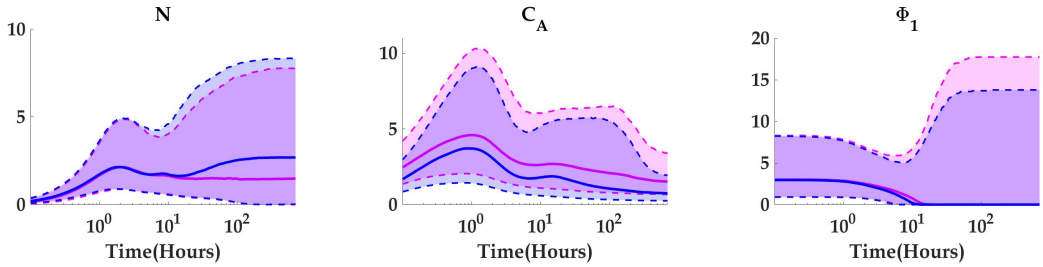

Figure 60: Predicted intervals of model trajectories obtained after C_A enhance by increasing s_c by 400% with respect to baseline. Here we are displaying only those variables that show significant differences between the two groups. The solid blue line corresponds to the median of the baseline trajectories, whereas the magenta solid line corresponds to the modified distribution with higher s_c. The color shaded regions enclose the $5\% - 95\%$ confidence interval.

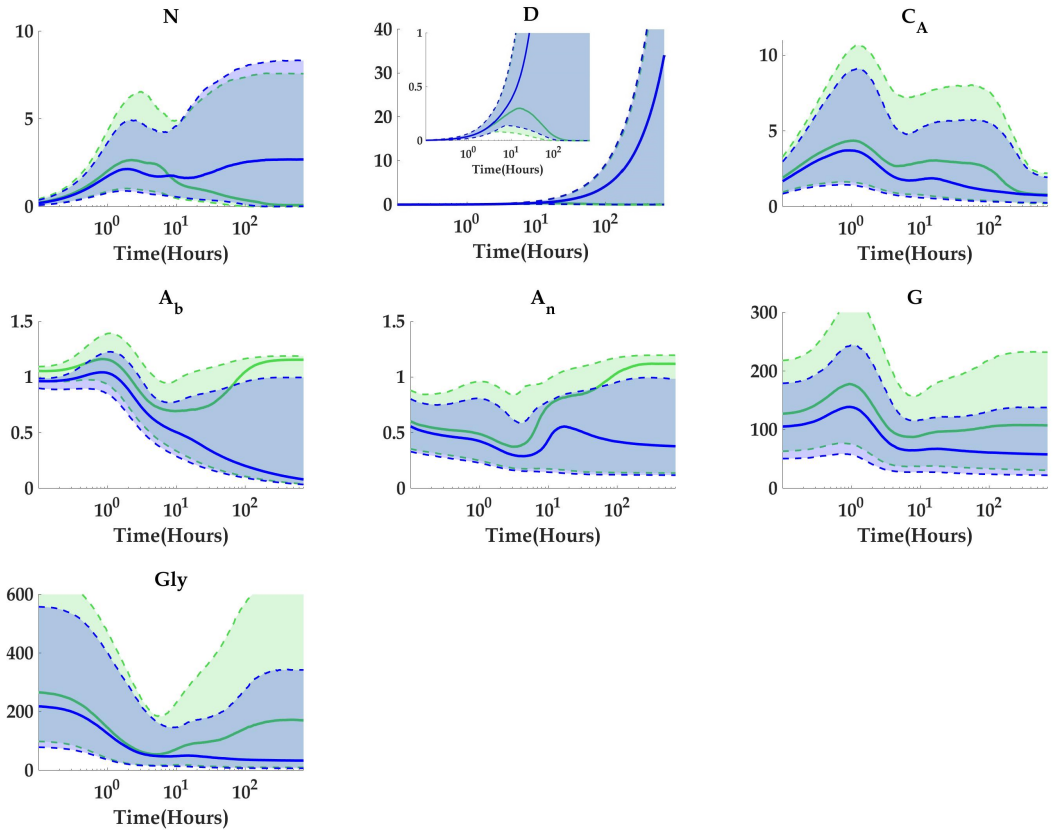

Figure 61: Predicted intervals of model trajectories obtained after enhancing glucose intake by 20%. Here we are displaying only those variables that show significant differences between the two groups. The solid blue line corresponds to the median of the baseline trajectories, whereas the green solid line corresponds to the modified distribution with higher s_g. The color shaded regions enclose the $5\% - 95\%$ confidence interval.

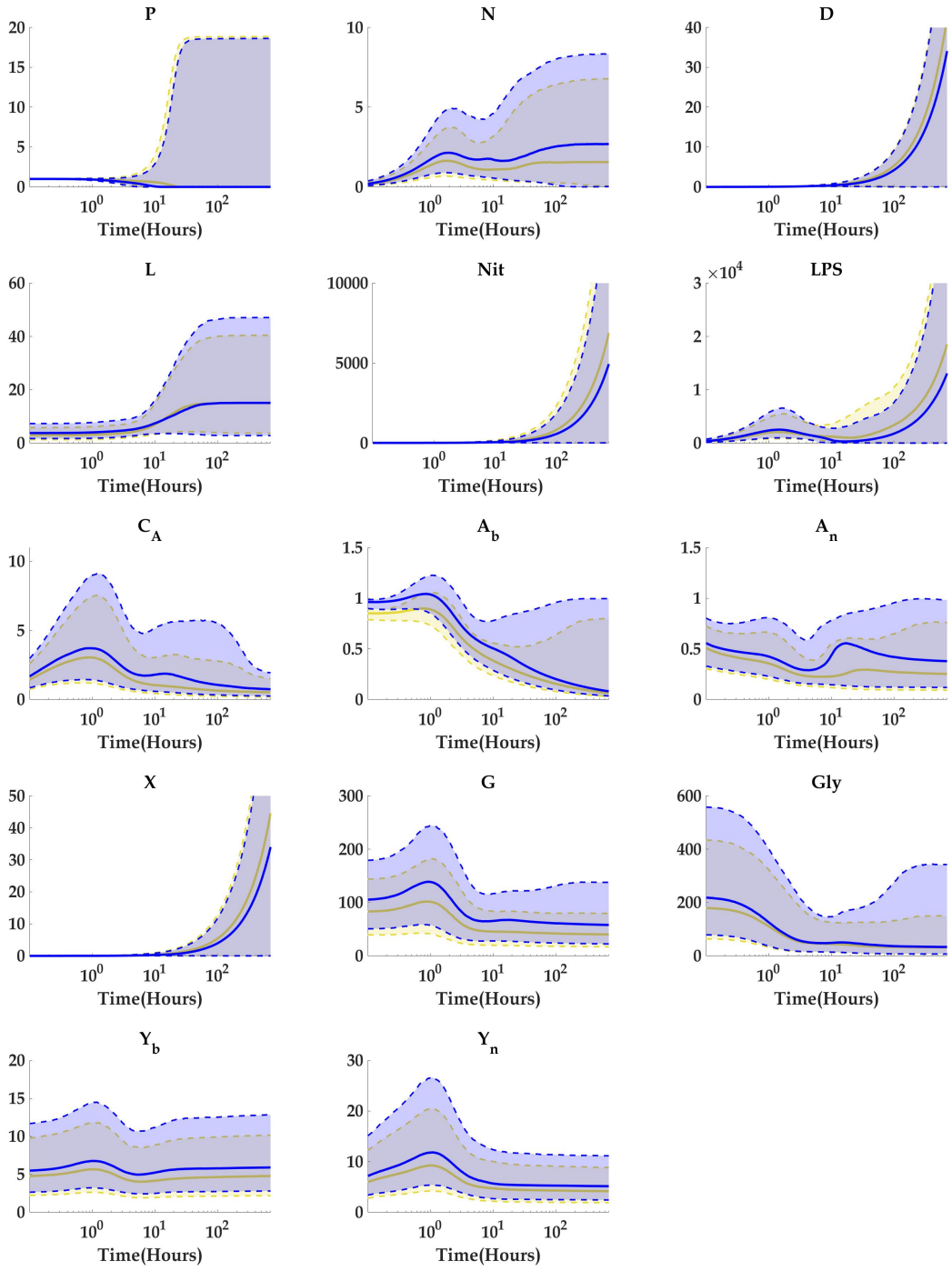

Figure 62: Predicted intervals of model trajectories obtained after lowering glucose intake by 20%. The solid blue line corresponds to the median of the baseline trajectories, whereas the yellow solid line corresponds to the modified distribution with lower s_g. The color shaded regions enclose the $5\% - 95\%$ confidence interval.

5.6 Discussion

In this chapter we started by using our extended model and the virtual population X_{tot} constructed in Section 4.3.3, to explore how hypoglycemia and hyperglycemia affect the virtual population while fighting a pathogenic infection. As expected, because of the work presented in Section 2.4, hypoglycemia has a major impact in mortality. Patients that under normal circumstances would have survived, were highly impacted by the induction of hypoglycemia and ended up dying. Although at a lower extend than hypoglycemia, hyperglycemia also proves to benefit sepsis resulting in an increment in mortality.

With our model, we also introduced the dynamics of an NOS inhibitor to be given at 12 hours after pathogen infection and during a continuous infusion that lasted until 48 hours. We introduced therapy into our virtual population X_{tot} and compared the results with the available data of 16 baboons who were treated with the NOS inhibitor at the mentioned time. Using a Metropolis algorithm with informative prior, we fitted the treated subjects data and obtained probability of survival that were, in most of the cases, consistent with the actual data. Work still needs to be done to improve the fits in non-survivors, especially in lactate measurements. Our model does not reflect the rise in lactate during therapy that is observed in three of the four non-survivors who were treated.

We also explored different times of therapy induction and our results suggest that early diagnosis and therefore early therapy can have a major role in reducing mortality. In fact, we found that introducing therapy after 8 hours of infection could improve survival by about 7%. However some limitations are observed in our model as it predicts higher survival when treatment is induced as early as 2 hours, whereas in practice such an early treatment is not realistic when treating real patients. Presumably there has to be certain period of time between infection, diagnosis, and treatment. Moreover, based on the observations made in the original baboon study, no side effects were observed. However, NOS inhibitors can cause a variety of side effects that were not contemplated into our model. Future directions can include such side effects when calibrating the model with potential new data.

We used logistic regression models to determine key model parameters that can serve as patient outcome predictors. In particular we determined biological processes that proved

to be significant to predict whether a patient will survive or not-survive, including the scenario when nitric oxide inhibition treatment is administered. Similarly, we found significant parameters to determine outcome within the non-survivor group between aseptic and septic.

As a matter of fact, when classifying survivors and non-survivors, we found 12 parameters that were significantly good predictors. These include the energy rate μ_A, the proportion of energy consumed during phagocytosis c_2, the phagocytosis rate k_{pn}, α_x which is the scaling parameter between molecules of nitric oxide and the level of pathogens, and x_{dn}, which is the half saturation level of the tissue damage marker. For instance, we found that spending too much energy during phagocytosis, that is high c_2 values, has a negative effect for survival, whereas patients with higher energy rate μ_A, are more likely to survive.

Similarly, we found that 5 parameters were particularly relevant to predict outcome between septic or aseptic patients. These parameters are the pathogen growth rate k_{pg}, the energy μ_A, the half-activation for the non-specific local response μ_m, the rate of pathogen elimination by non-specific local response k_{pm}, and the energy consumption rate of phagocytosis c_2. The fact that k_{pg} is an important predictor between septic and aseptic does not come as a surprise, as its relevance was also explored in Chapter 2 and published in [59]. However, the fact that energetics play an important role in this case is part of the new information we learned with our model.

Lastly, to predict therapy success, we found that pathogen virulence k_{pg}, energy rate μ_A, tissue damage half saturation level x_{dn}, and intrinsic decay rate of nitric oxide, μ_{no}, are some of the parameters that play important roles. In particular, patients with high energy rate are more likely to survive when treatment is administered. Likewise for those whose pathogen growth rate is low.

We also explore the role of high and low values of inflammatory mediators as well as low and high glucose in a virtual population. This was accomplished by tuning parameters involved in anti-inflammatory cytokines production and glucose intake. Our model suggests that low glucose intake can compromise energy availability to fuel the immune response leading to an increment in mortality. On the other hand, we found that an increment in circulating anti-inflammatory cytokines reduces mortality.

Logistic regression models have been used to predict patient outcome in different settings.

In particular, Seymour et. al [65] used logistic regression to predict outcome in septic patients using information including systolic blood pressure and patient respiratory rate. However, caution must be practiced when interpreting the results provided as logistic regression also has certain limitations. In particular, the analysis assumes the effect of one predictor is not influenced by the effect of the other. However this is not always true, as there might be cases when two processes interact with each other but yet be represented by two different predictors [78].

In a study similar to what we presented in this thesis, Malkin et. al [51] developed a computational model to explore how different levels of neutrophil activation impact survival on septic subjects. In particular, they explored the role of different neutrophil phenotypes, including killer, migratory, and dual neutrophil phenotypes to predict survival in an animal study. Further, they used an *in silico* extracorporeal treatment that modulates CXCR-1/2 neutrophil surface receptors and found an improvement in survival when deployed under certain ranges of conditions. They used parallel tempering for parameter estimation and stepwise logistic regression to identify model parameters to predict mortality. The animal data they used was taken from a similar baboon study done by the same group that performed the baboon study used in this thesis [62]. In this animal study, they followed the same protocol on which sixteen baboons (*Papio ursinus*) were infused 2×10^9 CFU intravenous *E.coli* for a period of two hours. The study was followed for a maximum of 28 days [63]. In summary in their work, Malkin et. al presented a model that describes interactions of neutrophils taking into account systemic variables and neutrophil receptors. Our work on the other hand, not only takes into account the interplay between neutrophils and their inflammatory effects, but it also takes into account the energy supply and demand required by netrophils to fight a pathogenic infection and supports previous findings that relate low ATP levels with sepsis. Also, the fact that we incorporate the link between inflammation and tissue damage through nitric oxide, allowed us to explore the effect of an alternative type of therapy (an NOS inhibitor), which was effective in the animal study but has shown negative results when used in human patients.

Although our model is complex, it is still an oversimplification of the many biological processes involved during the inflammatory response. Therefore caution should also be

practiced when interpreting the results presented in this chapter. These results should be used to complement medical knowledge and other findings in the field.

6.0 Conclusions

The inflammatory response requires energy. As a result, a diminished energy supply compromises the body's ability to mount a response to the presence of pathogens or related insults. Interestingly, since a healthy inflammatory response requires an appropriate balance and temporal interplay of pro- and anti-inflammatory elements, the effects of this compromise are not obvious. With reduced energy, the activation and effectiveness of pro-inflammatory components are limited, suggesting that the inflammatory response could become inadequate to eliminate pathogens. Less energy could also prove detrimental by limiting anti-inflammatory production and allowing inflammation to spiral out of control, or it could prove helpful by reducing damage-related effects of pro-inflammation. Clearly, the net result of reduced energy is difficult to predict. A computational model provides a helpful tool for evaluating the outcome of such tradeoffs in a variety of scenarios.

The goal of the work presented in this thesis was to provide qualitative and quantitative evidence of the relation between low energy levels combined with high presence of both nitric oxide and lactate, and the consequential high mortality of sepsis observed in the ICU. More specifically, we wanted to identify which biological factors play important in distinguishing between patients that recover from sepsis and those who do not and therefore die.

In general the work presented in this thesis can be divided into two parts; one consisting of a forward problem and the second of an inverse problem. In the forward problem, we proposed mathematical models that enclose the dynamics of the biological problem of interest. In the inverse problem, we use parameter estimation techniques to calibrate our model and extract relevant biological information that can be used to provide feedback and help physicians to make decisions when dealing with septic patients. Moreover, with the parameter estimates and uncertainty quantification, we explored different scenarios including patient heterogeneity, and treatment protocols.

More specifically, Chapter 2 consisted in the understanding, development, and implementation of a mathematical model that connects the acute inflammatory response with the energy consumption required to accomplish such response. We constructed a theoretical

model of ordinary differential equations in which we included several metabolic processes involved in the inflammatory response against pathogens along with the energetic requirements for such response to take place. Numerical explorations such as bifurcation analysis and numerical solutions of variations of the model allowed us to study metabolic conditions and their effect in a virtual population. We used the model to explore metabolic conditions like hypoglycemia, hyperglycmia, and hypoxia. The results obtained therein provided qualitative features that were consistent with the biology and the literature. Still as part of the forward problem, in Chapter 3, we followed a data-driven approach to extend our initial model to a model that includes variables that are typically measured in the ICU including glucose, lactate, LPS, nitrate, and elastase.

Chapter 4 consists of a backward problem on which animal data was used to obtain model parameter estimates. We did this in two stages, starting with a standard ordinary least squares (OLS) like approach to obtain an initial local minimum in the parameter space for the weighted sum of squares distance function. In the second stage, we followed a Bayesian approach to quantify uncertainty in the model parameters. In this process, we constructed a virtual population that resembles the variability observed in the animal data and that can be used to represent real patient heterogeneity. We validated our model and the virtual population comparing model results with data via a Metropolis algorithm with informative prior. We obtained results that were, for the most part, consistent with the data. We concluded that we can use our model to predict patient outcome from new data and that early measurement recording is important to improve accuracy of mortality predictions.

In Chapter 5, we used our extended model as a tool to explore the role of hypoglycemia and hyperglycemia in the virtual population and we observed that these two conditions benefit sepsis and increase mortality. We further extended our model to study the therapeutic effect of a nitric oxide inhibitor. We showed how our model can be used to predict patient outcome with new data from subjects who undergo treatment. We also explored different therapy protocols based on duration and time of induction and we determined that early diagnose and therefore early therapy can positively impact survival.

Lastly, with the help of logistic regression models, we identified key parameters that can be used as patient outcome predictors. We focused on three different scenarios: survivors and

non-survivors, within the non-survivors septic and aseptic, and survivors and non-survivors for patients that were treated with an NOS inhibitor. In particular, we found that parameters like energy rate, half tissue damage saturation constant, and energy consumption rate of phagocytosis proved to be some of the most significant to predict patient outcome between survivors and non-survivors. In our model, the energy rate, denoted by μ_A, appears in the production and depletion of ATP and hence it is involved in all mechanisms that require energy to take place, that is all the energy consumption fluxes denoted by Φ_i in the model and in the natural elimination of both ATPs, A_b and A_n. The half tissue damage saturation constant x_{dn} determines the levels of pathogens and nitric oxide needed to bring tissue damage production to half its maximum and the energy consumption rate of phagocytosis is given by c_2. Our model suggests that a high energy consumption during phagocytosis combined with a low energy rate constant could be considered a warning sign. The effects of a low energy rate constant are complicated as μ_A participates in both production and depletion of both ATPs. However, a slow energy rate leads to a slow ATP metabolism which results in a poor energy availability that compromises the immune response. Therefore patients with higher energy rate constant and low energy demand during phagocytosis are more likely to survive.

Similarly, we found that pathogen growth rate, energy rate and the energy consumption rate of phagocytosis were all good predictors between septic and aseptic subjects. Lastly, we found 19 parameters that are good predictors of survival in patients that undergo NOS inhibition treatment. Some of these parameters are again the energy rate, half tissue damage saturation constant, pathogen growth rate, and tissue damage production. Given this knowledge in impactful parameters we suggest that in order to increase chances of survival after treatment administration, energy rate must be enhanced.

Our model also suggests that the faster ATP is depleted, the faster energy is being used to fight the infection. However, there needs to be a balance between energy consumption and production. Energy must be enough to fuel anti-inflammatory cytokines and tissue healing. But there needs to be certain control in the amount of energy spent in phagocytosis.

Future directions for extending this work include model variations that will account for adaptive mechanisms that cells have developed to accommodate shortages in energy supply,

[66]. We also intend to expand our models to consider the dynamics of different organs in the host and therefore use it to study multiple organ dysfunction syndrome (MODS). Moreover, optimal control techniques can be applied to determine optimal treatment strategies to fight infection and simultaneously reduce side effects [25], [75], [72]. How soon should patients in the ICU be fed has been a topic of discussion [33]. Optimal control techniques and model simulations can also be applied to determine optimal timing of nutrition. Finally, inclusion of certain treatments that address hyperglycemia, hypoglycemia or hypoxia might also be considered in future work. Hopefully, designing these treatment strategies using a computational model will allow for approaches that are tailored to individual patient characteristics, allowing for a much more extensive exploration of options, with a more refined capability to address specific patient needs, than can be achieved in clinical settings.

Appendix Individual fits with DRAM

In Section 4.3.3 we found individual fits and envelopes for 16 subjects. However therein we only presented 4 of the 12 envelopes for the non-survivors. For completeness we present here the individual envelopes obtained with DRAM by fitting the data of the remainder non-survivors NS66, NS67, NS69, NS76 in Fig. 63 and NS80, NS92, NS97, and NS104 in Fig. 64.

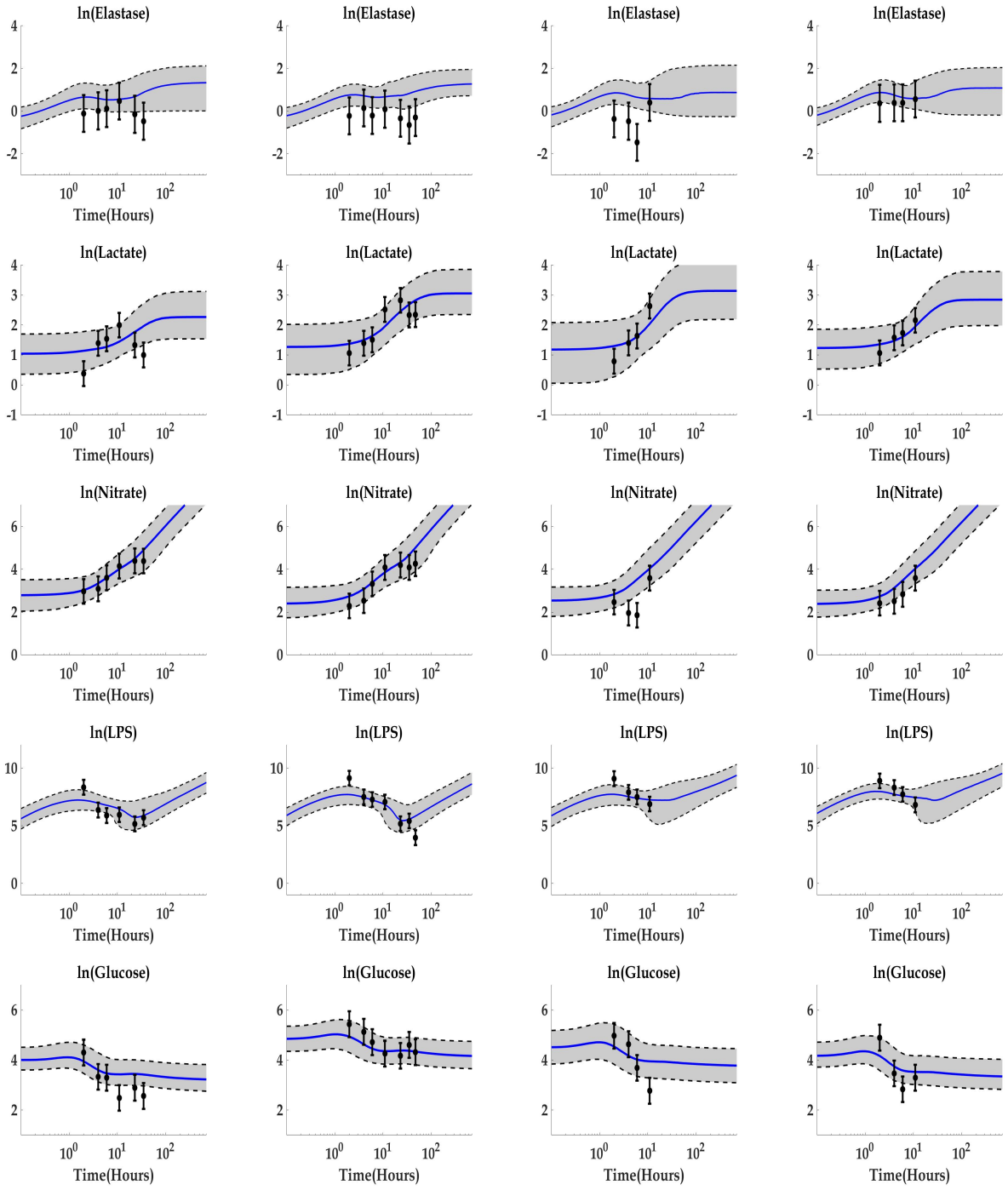

Figure 63: Envelopes of observed trajectories for subjects (a) NS66, (b) NS67, (c) NS69, and (d) NS76 obtained with DRAM. The solid blue line corresponds to the median of the sampled trajectories and the shaded gray regions enclose the $5\% - 95\%$ confidence intervals. The black dots correspond to the data and the bars the average of the standard deviation of the treated non-survivors.

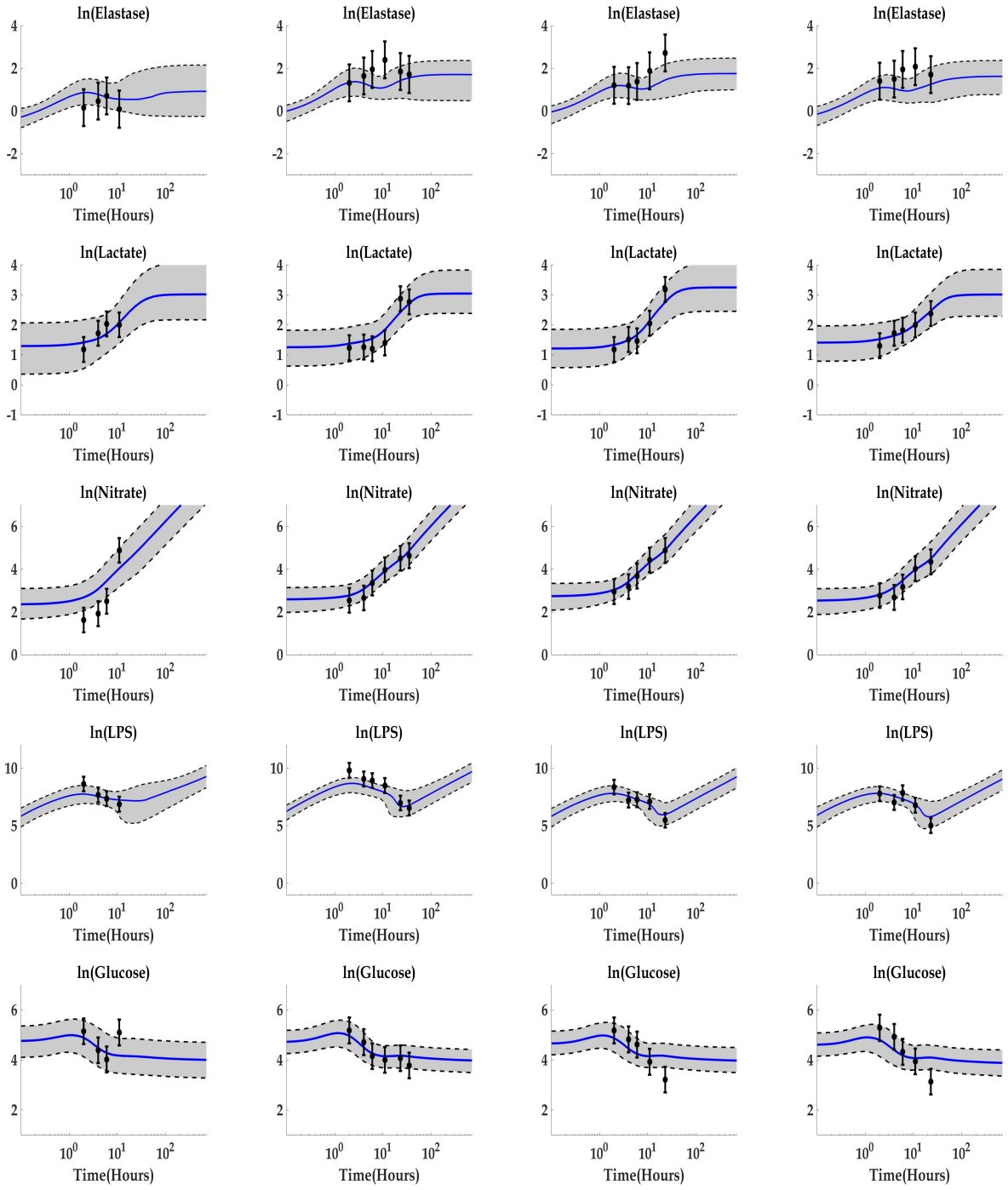

Figure 64: Envelopes of observed trajectories for subjects (a) NS80, (b) NS92, (c) NS97, and (d) NS104 obtained with DRAM. The solid blue line corresponds to the median of the sampled trajectories and the shaded gray regions enclose the $5\% - 95\%$ confidence intervals. The black dots correspond to the data and the bars the average of the standard deviation of the treated non-survivors.

Bibliography

[1] Sepsis Alliance. Sepsis fact sheet, 2018. Date Accessed:4-19-2018.

[2] U. Andersson, H. Wang, K. Palmblad, A. C. Aveberger, O. Bloom, H. Erlandsson-Harris, A. Janson, R. Kokkola, M. Zhang, H. Yang, and K. J. Tracey. High mobility group 1 protein (hmg-1) stimulates proinflammatory cytokine synthesis in human monocytes. *J. Exp Med*, 192:565–570, 2000.

[3] G. E. Bacon, F. M. Kenny, H. V. Murdaugh, and C. Richards. Prolonged serum half-life of cortisol in renal failure. *Johns Hopkins Med J*, 132:127–131, 1973.

[4] H.T. Banks and H.T. Tran. *Mathematical and Experimental Modeling of Physical and Biological Process*. Taylor and Francis Group, New York, 2009.

[5] K. Bartels, A. Grenz, and H.K. Eltzschig. Hypoxia and inflammation are two sides of the same coin. *Proceedings of the National Academy of Sciences*, 110(46):18351–18352, 2013.

[6] J. M. Berg, J. L. Tymoczko, and L. Stryer. *Biochemistry*. W H Freeman, New York, 5th edition, 2002. Section 18.6, The regulation of cellular respiration is governed primarily by the need for ATP.

[7] F. Bianconi, L. Tomassoni, C. Antonini, and Valigi P. A new bayesian methodology for nonlinear model calibration in computational systems biology. *Front. Appl. Math. Stat.*, 6(25), 2020.

[8] V. Bocci. Interleukins. clinical pharmacokinetics and practical implications. *Clin. Pharmacokinet*, 21:274–284, 1921.

[9] N. Borregaard and T. Herlin. Energy metabolism of human neutrophils during phagocytosis. *J Clin Invest*, 70:550–557, 1982.

[10] A. Branwood, K. Noble, and K. Schindhelm. Phagocytosis of carbon particles by macrophages in vitro. *Biomaterials*, 19:646–648, 1992.

[11] F. Brauer and C. Castillo-Chavez. *Mathematical Models in Population Biology and Epidemiology*. Springer, New York, NY, 2012.

[12] D. Brealey, M. Brand, I. Hargreaves, S. Heales, J. Land, R. Smolenski, N.A. Davies, C.E. Cooper, and M. Singer. Association between mitochondrial dysfunction and severity and outcome of septic shock. *Lancet*, 360:219–223, 2002.

[13] D. Brealey, S. Karyampudi, T.S. Jacques, M. Novelli, R. Stidwill, V. Taylor, R.T. Smolenski, and M. Singer. Mitochondrial dysfunction in a long-term rodent model of sepsis and organ failure. *Am J Physiol Regul Integr Comp Physiol*, 286:R491–7, 2004.

[14] P. S. Brookes, J. P. Bolaños, and S. J. R. Heales. The assumption that nitric oxide inhibits mitochondrial atp synthesis is correct. *FEBS*, 446:261–263, 1999.

[15] G. C. Brown. Nitric oxide as a competitive inhibitor of oxygen consumption in the mitocondrial respiratory chain. *Acta Physiol Scand*, 168:667–674, 2000.

[16] L. T. Buck and P. W. Hochachka. Anoxic suppression of na^+-k^+-atpase and constant membrane potential in hepatocytes: support for channel arrest. *Am J Physiol,.*, 265(5):R1020–R1025, Nov 1993.

[17] F. Buttgereit and M. D. Brand. A hierarchy of atp-consuming processes in mammalian cells. *Biochem J. Portland Press Ltd*, 312(15):163–167, Nov 1995.

[18] J. E. Carré and M. Singer. Cellular energetic metabolism in sepsis: The need for a systems approach. *Biochimica et Biophysica Acta*, 1777:763–771, 2008.

[19] C. C. Chow, G. Clermont, R. Kumar, C. Lagoa, Z. Tawadrous, D. Gallo, B. Betten, J. Bartels, G Constantine, M.P. Fink, T.R. Billiar, and Y. Vodovotz. The acute inflammatory response in diverse shock states. *Shock*, 24(1):74–84, 2005.

[20] G. Clermont, J. Bartels, R. Kumar, G. Constantine, Y. Vodovotz, and C.Chow. In silico design of clinical trials: A method coming of age. *Crit Care Med*, 32(10), 2004.

[21] R.L. Cooper, R.A. Segal, R.F. Diegelmann, and A.M. Reynolds. Modeling the effects of systemic mediators on the inflammatory phase of wound healing. *Journal of Theoretical Biology*, 367:86–99, 2015.

[22] A. Coxon, T. Tang, and T. N. Mayadas. Cytokine-activated endothelial cells delay neutrophil apoptosis in vitro and in vivo. a role for granulocyte/macrophage colony-stimulating factor. *J. Exp Med*, 190:923–934, 1999.

[23] C. E. Cressler, W. A. Nelson, T. Day, and E. McCauley. Disentangling the interaction among host resources, the immune sytem and pathogens. *Ecology letters*, 17:284–293, 2014.

[24] S. Daun, J. Rubin, Y. Vodovotz, A. Roy, R. Parker, and G. Clermont. An ensemble of models of the acute inflammatory response to bacterial lipopolysaccharide in rats: Results from parameter space reduction. *J. Theor. Biol*, 253:843–853, 2008.

[25] J. Day, J. Rubin, and G. Clermont. Using nonlinear model predictive control to find optimal therapeutic strategies to modulate inflammation. *Mathematical Biosciences and Engineering*, 7:739–763, 2010.

[26] J. Day, J. Rubin, Y. Vodovotz, C. C. Chow, A. Reynolds, and G. Clermont. A reduced mathematical model of the acute inflammatory response II. Capturing scenarios of repeated endotoxin administration. *J. Theor. Biol*, 242:237–256, 2006.

[27] X. Dong, P. T. Foteinou, S. E. Calvano, S. F. Lowry, and I. P. Androulakis. Agent-based modeling of endotoxin-induced acute inflammatory response in human blood leukocytes. *PLoS ONE*, 5(2), 2010.

[28] J. Duran-Bedolla, M. A. Montes de Oca-Sandoval, V. Saldana-Navor, J. A. Villalobos-Silva, M. C. Rodriguez, and S. Rivas-Arancibia. Sepsis, mitochondrial failure and multiple organ dysfunction. *Clin Invest Med*, 37(2):E58–E69, 2014.

[29] H. K. Eltzschig and P. C. Carmeliet. Hypoxia and inflammation. *N Engl J Med*, 364(7):656–665, 2011.

[30] H.K. Eltzschig and T. Eckle. Ischemia and reperfusion—from mechanism to translation. *Nat Med*, 17(11):1391–1401, 2011.

[31] B. Ermentrout. *Simulating, Analyzing, and Animating Dynamical Systems. A Guide to XPPAUT for Researchers and Students.* SIAM, Philadelphia, PA, 2002.

[32] R. Bradyand D.O. Frank-Ito, H.T. Tran, S. Janum, K. Møller, S. Brix, J.T. Ottesen, J. Mehlsen, and M. S. Olufsen. Personalized mathematical model of endotoxing-induced inflammatry responses in young men and assoiciated changes in heart rate variability. *Mathematical Modelling of Natural Phenomena*, 13(42), 2018.

[33] R.D. Fremont and T. W. Rice. How soon should we start interventional feeding in the icu? *Current Opinion in Gastroenterology*, 30(2):178–181, 2014.

[34] A. C. Fuchs, E. V. Granowitz, L. Shapiro, E. Vannier, G. Lonnemann, J. B. Angel, J. S. Kennedy, A. R. Rabson, E. Radwanski, M. B. Affrime, D. L. Cutler, P. C. Grint, and C. A. Dinarello. Clinical, hematologic, and immunologic effects of interleukin-10 in humans. *J. Clin. Immunol*, 16:291–303, 1996.

[35] M.P.W. Grocott, D.S. Martin, D.Z.H. Levett, R. McMorrow, J. Windsor, and H.E. Montgomery. Arterial blood gases and oxygen content in climbers on mount everest. *N Engl J Med*, 360:140–149, 2009.

[36] R. Grover, D. Zaccardelli, G. Colice, K. Guntupalli, D. Watson, and J.L Vincent. An open-label dose escalation study of the nitric oxide synthase inhibitor, ng-methyl-l-arginine hydrochloride (546c88), in patients with septic shock. *Critical Care Medicine*, 27(5):913–922, 1999.

[37] H. Haario, M. Laine, A. Mira, and E. Saksman. Dram: Efficient adaptive mcmc. *Statistics and Computing*, 16(4):339–354, 2006.

[38] P.H. Hackett and R.C. Roach. High-altitude illness. *N Engl J Med.*, 345:107–114, 2001.

[39] G. Hartmann, M. Tschop, R. Fischer, C. Bidlingmaier, R. Riepl, K. Tschöp, H. Hautmann, S. Endres, and M. Toepfer. High altitude increases circulating interleukin-6, interleukin-1 receptor antagonist and c-reactive protein. *Cytokine*, 12:246–252, 2000.

[40] A. C. Hindmarsh, P. N. Brown, K. E. Grant, S. L. Lee, R. Serban, D. E. Shumaker, and C. S. Woodward. SUNDIALS: Suite of nonlinear and differential/algebraic equation solvers. *ACM Transactions on Mathematical Software (TOMS)*, 31(3):363–396, 2005.

[41] R. D. Huhn, E. Radwanski, J. Gallo, M. B. Affrime, R. Sabo, G. Gonyo, A. Monge, and D. L. Cutler. Pharmacodynamics of subcutaneous recombinant human interleukin-10 in healthy volunteers. *Clin. Pharmacol. Ther*, 62(2):171–180, 1997.

[42] P. Isler, B. G. de Rochemonteix, F. Songeon, N. Boehringer, and L. P. Nicod. Interleukin-12 production by human alveolar macrophages is controlled by the autocrine production of interleukin-10. *Am. J. Respir. Cell Mol. Biol*, 20:270–278, 1999.

[43] N. Jafar, H. Edriss, and K. Nugent. The effect of short-term hyperglycemia on the innate immune system. *The American Journal of Medical Sciences*, 351(2):201–211, 2016.

[44] C. A. Janeway Jr, P. Travers, M. Walport, and M. J. Shlomchik. *Immunobiology: The Immune System in Health and Disease*. Garland Science, New York, 5th edition, 2001.

[45] C. Jean-Quartier, F. Jeanquartier, I. Jurisica, and A. Holzinger. In silico cancer research towards 3r. *BMC Cancer 18*, 408, 2018.

[46] K. A. Kirkeboen and O. A. Strand. The role of nitric oxide in sepsis - an overview. *Acta Anasthesiol Scand*, 43:275–288, 1999.

[47] R. Kumar, G. Clermont, Y. Vodovotz, and C. C. Chow. The dynamics of the acute inflammation. *Journal of Theoretical Biology*, 230:145–155, 2004.

[48] C. H. Lang and C. Dobrescu. Sepsis-induced increases in glucose uptake by macrophage-rich tissues persist during hypoglycemia. *Metabolism*, 40:585–593, 1991.

[49] L. Leonidou, A. Mouzaki, M. Michalaki, A. L. DeLastic, V. Kyriazopoulou, H. P. Bassaris, and C. A. Gogos. Cytokine production and hospital mortality in patients with sepsis-induced stress hyperglycemia. *Journal of Infection*, 55:340–346, 2007.

[50] A. López, J.A. Lorente, J. Steingrub, J. Bakker, A. McLuckie, S. Willatts, M. Brockway, A. Anzueto, L. Holzapfel, D. Breen, M. Silverman, J. Takala, J. Donaldson, G. Grove C. Arneson, S. Grossman, and R. Grover. Multiple-center, randomized, placebo-controlled, double-blind study of the nitric oxide synthase inhibitor 546c88: Effect on survival in patients with septic shock. *Critical Care Medicine*, 32(1):21–30, 2004.

[51] A.D. Malkin, R.P. Sheehan, S.Mathew, W.J. Federspiel, H. Redl, and G. Clermont. Neutrophil phenotype model for extracorporeal treatment of sepsis. *Plos Comp. Bio.*, 11(10), 2015.

[52] A. Mathonnet and A. Cariou. Glycemic control in sepsis. *Advances in Sepsis*, 6(1):16–18, 2007.

[53] C.A. McCloskey, T.R. Billiar, Edited by D. Salvemini, T.R. Billiar, and Y. Vodovotz. *Nitric oxide in shock: sepsis and hemorrhage. In: Nitric Oxide and Inflammation. Progress in Inflammation Research*. Birkhauser Verlag Basel, Switzerland, 2001.

[54] S. I. Miller, J. Wallace, D. M. Musher, E. J. Septimus, S. Kohl, and R. E. Baughn. Hypoglycemia as a manifestation of sepsis. *The Academic Journal of Medicine*, 68:649–654, 1980.

[55] S. S Moncada and J. D. Erusalimsky. Does nitric oxide modulate mitochondrial energy and apoptosis? *Nat Rev Mol Cell Biol*, 3(3):214–20, 2002.

[56] L. Razavi Nematollahi, A.E. Kitabchi, F. B. Stentz, B.A. Larijani, M.H. Gozashti, K. Omidfar, and E. Taheri. Proinflammatory cytokines in response to insulin-induced hypoglycemic stress in healthy subjects. *Metabolism - Clinical and Experimental*, 58(4):443 – 448, 2009.

[57] R. S. Parker, J. S. Hogg, A. Roy, J. A. Kellum, T. Rimmel, S. Daun-Gruhn, M. V. Fedorchak, I. E. Valenti, W. J. Federspiel, J. Rubin, Y. Vodovotz, C. Lagoa, and G. Clermont. Modeling and hemofiltration treatment of acute inflammation. *Processes*, 4(38), 2016.

[58] T. Pfeiffer, S. Schuster, and S. Bonhoeffer. Cooperation and competition in the evolution of atp-producing pathways. *Science*, 292:504–507, 2001.

[59] I. Ramirez-Zuniga, J.E.Rubin, D.Swigon, and G. Clermont. Mathematical modeling of energy consumption in the acute inflammatory response. *Journal Theoretical Biology*, 460:101–114, 2019.

[60] J. M. Ratter, H. M. Rooijackers, C. J. Tack, A. G. Hijmans, M. G. Netea, B. E. de Galan, and R. Stienstra. Proinflammatory effects of hypoglycemia in humans with or without diabetes. *Diabetes*, 66:1052–1061, 2017.

[61] A. Reynolds, J. Rubin, G. Clermont, J. Day, Y. Vodovotz, and G. B. Ermentrout. A reduced mathematical model of the acute anti-inflammatory response I. Derivation of model and analysis of anti-inflammation. *Journal Theoretical Biology*, 242:220–236, 2006.

[62] G. Schlag and H.Redl (Eds). *Shock, Sepsis, and Organ Failure*. Springer-Verlag Berlin Heidelberg, Berlin, 1999.

[63] G. Schlag, H. Redl, J. Davies, C.J.J. Vuuren, and P.Smuts. *Live Escherichia coli Sepsis Models in Baboons.* Spriger, Berlin Heidelberg, 1993.

[64] G.L. Semenza. Life with oxygen. *Science*, 318:62–64, 2007.

[65] C.W. Seymour, V.X. Liu, T.J. Iwashyna, F.M. Brunkhorst, T.D. Rea, A. Scherag, G. Rubenfeld, J.M. Kahn, M. Shankar-Hari, M. Singer, C.S. Deutschman, G.J.Escobar, and D.C. Angus. Assessment of clinical criteria for sepsis: For the third international consensus definitions for sepsis and septic shock (sepsis-3). *JAMA*, 315(8):762–74, 2016.

[66] M. Singer. The role of mitochondrial dysfunction in sepsis-induced multi-organ failure. *Virulence*, 5(1):66–72, 2014.

[67] S. Singh-Gryzbon, B. Ncho, and V. Sadri V et al. Influence of patient-specific characteristics on transcatheter heart valve neo-sinus flow: An in silico study. *Ann Biomed Eng*, 2020.

[68] R. C. Smith. *Uncertainty Quantification: Theory, Implementation, and Applications*. SIAM, Philadelphia, 2014.

[69] W. S. Spector (Ed.). *Handbook of Biological Data*. W.B. Saunders, London, 1st edition, 1956.

[70] R. Ssekitoleko, S. T. Jacob, P. Banura, R. Pinkerton, D. B. Meya, S. J. Reynolds, N. Kenya-Mugisha, H. Mayanja-Kizza, R. Muhindo, S. Bhagani, W. M. Scheld, and C. C. Moore. Hypoglycemia at admission is associated with inhospital mortality in ugandan patients with severe sepsis. *Crit Care Med*, 39(10):2271–2276, 2011.

[71] W. Stahl, M. Matejovic, and P. Radermacher. Inhibition of nitric oxide synthase during sepsis: Revival because of isoform selectivity? *Shock*, 34(3):321,322.

[72] R. F. Stengel, R. Ghigliazza, N. Kulkarni, and O. Laplace. Optimal control of innate immune response. *Optimal control applications and methods*, 23:91–104, 2002.

[73] B. Su, W. Zhou, K. S Dorman, and D.E. Jones. Mathematical modelling of immune response in tissues. *Computational and Mathematical Methods in Medicine*, 10(1):9–38, 2009.

[74] D. Swigon, S. R. Stanhope, S. Zenker, and J.E. Rubin. On the importance of the jacobian determinant in parameter inference for random parameter and random measurement error models. *SIAM/ASA J. Uncertainty Quantification*, 7(3):975–1006, 2019.

[75] J. Tan and X. Zou. Optimal control strategy for abnormal innate immune response. *Computational and Mathematical Methods in Medicine*, 2015:16, 2015.

[76] D. D. Thomas, X. Liu, S. P. Kantrow, and J. R. Lancaster Jr. The biological lifetime of nitric oxide: Implications for the perivascular dynamics of no and o2. *PNAS*, 98(1):355–360, 2001.

[77] K. Todar. *Growth of bacterial populations. In: Todar's Online Textbook of Bacteriology*. K. Todar, 2012.

[78] J. Tolles and W.J. Meurer. Logistic regression: Relating patient characteristics to outcomes. *JAMA*, 316(5):533–534, 2016.

[79] M. Torres, J. Wang P. J. Yannie, S. Ghosh, R. A. Segal, and A.M. Reynolds. Identifying important parameters in the inflammatory process with a mathematical model of immune cell influx and macrophage polarization. *Plos Computational Biology*, 15(7), 2019.

[80] K. Tsukaguchi, B. de Lange, and W. H. Boom. Differential regulation of IFN-gamma, TNF-alpha, and IL-10 production by CD4(+) alphabetaTCR+ T cells and vdelta2(+) gammadelta T cells in response to monocytes infected with mycobacterium tuberculosis-H37Ra. *Cell Immunol*, 19:12–20, 1999.

[81] G.I. Valderrama-Bahamóndez and H. Fröhlich. MCMC techniques for parameter estimation of ode based models in systems biology. *Front. Appl. Math. Stat.*, 5(55), 2019.

[82] J. A. Vrugt, J. M Hyman, B. A. Robinson, D. Higdon, C.J.F. Ter Braak, and C. G. H. Diks. Accelerating Markov Chain Monte Carlo simulation by differential evolution with self-adaptive randomized subspace sampling. *International Journal of Nonlinear Sciences and Numerical Simulation*, 10(3):273–290, 2008.